

COMPUTATIONAL STUDIES OF MOLYBDENUM  
OXIDE CLUSTERS  
AND ENVIRONMENTAL CORROSION OF IRON  
AND ZINC

By

AHMAD RAZZAGHI SOUFIANI

Bachelor of Science in Chemistry  
Birjand University  
Birjand, Iran  
1996

Master of Science in Physical Chemistry  
Isfahan University of Technology  
Isfahan, Iran  
1999

Submitted to the Faculty of the  
Graduate College of the  
Oklahoma State University  
in partial fulfillment of  
the requirements for  
the Degree of  
DOCTOR OF PHILOSOPHY  
July, 2014

COMPUTATIONAL STUDIES OF MOLYBDENUM  
OXIDE CLUSTERS  
AND ENVIRONMENTAL CORROSION OF IRON  
AND ZINC

Dissertation Approved:

Dr. Nicholas Materer

---

Dissertation Adviser

Dr. Allen Aplett

---

Dr. Barry Lavine

---

Dr. Charles Scott Weinert

---

Dr. John Mintmire

---

## ACKNOWLEDGEMENTS

I would never have been able to finish my dissertation without the guidance of committee members, help of my friends, and support from my family.

I would like to express my deepest gratitude to my advisor, professor Nicholas Materer for his excellent mentoring and support during my study. I have received encouragement and his great advices as my advisor and friend, not only in my research, but also in my life.

I would like to thank all my colleagues and friends. They helped me to start and finish my research. Finally, I would like to thank my family for their support and encouragement.

Name: RAZZAGHI SOUFIANI, AHMAD

Date of Degree: JULY, 2014

Title of Study: COMPUTATIONAL STUDIES OF MOLYBDENUM OXIDE  
CLUSTERS  
AND ENVIRONMENTAL CORROSION OF IRON AND ZINC

Major Field: CHEMISTRY

Abstract:

This dissertation describes two creative activities. The first is a computational study of molybdenum oxide clusters and the other is an experimental study of the corrosion of metals. The first effort covers three topics. First, the UV-Vis spectra for molybdenum oxide clusters were simulated utilizing Time-Dependent Density-Functional Theory (TD-DFT) calculations. The effects on the spectra due to changes in the cluster size and the variation of the formal charge of the molybdenum were investigated. Specifically, the location and transition intensity of a charge transfer transition between the molybdenum atoms were identified.

The second computational topic explored the adsorption and dissociation of dimethyl peroxide on the (100) surface of molybdenum trioxide and the hydrogen molybdenum bronze using Density-Functional Theory (DFT) calculations. It was found that dimethyl peroxide adsorbs molecularly on the oxide and bronze surfaces. However, the decomposition can occur only on the bronze surface through an O-O bond cleavage pathway. The final computational topic examined the equilibrium between a molybdenum monomer and a mixed valence dimer complex with gluconic acid. UV-Vis spectroscopy was used to measure the concentration of the dimer and monomer as a function of time and temperature. For this data, the activation energy for the dimer dissociation and the Gibbs free energy of the equilibrium could be calculated. To complement the experimental results, the UV-Vis spectra for complexes were simulated using TD-DFT calculations. The results are in agreement with the experimental assumption that the equilibrium is between a mixed valence dimer and two monomers.

The second effort is the experimental study of metal corrosion using a new method for corrosion evaluation based on thin wires. This effort covers two topics. The first topic was the corrosion of small iron wires in sodium chloride solutions, which may lead to a rapid technique to measure the efficiency of corrosion inhibitors. The second topic was the corrosion of mild steel and the galvanic corrosion of zinc wires in two types of soils. These results were used to develop a wireless corrosion sensor for underground structures.

## TABLE OF CONTENTS

Chapter	Page
I. INTRODUCTION.....	1
1.1 Molybdenum Oxide and Hydrogen Molybdenum Bronze .....	2
1.1.1 Molybdenum Oxide (100) Surface .....	4
1.1.2 Hydrogen Molybdenum Bronzes.....	4
1.2 Schrödinger Equation and Its Solution .....	6
1.2.1 Hartree-Fock (HF) Approximation.....	7
1.2.2 Density Functional Theory (DFT) .....	9
1.2.3 Time-Dependent Density Functional Theory (TD-DFT) .....	12
1.3 Solvation Models .....	14
1.4 Corrosion.....	17
1.4.1 Corrosion Types.....	18
1.4.2 Laboratory Studies of Corrosion.....	22
1.4.3 Corrosion Prevention Methods .....	23
1.4.4 Corrosion Detection.....	24
II. THEORETICAL PREDICTION OF UV-VIS SPECTRA FOR MOLYBDENUM OXIDE CLUSTERS .....	27
2.1 Computational Procedure.....	28
2.2 Results and Discussion .....	29
2.2.1 Chains .....	29
2.2.1.1 112 Chains .....	32
2.2.1.2 113 Chains .....	37
2.2.1.3 114 Chains .....	40
2.2.2 Ribbons .....	43
2.2.2.1 122 Ribbons .....	43
2.2.2.2 123 Ribbons .....	47
2.2.2.3 124 Ribbons .....	50
2.2.3 Layers.....	54
2.3 Summary.....	57

Chapter	Page
III. DENSITY FUNCTIONAL STUDIES OF DIMETHYL PEROXIDE ADSORPTION AND DISSOCIATION ON MoO <sub>3</sub> (100) AND H <sub>0.33</sub> MoO <sub>3</sub> (100) SURFACES .....	58
3.1 Computational Procedure.....	59
3.2 Results and Discussion .....	60
3.2.1 Adsorption of Dimethyl Peroxide on the MoO <sub>3</sub> (100) Surface .....	62
3.2.2 Dissociation of Dimethyl Peroxide on the MoO <sub>3</sub> (100) Surface .....	65
3.2.3 Adsorption of Dimethyl Peroxide on the Bronze H <sub>0.33</sub> MoO <sub>3</sub> (100) Surface .....	66
3.2.4 Dissociation of Dimethyl Peroxide on the Bronze Surface Through O-O Bond Cleavage.....	68
3.2.5 Dissociation of Dimethyl Peroxide on the Bronze Surface Through C-O Bond Cleavage .....	72
3.3 Summary.....	74
IV. EXPERIMENTAL AND THEORETICAL STUDIES OF MOLYBDENUM-GLUCONIC ACID COMPLEXES .....	76
4.1 Experimental Procedure.....	77
4.2 Computational Procedure.....	77
4.3 Results and Discussion .....	78
4.3.1 Experimental.....	80
4.3.2 Computational Analysis.....	86
4.4 Summary.....	94
V. ENVIRONMENTAL CORROSION RATES OF IRON AND ZINC WIRES.....	96
5.1 Corrosion of Iron and Zinc Wires in Sodium Chloride Solution.....	97
5.2 Corrosion Inhibitors.....	103
5.3 Summary.....	107
VI. CORROSION IN SOILS.....	108
6.1 Corrosion of Mild Steel Coupons in Soil.....	109
6.2 Galvanic Corrosion of Zinc Wires in Soil .....	113
6.3 Corrosion Sensor for Pipelines .....	116
6.4 Summary.....	119

Chapter	Page
VII. CONCLUSION .....	121
7.1 Computational.....	121
7.1.1 UV-Vis Spectra Simulation of Molybdenum Oxide Clusters.....	122
7.1.2 Adsorption and Dissociation of Dimethyl Peroxide on Molybdenum Oxide and Its Hydrogen Bronze (100) Surface.....	123
7.1.3 Molybdenum-Gluconic Acid Complexes .....	125
7.2 Experimental.....	126
7.2.1 Corrosion of Metal Wires in Solution.....	125
7.2.2 Corrosion in Soil.....	127
 REFERENCES .....	 129

## LIST OF TABLES

Table	Page
2-1 HOMO and LUMO energies and HOMO to LUMO excitation wavelengths for chains.....	30
2-2 HOMO and LUMO energies and HOMO to LUMO excitation wavelengths for 112 chains.....	32
3-1 Structural parameters and adsorption energies of isolated and molecularly adsorbed dimethyl peroxide (DMP) forms and transition states for their conversion on MoO <sub>3</sub> cluster.....	63
3-2 Structural parameters and adsorption energies of isolated and molecularly adsorbed dimethyl peroxide (DMP) forms and transition states for their conversion on H <sub>0.33</sub> MoO <sub>3</sub> bronze cluster .....	67
3-3 Structural parameters and adsorption energies of molecularly adsorbed dimethyl peroxide (DMP) forms on MoO <sub>3</sub> and H <sub>0.33</sub> MoO <sub>3</sub> .....	68
3-4 Structural parameters and adsorption energies of molecularly adsorbed dimethyl peroxide (DMP) and forms produced by O-O bond cleavage and transition states for molecularly adsorbed form conversion to these structures on bronze cluster .....	69
3-5 Structural parameters and energies of stable structures and transition states for the BOO2 to BOO1 conversion.....	71
3-6 Structural parameters and adsorption energies of molecularly adsorbed dimethyl peroxide (DMP) and forms produced by C-O bond cleavage and transition states for molecularly adsorbed form conversion to these structures on bronze cluster .....	73
4-1 Experimental data used to calculate activation energy (E <sub>a</sub> ) for the dissociation of the dimer (Reaction I).....	83
4-2 Data used to calculate Gibbs free energy (ΔG) for the dissociation of the dimer (Reaction II).....	85
4-3 Computed ΔG for equilibrium IV in gas phase and aqueous solution .....	93
5-1 Corrosion time of iron wires in sodium chloride 0.5% and 5% solutions.....	99
5-2 Corrosion time of zinc wires in sodium chloride 5% solution .....	102
5-3 Corrosion inhibition efficiency of calcium gluconate .....	105

Table	Page
5-4 Corrosion inhibition efficiency commercial inhibitors .....	107
6-1 Weight loss of mild steel coupons in Earthgro (EG) soils with various sodium chloride content.....	111
6-2 Weight loss of mild steel coupons in Miraclegro (MG) soils with various sodium chloride content.....	112
6-3 Corrosion rate of mild steel coupons in soils with various sodium chloride content .....	113
6-4 Data for galvanic corrosion of zinc wires connected to mild steel coupons in Miraclegro (MG) soil containing 5% sodium chloride by weight (MG-5) .....	115
6-5 Galvanic corrosion of zinc wires in Miraclegro (MG) soil containing 5% sodium chloride by weight (MG-5) .....	118

## LIST OF FIGURES

Figure	Page
1-1 Schematic view of $\text{MoO}_3 \cdot 2\text{H}_2\text{O}$ , $\beta\text{-MoO}_3 \cdot \text{H}_2\text{O}$ , and $\alpha\text{-MoO}_3$ crystalline structures .....	3
1-2 The (100) plan for a cubic cell and $\alpha\text{-MoO}_3$ .....	4
1-3 Available hydrogen insertion sites in $\text{MoO}_3$ , and $\text{H}_{0.33}\text{MoO}_3$ structure .....	5
1-4 SCF steps to solve the Schrödinger equation .....	9
1-5 SCF steps to solve the Kohn-Sham equations.....	12
1-6 A typical Linear Response Time-Dependent Density Functional Theory (LR-TDDFT) calculation scheme .....	13
1-7 Solvation models .....	14
1-8 Solvation steps.....	15
1-9 Solvent cavities.....	16
1-10 Uniform corrosion .....	18
1-11 Local corrosion.....	19
1-12 Intergranular corrosion .....	21
1-13 Schematic representation of zinc-iron galvanic cell.....	22
2-1 Molybdenum oxide cluster structures.....	28
2-2 UV-Vis spectra of molybdenum oxide chains of various sizes.....	30
2-3 HOMO and LUMO energy levels for chain structures of various sizes .....	31
2-4 HOMO and LUMO energy levels for 112(66) and 112(56) chains .....	33
2-5 UV-Vis spectra for 112 chains .....	35
2-6 Electron density transfers for 112(66) chain .....	36
2-7 Electron density transfer for excitation at 750 nm for 112(56) chain .....	36
2-8 UV-Vis spectra for 113 chains .....	38
2-9 Examples of ligand to metal (LMCT) and intervalence (IVCT) charge transfers for 113 chains.....	39
2-10 UV-Vis spectra for 114 chains .....	41
2-11 Examples of ligand to metal (LMCT) and intervalence (IVCT) charge transfers for 114 chains.....	42
2-12 UV-Vis spectra for ribbons of various sizes.....	44
2-13 UV-Vis spectra for 122 ribbons.....	45
2-14 Examples of ligand to metal (LMCT) and intervalence (IVCT) charge transfers for 122 ribbons .....	46

Figure	Page
2-15 UV-Vis spectra for 123 ribbons.....	48
2-16 Examples of ligand to metal (LMCT) and intervalence (IVCT) charge transfers for 123 ribbons.....	49
2-17 UV-Vis spectra for 124 ribbons.....	51
2-18 Examples of ligand to metal (LMCT) and intervalence (IVCT) charge transfers for 124 ribbons.....	53
2-18 UV-Vis spectra for 222 Layer.....	55
2-19 Examples of ligand to metal (LMCT) and intervalence (IVCT) charge transfers for 222 layer.....	56
3-1 Molybdenum oxide and hydrogen molybdenum bronze structures.....	59
3-2 Frontier orbitals: Dimethyl peroxide, MoO <sub>3</sub> , and H <sub>0.33</sub> MoO <sub>3</sub> .....	61
3-3 Molecularly adsorbed dimethyl peroxide (DMP) forms on MoO <sub>3</sub> (100) surface.....	63
3-4 Reaction coordinate between molecularly adsorbed dimethyl peroxide (DMP) forms on MoO <sub>3</sub> (100) surface.....	64
3-5 Stable structure from dimethyl peroxide C-O bond dissociation on MoO <sub>3</sub> (100) surface.....	64
3-6 Molecularly adsorbed dimethyl peroxide (DMP) forms on H <sub>0.33</sub> MoO <sub>3</sub> (100) surface.....	66
3-7 Reaction coordinate between molecularly adsorbed dimethyl peroxide (DMP) forms on H <sub>0.33</sub> MoO <sub>3</sub> .....	67
3-8 Reaction coordinate between molecularly adsorbed dimethyl peroxide (DMP) and structures produced by O-O bond cleavage on bronze cluster.....	70
3-9 Pathway for conversion of BOO2 to BOO1 on bronze surface.....	72
3-10 Reaction coordinate between molecularly adsorbed dimethyl peroxide (DMP) and structures produced by C-O bond cleavage on bronze cluster.....	73
4-1 D-gluconic acid structure.....	78
4-2 D-gluconic acid complexes with molybdenum.....	79
4-3 UV-Vis spectrum of blue dimer complex.....	81
4-4 UV-Vis spectrum of 2:1 blue complex as function of time after heated from room temperature to 40 °C.....	81
4-5 Kinetics measurements at 20, 40, 60, and 80 °C for diluted blue dimer.....	82
4-6 Arrhenius plot to calculate the activation energy (E <sub>a</sub> ) for the dissociation of the dimer (Reaction I).....	83
4-7 lnK vs 1/T plot to calculate the Gibbs free energy (ΔG) for proposed dissociation of the dimer (Reaction II).....	85
4-8 2-methoxyethanol and erythritol complexes with Mo(VI).....	87
4-9 Computed and experimental spectra of molybdic acid and molybdate.....	87
4-10 Experimental and simulated spectra for all possible dimer complexes.....	89
4-11 Experimental and simulated spectra for Mo(VI, V) dimer complex in various solvents.....	90

Figure	Page
4-12 Experimental and simulated spectra for Mo(V, V) dimer complex in water.....	91
4-13 Simulated spectra for Mo(V) and Mo(VI) monomer complexes in water .....	91
5-1 Wire holder and data collection board.....	97
5-2 Wire conductance change with time for iron wire (r = 0.065 mm) in sodium chloride 5% solution .....	98
5-3 Weight loss of iron wires in sodium chloride solutions .....	100
5-4 Zinc wires weight loss in sodium chloride 5% solution.....	102
5-5 Iron gluconate complex structure .....	104
5-6 Iron wire corrosion rate in sodium chloride 0.5% solution in presence of calcium gluconate as inhibitor.....	106
6-1 Apparatus for corrosion test in soil.....	110
6-2 Weight loss of mild steel coupons in Earthgro (EG) soils with various sodium chloride content.....	111
6-3 Weight loss of mild steel coupons in Miraclegro (MG) soils with various sodium chloride content.....	112
6-4 Zinc wire and mild steel coupon installed on holder for galvanic corrosion test.....	114
6-5 Weight loss of zinc wires due to galvanic corrosion in Miraclegro soil containing 5% sodium chloride by weight (MG-5).....	115
6-6 Galvanic corrosion of zinc wires and expected corrosion of mild steel coupons in Miraclegro soil containing 5% sodium chloride by weight (MG-5) .....	116
6-7 Passive wireless corrosion sensor and passive radio frequency identification (RFID) system .....	117
6-8 Sensor system for zinc galvanic corrosion in Miraclegro soil containing 5% sodium chloride by weight (MG-5).....	118

## CHAPTER I

### INTRODUCTION

This dissertation describes two creative activities. The first is a computational study of molybdenum oxide clusters and the other is an experimental study of the corrosion of metals. The first effort covers three topics. Chapter 2 covers the theoretical simulation of UV-Vis spectra for molybdenum oxide clusters. In this chapter, the effects on the spectra due to changes in the cluster size and the variation of the formal charge of the molybdenum are investigated. Adsorption and decomposition of dimethyl peroxide on the molybdenum oxide and hydrogen molybdenum bronze surfaces is studied computationally in Chapter 3. Finally, in Chapter 4, molybdenum complexes with D-gluconic acid are examined computationally and experimentally. The second effort is discussed in three experimental sections. The corrosion of small iron wires in sodium chloride solution and efficiency of corrosion inhibitors are studied in Chapter 5. In Chapter 6, the corrosion of mild steel and the galvanic corrosion of zinc wires in soils are investigated. Finally, application of corrosion studies to build a wireless corrosion sensor for underground structures is described in Chapter 6. In this chapter, the background for both projects is described in turn.

## 1.1 Molybdenum Oxide and Hydrogen Molybdenum Bronze

Transition metal oxides are used in many valuable industrial processes either directly or supported on other materials. For instance, molybdenum oxide and its bronzes with other metals and hydrogen are highly important in many industrial processes. Molybdenum oxides have catalytic activity toward oxidation of alcohols and ethers[1]. These compounds act as catalysts in selective oxidation of hydrocarbons[2] and production of acrylonitrile and acrylic acid[3, 4]. They are used as catalyst for catalytic hydrocarbon oxidation and dehydrosulfurization processes[5-7]. These complexes also have interesting optical and electronic properties, which makes them valuable for electrochromic devices[8-12]. These important properties depend on structure and oxidation number of molybdenum atoms in compound. They also have electrochemical applications in electrochemical sensors, and rechargeable batteries[7]. Finally, molybdenum oxides interact with carbohydrates and their derivatives which are important in various industrial and pharmaceutical processes[13, 14].

Three main crystal structures have been identified for molybdenum oxide:  $\text{MoO}_3 \cdot 2\text{H}_2\text{O}$ ,  $\beta\text{-MoO}_3 \cdot \text{H}_2\text{O}$ , and  $\alpha\text{-MoO}_3$ , these structures are shown in Figure 1-1[15]. Hydrate forms are 2-dimensional layers of distorted  $\text{MoO}_6$  octahedra joined by vertices, whereas the  $\alpha\text{-MoO}_3$  structure is a 2-dimensional layer of double chains of edge-sharing  $\text{MoO}_6$  octahedra connected through the vertices. In all structures, layers are stacked above each other with a void between the layers. This space is filled with interstitial water in dihydrate form and is vacant in the other structures.

Most of the experimental studies concerning molybdenum oxides are focused on  $\alpha\text{-MoO}_3$ , particularly, the catalytic activity of (100) face of solid oxide has been the subject of various researches. There is little theoretical work on the molybdenum oxide structure and its physicochemical properties. Zhai and coworkers studied the electronic structure and chemical bonding in  $\text{MoO}_n^-$  and  $\text{MoO}_n$  clusters[16], Papakondylis and Sautet studied the structure of the  $\alpha\text{-}$

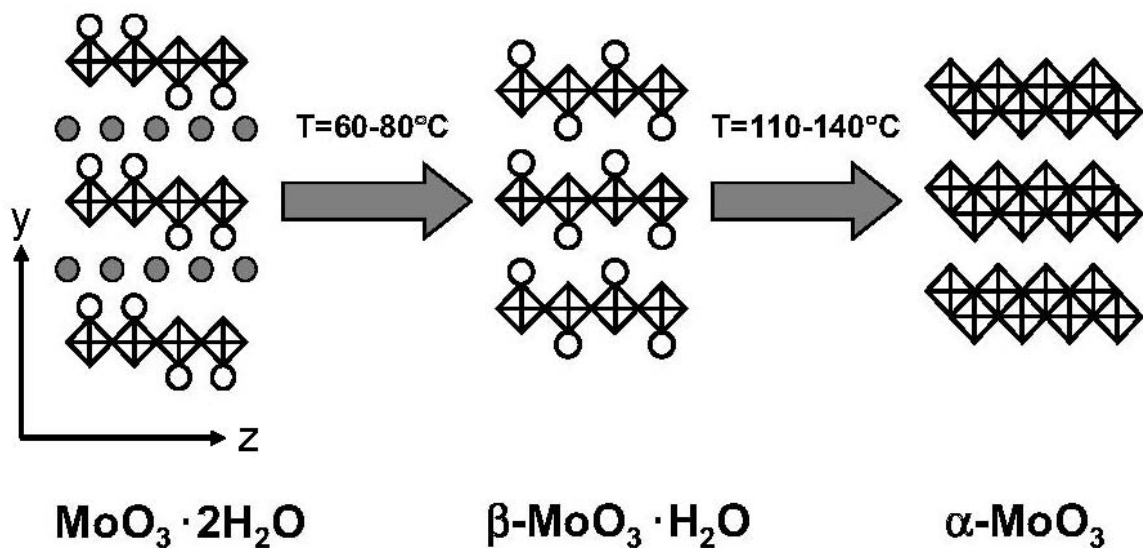


**Figure 1-1.** Schematic view of  $\text{MoO}_3 \cdot 2\text{H}_2\text{O}$ ,  $\beta\text{-MoO}_3 \cdot \text{H}_2\text{O}$ , and  $\alpha\text{-MoO}_3$  crystalline structures. (●) interstitial water molecules, (○) coordinated water molecules (Figure adapted from Ref [15])

$\text{MoO}_3$  and the adsorption of  $\text{H}_2\text{O}$  and  $\text{CO}$  on (100) surface of  $\alpha\text{-MoO}_3$  [17], Tsipis studied the structure of molybdenum oxide clusters[18], and recently, Kadassov and coworkers[19], studied the adsorption and dissociation of peroxides on (100) faces of molybdenum oxide and hydrogen molybdenum bronze clusters.

Although the natural cleavage plane is along the (010) surface, there is not an agreement between researchers on which face of the compound is catalytically active. For instance, Volta and Tatibouet[20] claimed that oxidation of propene takes place on the (100) face, while Bruckman and coworkers[21] believe that (010) face is more favorable for this oxidation. Guerrero-Ruiz and coworkers[22] concluded that Lewis acid centers on (100) face of the cluster are responsible for olefin adsorption and intermediate species stabilization, and Smith and Ozkan[23], claimed that  $\text{Mo}=\text{O}$  or  $\text{O}-\text{Mo}-\text{O}$  centers are responsible for the oxygen insertion step. The work here will focus on the reactivity of the (100) face of these materials.

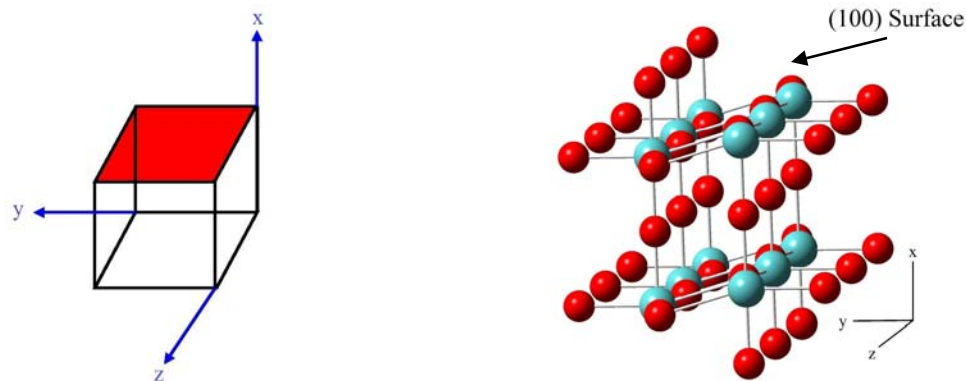


**Figure 1-2.** The (100) plane for (left) a cubic cell and (right)  $\alpha$ -MoO<sub>3</sub>

### 1.1.1 Molybdenum Oxide (100) Surface

To specify the surfaces of crystals, Miller Indices are used. In this system, a plane is represented as  $(hkl)$ , where  $h$ ,  $k$ , and  $l$  are Miller indices, which determine where this plane intercepts the three axes. To determine the Miller indices for a plane, first the intercepts of the plane with the axes are determined and expressed in terms of unit cell lengths, then Miller indices for that specific plane are the result of taking the reciprocal of these numbers. Hence, for the (100) plane, the plane intercepts the x axis on one unit cell length in the x direction and it is parallel to the y and z axes. The (100) plane for a cubic cell and molybdenum oxide are shown in Figure 1-2. The (100) surface of the molybdenum oxide is terminated with axial oxygen and bare molybdenum atoms within a double-chain layer that are possible positions for the adsorption of chemicals.

### 1.1.2 Hydrogen Molybdenum Bronzes

The term bronze, which originally used for Na<sub>x</sub>WO<sub>3</sub> compounds, is applied to various crystalline phases of transition metal oxides[24]. Bronzes are usually ternary compounds of general formula of A<sub>x</sub>M<sub>z</sub>O<sub>y</sub> where M is the transition metal and A can be H, NH<sub>4</sub><sup>+</sup>, alkali, alkaline

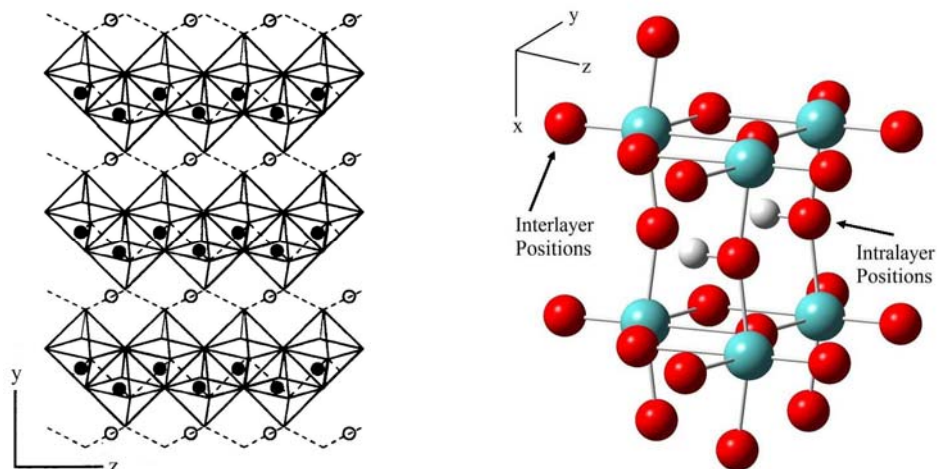


**Figure 1-3.** (left) Available hydrogen insertion sites in MoO<sub>3</sub>. (●) intralayer and (○) interlayer positions. (Figure adapted from Ref [26]). (right) H<sub>0.33</sub>MoO<sub>3</sub> structure

earth, rare earth, group 11, group 12, or other metal ions. Some of the unique features of these materials are their metallic luster, intense color, and metallic properties.

Four phases of hydrogen molybdenum bronzes with general H<sub>x</sub>MoO<sub>3</sub> ( $0 \leq x \leq 2$ ) formula have been reported[25]. The amount of hydrogen in each of these phases is different (phase I,  $0.23 < x < 0.4$ ; phase II,  $0.85 < x < 1.04$ ; phase III,  $1.55 < x < 1.72$ ; and phase IV,  $x = 2$ ). As shown in Figure 1-3, two sites are available for hydrogen insertion, intralayer and interlayer. Depending on the amount of hydrogen, they first attach to bridging oxygen atoms, (intralayer), and then start to attach to terminal oxygen atoms, (interlayer). Hence for H<sub>0.33</sub>MoO<sub>3</sub> bronze, all protons are attached to intralayer sites[26]. Figure 1-3 shows the available hydrogen insertion sites and the H<sub>0.33</sub>MoO<sub>3</sub> bronze structure.

The average oxidation number of molybdenum atoms in hydrogen molybdenum bronzes is less than six and this makes the bronzes strong reducing agents. These compounds have been the subject of research as potential catalysts for isomerization[27], hydrogenation[28], oxidation[29, 30], and dehydration[31] reactions. Apblett and coworkers[32] studied the reaction of hydrogen molybdenum bronze with triacetone triperoxide, and Kadassov and coworkers[19],

theoretically studied the adsorption and dissociation of hydrogen peroxide on the (100) face of  $\text{MoO}_3$  and  $\text{H}_{0.33}\text{MoO}_3$  by means of density functional calculations[19].

Gyurcsik and Laszalo reviewed complexation of carbohydrate ligands with molybdenum and other metals[33]. In particular, the complexation of D-gluconic acid has been subject of several studies[34-40]. Polarimetric, polarographic, spectrometric, and  $^{13}\text{C}$  NMR spectroscopic methods have been used to study gluconic acid complexation with molybdate and tungstate[41-44]. Ramos and coworkers have systematically studied complexation of various aldonic acids with molybdenum(VI) and tungsten(VI) by means of NMR spectroscopy[45]. They found that depending on pH and concentration conditions, gluconic acid forms 10 and 8 complexes with tungsten(VI) and molybdenum(VI), respectively.

As mentioned earlier, there is little theoretical work on molybdenum oxide and its bronzes. Thus, considering the interesting and valuable properties of these compounds, it is of great importance to study the structure, bonding, and physicochemical properties of these materials. In the next few chapters of this dissertation, the structure of the crystal will be modeled theoretically and the dependence of the UV-Vis spectra to the size of the clusters and valence of molybdenum atoms will be discussed (Chapter 2). After this, the adsorption and dissociation of dimethyl peroxide on the surface of the solid will be explained (Chapter 3). Finally, we will examine the reaction of the molybdenum oxide with gluconic acid (Chapter 4).

## **1.2 Schrödinger Equation and Its Solution**

In most quantum chemistry problems, the goal is to theoretically predict energy, optimized geometry, and properties of the molecular system under study by means of solving the time-independent Schrödinger equation:

$$\hat{H}\Psi_i = E_i\Psi_i \quad (1-1)$$

$$\hat{H} = -\frac{1}{2} \sum_{i=1}^N \nabla_i^2 - \frac{1}{2} \sum_{A=1}^M \nabla_A^2 - \sum_{i=1}^N \sum_{A=1}^M \frac{Z_A}{r_{iA}} + \sum_{i=1}^N \sum_{j>i}^N \frac{1}{r_{ij}} + \sum_{A=1}^M \sum_{B>A}^M \frac{Z_A Z_B}{R_{AB}} \quad (1-2)$$

(1)
(2)
(3)
(4)
(5)

$$\nabla_i^2 = \frac{\partial^2}{\partial X_i^2} + \frac{\partial^2}{\partial Y_i^2} + \frac{\partial^2}{\partial Z_i^2} \quad (1-3)$$

, where,  $\hat{H}$  is Hamiltonian operator for a system consisting of M nuclei and N electron,  $\Psi_i$  is the wavefunction for the ith state of the system which contains all the information about the quantum system at hand,  $E_i$  is the numerical value of the energy of the system, and  $\nabla_i^2$  is the Laplacian operator. The Hamiltonian consists of five terms: (1) electron's kinetic energy, (2) nuclei's kinetic energy, (3) electron-nuclei interaction energy, (4), electron-electron interaction energy and (5) nuclei-nuclei interaction energy.

### 1.2.1 Hartree-Fock (HF) Approximation

The traditional approach to solve this equation is the wavefunction approach in which a wavefunction is defined and the Schrödinger equation is solved. Because of the complexity, the Schrödinger equation is solved using approximations. Using the Born-Oppenheimer approximation, which assumes that the nuclei is much heavier than an electron, the wavefunction can be broken into electronic and nuclear parts. Hence, by applying this approximation, the Electronic Hamiltonian is the sum of terms (1), (3), and (4) in equation (1-2). Although, the problem is simplified, the complexity of electron-electron interactions prevents the Schrödinger equation to be solved analytically. One numerical approach is called the Hartree-Fock approximation.

The Hartree-Fock approach uses three main approximations[46]. Electrons are assumed to move in an average potential due to the fixed nuclei and the other electrons. This procedure results in the independent electron approximation. Each electron is in a molecular orbital constructed using a Linear Combination of Atomic Orbitals (LCAO):

$$\psi_i(r_i) = \sum_{\mu} C_{\mu i} \chi_{\mu}(r_i) \quad (1-4)$$

, where  $\psi_i$  is the  $i$ th molecular orbital,  $\chi_{\mu}$  is the atomic orbital (basis function), and  $C_{\mu i}$  is the atomic orbital coefficient. Finally, the total electronic wavefunction is constructed using a Slater determinant to ensure the wavefunction is anti-symmetric.

$$\Psi = \frac{1}{\sqrt{N!}} \begin{vmatrix} \psi_1(r_1) & \psi_2(r_1) & \dots & \psi_N(r_1) \\ \psi_1(r_2) & \psi_2(r_2) & \dots & \psi_N(r_2) \\ \vdots & \vdots & \vdots & \vdots \\ \psi_1(r_N) & \psi_2(r_N) & \dots & \psi_N(r_N) \end{vmatrix} \quad (1-5)$$

, where  $N$  is the number of electrons.

After constructing the total wavefunction using atomic orbitals, the electronic Schrödinger equation can be solved. However, to construct the average potential, the  $C_{\mu i}$  must be known. Hence the problem needs to be solved iteratively. This iterative approach is called the Self-Consistent-Field (SCF) method. The construction of the wavefunction is started using a series of guesses  $C_{\mu i}$ . Next, the Schrödinger equation is solved and the new  $C_{\mu i}$  are compared to the initial ones. When the new and initial sets are same, the SCF is said to have converged. These steps are demonstrated in Figure 1-4.

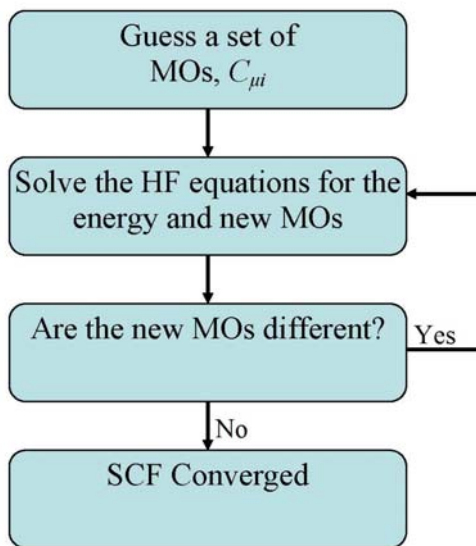


**Figure 1-4.** SCF steps to solve the Schrödinger equation.

The assumption that electrons move in an average potential due to the fixed nuclei and the other electrons basically ignores electron correlations resulting in serious errors in the final energy. To improve the results, usually post Hartree-Fock methods (Post-HF) are utilized (Configuration Interaction, Moller-Plesset Perturbation, Coupled-Cluster, and Multi-Configuration SCF methods) where electron-electron correlations are considered in solving the Schrödinger equation. Although Post-HF methods improve the calculation result, they are time consuming and very expensive computationally.

### 1.2.2 Density Functional Theory (DFT)

The other approach to solve the problem which accounts for electron-electron correlations is utilizing Density Functional Theory (DFT) methods, based on the Hohenberg and Kohn theorem[47]. This theorem proves that the ground state electronic energy can be determined by the electron density  $\rho$ , instead of wavefunction,  $\Psi$ . This theory was brought to practical use by Kohn and Sham through developing self-consistent equations[48]. The simplicity of the density

functional theory (DFT) methods lays in the fact that the electron density depends only on three spatial coordinates, independent of the number of electrons.

In density functional theory, electrons are considered to be non-interacting particles moving in an effective potential and the Kohn-Sham equations are solved:

$$\left[ -\frac{\hbar^2}{2m} \nabla^2 + V_{eff}(r) \right] \psi_i(r) = E_i \psi_i(r) \quad (1-6)$$

$$V_{eff}(r) = V_{ext}(r) + V_{coul}(r) + V_{XC}(r) \quad (1-7)$$

, where  $\psi_i(r)$  is a single Slater determinant for the non-interacting system,  $V_{ext}(r)$  is the external potential consisting of electron-nuclei interactions,  $V_{coul}(r)$  is the electron-electron repulsions, and  $V_{XC}(r)$  is the exchange-correlation interactions. The Hartree-Fock method includes the electron exchange part by constructing the wavefunction as a Slater determinant and approximating the electron-electron interactions as an average field. Post-Hartree-Fock methods construct the wavefunction by combination of multiple Slater determinants to account for electron correlation. In contrast, density functional theory methods use density-functionals for the exchange-correlation part of the effective potential.

The main goal of density functional theory methods is to design functionals connecting the electron density with the energy[49]. In density functional theory methods, the electronic energy is defined as[50]:

$$E = E^T + E^V + E^J + E^{XC} \quad (1-8)$$

, where  $E^T$  and  $E^V$  are kinetic and electron-nuclear interaction energies,  $E^J$  is the Coulomb electron-electron interaction energy, and  $E^{XC}$  is the exchange-correlation part of the electron-electron interaction energy.

At the beginning, all the density functional theory methods tried to define all the energy components as a functional of electron density, but these methods had poor performances. Later, Kohn and Sham[48], improved the performance of density functional theory methods by suggesting that  $E^T$  should be calculated using a set of orbitals representing the electron density, and taking  $E^{XC}$  as the only unknown. In fact, the difference between various modern density functional theory methods is the form of the functional for the  $E^{XC}$ .

In the simplest model known as Local Density Approximation (LDA), electron density is treated as a uniform electron gas which slowly varies by distance[51]. The improvement of this approximation is by considering the gradient of electron density via first and higher order derivatives of electron density. These methods are known as General Gradient Approximation (GGA) methods. The examples of such functionals are B or B88[52], PW86[53], PW91[54], and PBE[55] containing first order correction terms and BR[56], B95[57], and HCTH[58] functionals containing higher order gradients. In addition, Hybrid methods have been developed where exchange-correlation functional is constructed as a linear combination of the Hartree-Fock exact exchange and other exchange and correlation density functionals. The most popular hybrid functional is B3LYP (Becke, three-parameter, Lee-Yang-Parr) which consists of Becke exchange functional[52] and the correlation functional of Lee, Yang, and Parr[59]. Solving the Kohn-Sham equations implies computing the  $\rho(r)$ , which requires that the wavefunction be known, similar to Hartree-Fock approximation above. Thus, Kohn-Sham equations must be solved iteratively, as outlined in Figure 1-5.

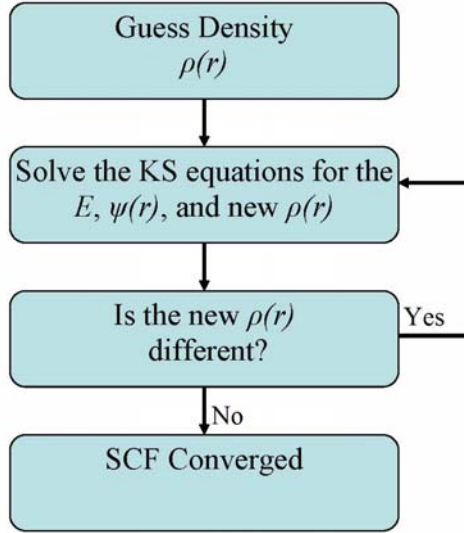


**Figure 1-5.** SCF steps to solve the Kohn-Sham equations.

### 1.2.3 Time-Dependent Density Functional Theory (TD-DFT)

Hohenberg and Kohn theorem[47] only applies to the ground state and hence, the time-dependent properties such as frequency-dependent response properties and photoabsorption spectra cannot be studied using the Kohn Sham equations. Within the density functional theory formalism, these properties need to be investigated using the time-dependent Kohn-Sham equations[60]:

$$i \frac{\partial \Psi(r, t)}{\partial t} = V_{\text{eff}}(r, t) \Psi(r, t) \quad (1-9)$$

$$V_{\text{eff}}(r, t) = V_{\text{ee}}(r, t) + V_{\text{ext}}(r, t) + V_{\text{XC}}(r, t) \quad (1-10)$$

, where the effective potential is composed of electron-electron interactions, external field, and exchange-correlation, respectively. The exchange-correlation potential is a functional of electron density and the ground state wavefunction.

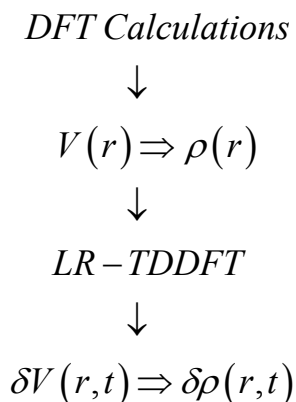


**Figure 1-6.** A typical Linear Response Time-Dependent Density Functional Theory (LR-TDDFT) calculation scheme.

If the external perturbation is small it does not completely destroy the ground state of the system. In this case the variation of the system by time will depend on the ground state wavefunction, which is linearly changed in presence of the external perturbation. This concept introduces the Linear Response Time-Dependent Density Functional Theory (LR-TDDFT), where the electron density of the ground state changes linearly with external perturbation[61]. Basically, calculations are started using time-independent Kohn-Sham equations to determine the ground state potential and hence the electron density, and then linear response time-dependent density functional theory calculations are utilized to calculate the changes in electron density and other time-dependent properties (Figure 1-6).

This formalism also allows the excited states to be determined, allowing properties such as the electronic absorption spectra to be calculated. This methodology is used in Chapter 2 to simulate the UV-Vis spectra of molybdenum oxide clusters for investigating the effects of cluster size and molybdenum formal charge on the spectra, and in Chapter 4 to simulate the UV-Vis spectra of molybdenum complexes with gluconic acid.

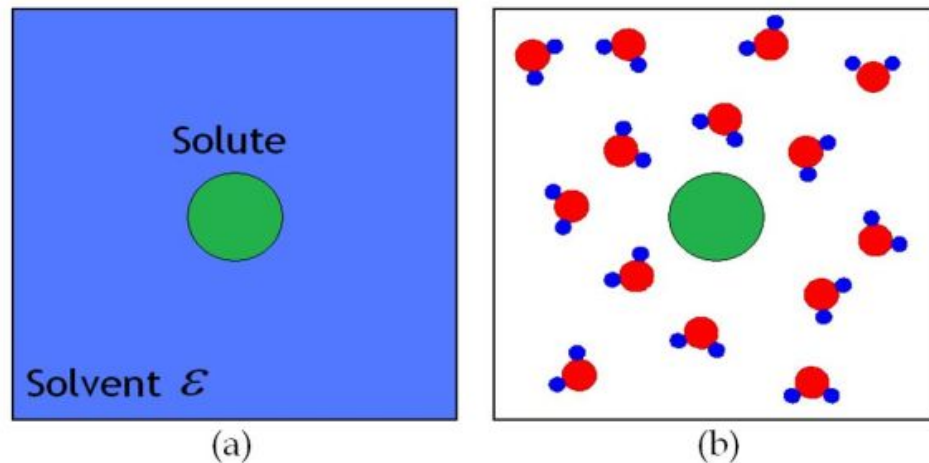


**Figure 1-7.** Solvation models.  
(a) implicit, (b) explicit

### 1.3 Solvation Models

Generally, quantum chemistry calculations are performed for systems in the gas phase, but most chemical reactions occur in solution. In the solution phase, electrostatic forces between solute and solvent affect the properties of substances such as their geometry, energy, and spectra. Hence to investigate the reactions in the solution phase, these electrostatic forces must be considered. To evaluate the solvent effects in computational chemistry, solvation models are used. Broadly, these models are divided in two types: explicit and implicit models. In explicit models, each solvent molecule is treated individually. For the implicit models, the solvent is represented by a continuum described by macroscopic properties such as the dielectric constant,  $\epsilon$ . These models are represented in Figure 1-7. From the definition above, it is clear that explicit model involves more details and produces more accurate results, but it is computationally expensive, hence in this research implicit models have been used.

Continuum models consider solvent as a uniform polarizable medium with a dielectric constant and place the solvent in a suitable hole in the medium[62, 63]. Usually the solvation of a solute is considered to happen through multiple steps (Figure 1-8). First a cavity is formed in the

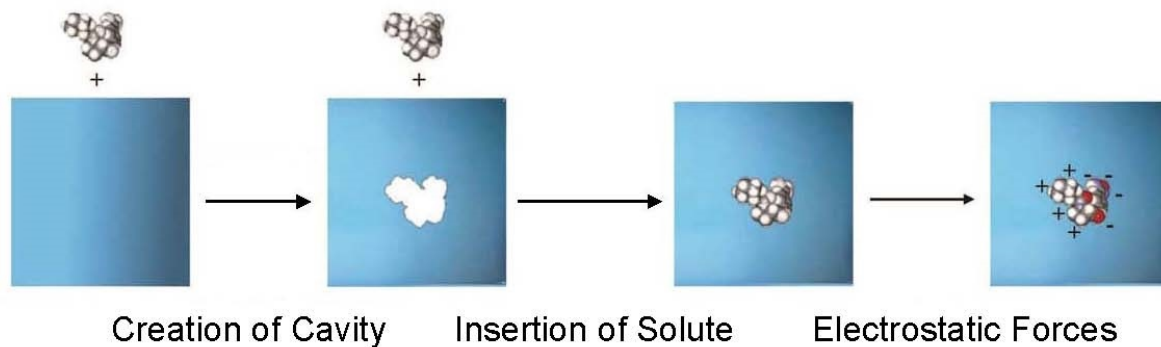


**Figure 1-8.** Solvation steps.

solvent and the solute molecule is placed in the cavity followed by reorientation and polarization of the solvent molecules in response to solute charge density. Finally, solvent polarization induces an electric field (reaction field) within the cavity that interacts with the solute dipole. The solvation energy, then, can be expressed as:

$$U_{solv} = U_{cav} + U_{disp-rep} + U_{elec} \quad (1-11)$$

, where  $U_{cav}$ ,  $U_{dis-rep}$ , and  $U_{elec}$  are cavitations energy, dispersion-repulsion interactions energy, and electrostatic interactions energy, respectively. The creation of the cavity requires energy and causes destabilization, the reorientation of the solvent molecules are due to dispersion-repulsion (mainly Van der Waals) interactions between solute and solvent molecules that lowers the energy of the system and finally, the back and forth polarization induced between solute and solvent molecules results in the most stable charge distribution in the system.

The electrostatic part of this equation, which involves the interaction of the reaction field with the solute charge density can be determined by the Poisson equation:

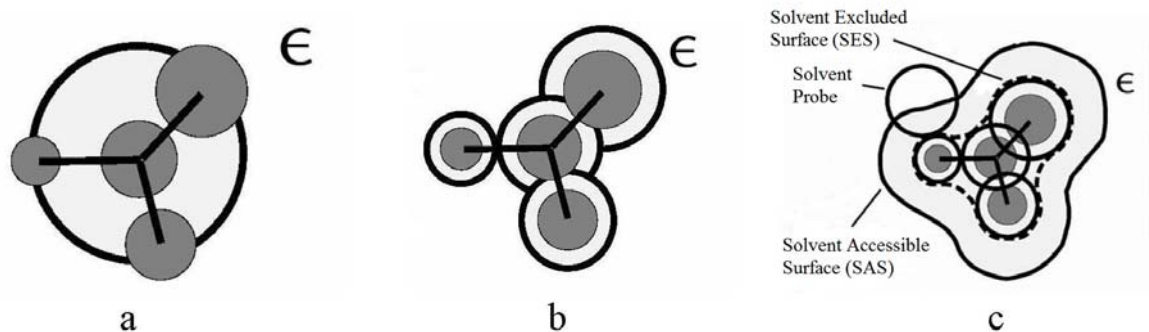


**Figure 1-9.** Solvent cavities.  
 (a) spherical, (b) interlocking spheres, (c) solvent accessible (SAS) and solvent excluded (SES) surfaces

$$\nabla \cdot [\varepsilon(r) \nabla \varphi(r)] = -4\pi\rho(r) \quad (1-12)$$

, where,  $\varepsilon(r)$ ,  $\varphi(r)$ , and  $\rho(r)$  are the solvent dielectric constant, the reaction field, and the solute charge density, respectively.

These models differ in: size and shape of the cavity, method of calculating the cavity creation and dispersion-repulsion contributions, how the charge distribution of solute is represented, whether the solute is described classically or quantum mechanically, and how the dielectric medium is described. In the simplest model known as the Onsager model[64], solute is placed in a spherical cavity with a radius that is determined from its gas phase structure (Figure 1-9). The charge distribution of the solute is expressed in terms of a dipole moment,  $\mu$ , and electrostatic interactions are calculated analytically. More sophisticated continuum models in which the solute molecule is treated quantum mechanically are known as Self-Consistent Reaction Field, (SCRF), models. In these models, the calculated electric moments induce charges in the dielectric medium, that in turn acts back on the solute molecule, causing the wavefunction to respond resulting in changes in the electric moments. This interaction is solved by iteration and

hence these models are called self-consistent. The most common self-consistent reaction field models are the Polarizable Continuum Model (PCM)[65], the Conductor-Like Screening Model (COSMO)[66, 67], the Conductor Polarizable Continuum (CPCM)[68] model that is basically the COSMO model with defined surface charges, and the Universal Solvation Models (SMD)[69].

The Tomasi polarizable continuum model, makes the cavity by interlocking spheres of van der Waals radii centered on each atom (Figure 1-9), and parameterizes the cavity-medium interaction based on the cavity surface area and solves the electrostatic interactions numerically. The conductor-like screening model employs a solvent accessible surface (SAS) to make the cavity (Figure 1-9). In this model, the solvent is considered to be a conductor except close to cavity and electrostatic interactions are solved numerically based on a conducting polygonal surface. Also, as recommended by Marenich and coworkers for  $\Delta G$  calculations, the universal solvation model calculates the partial atomic charges from the wavefunction and parameterized cavity-medium interactions based on the solvent excluded surface (SES) (Figure 1-9). Solvent models are used in Chapter 4 to simulate the UV-Vis spectra of molybdenum complexes with gluconic acid in solvents with the aim of investigating the solvent effect on the spectra.

#### **1.4 Corrosion**

Most metals are unstable and have tendency to react with their environment to form a more stable state with lower energy. It is due to this tendency of metals that the corrosion problems arises. The American Society for Testing and Materials (ASTM), defines corrosion as "the chemical or electrochemical reaction between a material, usually a metal, and its environment that produces a deterioration of the material and its properties"[67]. In the corrosion process, metal atoms are oxidized to metal ions and the released electrons are used to reduce  $O_2$  or  $H^+$  depending on the environment. The reactions involved in corrosion process can be summarized as:

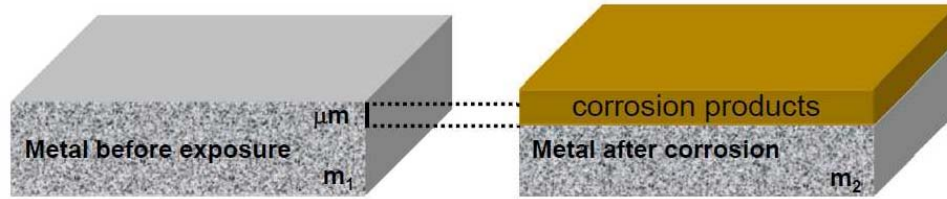
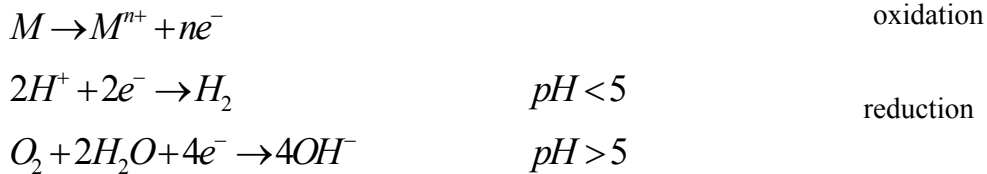


**Figure 1-10.** Uniform corrosion.



Millions of dollars are lost each year because of corrosion induced damage, a large percentage from the corrosion of iron and steel parts of equipment and underground metal structures in various industries. In addition to the corrosion cost directly from metallic structures, such as damage that forces replacement of structures and buildings, other costs of corrosion are related to corrosion control and the cost of designing new materials[69]. Therefore, the study of corrosion and corrosion inhibition and detection has attracted many scientists.

### 1.4.1 Corrosion Types

In the real world, metals are exposed to various environments such as atmosphere, water, soil, and industrial fluids. Depending on the environment to which a metal is exposed and the corrosive conditions, corrosion can take place through different mechanisms. The most important types of corrosion are explained briefly in this section. In the case of Uniform Corrosion, corrosion occurs all over the surface of the metal relatively evenly causing uniform decrease of the metal thickness[70] (Figure 1-10). The rate of the uniform corrosion may be controlled through two mechanisms: concentration control and activation control. Concentration control

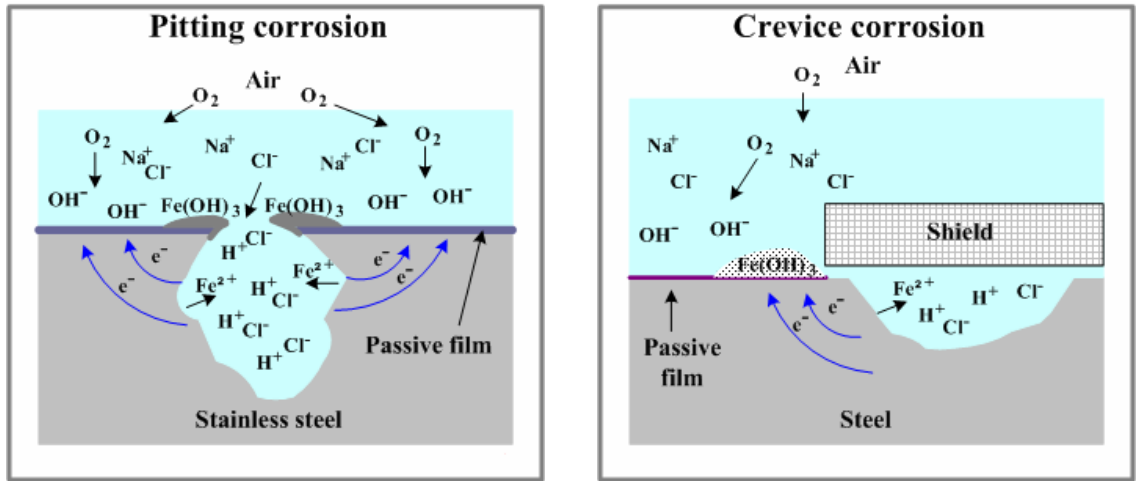


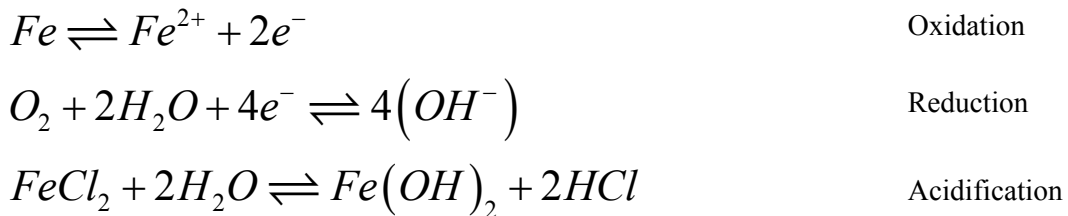
**Figure 1-11.** Local corrosion.  
(left) Pitting, (right) Crevice. (Figure adapted from Ref [73])

happens when the diffusion rate of the reactant or products to or from surface, where corrosion takes place, is the slowest step in the corrosion process. Activation control refers to rate of the oxidation and / or reduction reactions as the rate controlling step[71]. Uniform corrosion produces a protective metal oxide layer that prevents the metal from further corrosion. If this protective layer is damaged mechanically or by aggressive ions in the environment (e.g.  $\text{Cl}^-$ ), Localized Corrosion is initiated (Figure 1-11).

In contrast to uniform corrosion, when discrete areas of metal surface are corroded with the majority of the surface unchanged, corrosion is defined as Pitting Corrosion[72]. Essentially, when the passive layer on the surface of the metal is damaged due to physical or chemical forces, narrow pits are formed on the surface of the metal and the metal can be attacked by aggressive species of environment such as  $\text{Cl}^-$  and  $\text{SO}_4^{2-}$  [74]. Crevice Corrosion occurs when discrete areas on an alloy are physically isolated. This situation often happens underneath the surface in confined spaces such as under deposits, gaps, contact areas between parts, and inside cracks[72]. In this type of corrosion, these occluded spaces are wide enough for corrodent to enter and narrow enough such that corrodent remains. Once trapped, the dissolved oxygen is rapidly

depleted and a local galvanic cell is established due to the difference in the oxygen concentration of the solutions within a crevice and surrounding surface, which in turn promotes the corrosion[75].

The mechanisms of pitting and crevice corrosions are basically same. The passivating film is damaged and unprotected iron inside the pit or crevice is oxidized. Next, the generated electrons are consumed for reduction of dissolved oxygen outside the pit or crevice. As a result of these reactions, the electrolyte inside the pit or crevice gains positive electrical charge which attracts the negatively charged aggressive ions like  $Cl^-$ . The reaction of  $Cl^-$  and  $Fe^{2+}$  inside the pit or crevice decreases the pH which accelerate the corrosion.



Intergranular Corrosion occurs in alloys because of the composition difference between grain boundaries and inner parts of grains. For the case of steel, in presence of small amounts of carbon in steel, chromium reacts with carbon during heat treatment to produce carbide. The needed chromium diffuses from bulk to boundaries and chromium depletion occurs (Figure 1-12). The chromium-depleted areas are more instable and hence more susceptible for localized corrosion. As a result grains falling out resulting in a drastic loss of material strength.

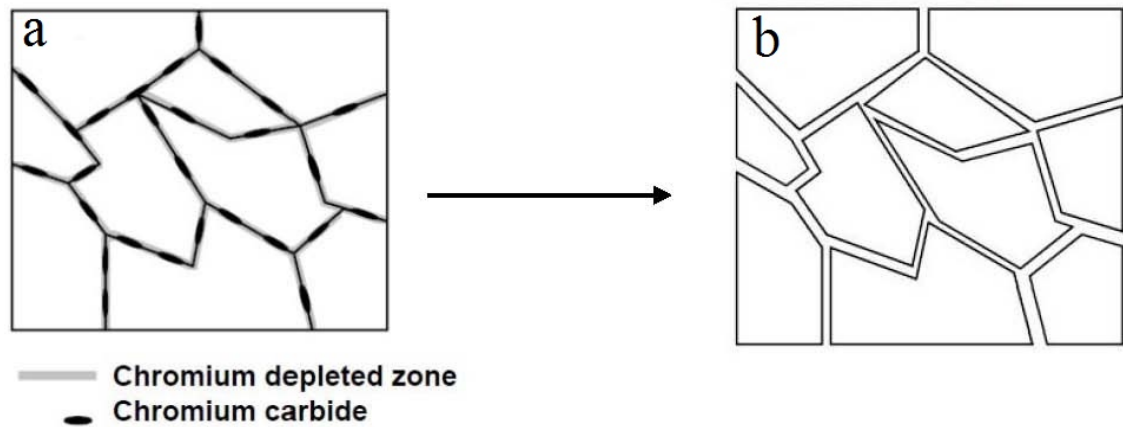
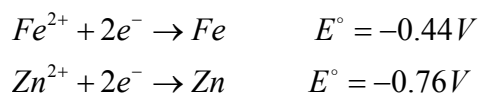


**Figure 1-12.** Intergranular corrosion.  
 (a) Chromium Carbide formation at grain boundaries  
 (b) Intergranular corrosion induced grain falling out.  
 (Figure adopted from Ref [76])

Galvanic Corrosion transpires when two different metals are in an electrical contact in an conducting electrolyte which in one metal corrodes preferentially to the other one[72]. Galvanic corrosion is an electrochemical process in which, depending on electrochemical potentials, one metal acts as anode where oxidation reaction happens and the other one acts as cathode where reduction reaction happens. During the oxidation reaction, the metal is transformed to ion by releasing of electrons, the released electrons are transferred to cathodic site via electrical contact and consumed by cathodic reaction. The electrochemical potentials for iron and zinc are:



Thus, the zinc will be the anode and corroded in the zinc-iron galvanic cell. Figure 1-13 illustrates the zinc-iron galvanic cell schematically.

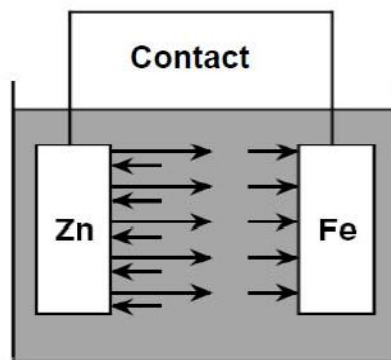


**Figure 1-13.** Schematic representation of zinc-iron galvanic cell

#### **1.4.2 Laboratory Studies of Corrosion**

To study the corrosion and effectiveness of corrosion inhibitors in the laboratory, several standard methods are available[77]: electrochemical, cabinet, immersion, and high-temperature / high-pressure (HT/HP), methods. In the work presented here, immersion corrosion tests[78] were utilized to accelerate the corrosion process. In this method, small pieces or coupons of the material are exposed to the test medium and the weight loss of the material is measured for a given period of time. In this type of corrosion test, chemical and physical parameters affecting the corrosion can be controlled. Concentration, pH, phase equilibrium, dissolved gases, and conductivity are among the chemical parameters and temperature, pressure, flow velocity, surface area, and time are among the physical parameters which can be controlled during the test.

The immersion method is used in Chapter 5 to study the corrosion of iron and zinc wires in sodium chloride solution. We used a new method to evaluate the corrosion rate of small wires instead of weight loss. This method is based on the change in the resistance of wire by time and is amenable to high-throughput screening. In this method small wires of known radii are installed on a holder, all the connections are sealed and only a known length of the wires are exposed to corrosive media. Wires are connected to an electronic board, which measures and saves the wire

resistance periodically. By plotting the resistance versus time, wire failure time is detected which is the time when the wire is corroded completely. The corrosion rate is calculated from the slope of the plot of masses of wires of various radii versus failure time. Also, the immersion method based on weight loss is used in Chapter 6 to study the corrosion of mild steel in soil.

### **1.4.3 Corrosion Prevention Methods**

Generally, the corrosion of metals happens through oxidation reaction of metal in an electrochemical cell where metal acts as anode. In addition to anode, there are three other major components, which are necessary to corrosion to occur: a corrosive media, a cathode where the reduction reaction happens, and an electron-conducting path between anode and cathode. The basic concept of most methods of corrosion protection is to either remove one or more of these cell components so that the metal will not corrode or changing the nature of the anode so that it becomes the cathode (cathodic protection)[79].

Galvanic corrosion happens when two dissimilar metals immersed in the same electrolyte are in electric contact. The metal with lower electrochemical potential acts as anode and the metal with higher electrochemical potential acts as cathode, leading to the corrosion of anode through oxidation reaction. The principle of galvanic corrosion is used in cathodic protection. In this method of protection, a metal with lower electrochemical potential than that of metal to be protected, is attached to the structure and acts as a sacrificial anode and hence protects the structure from corroding.

The other method of corrosion protection is making a barrier between the metal of interest and the corrosive environment by means of coating the metal by a layer of suitable organic, inorganic, or metallic compound[72, 80]. Organic coatings include paints, resins, lacquers, and varnishes with various formulations, which are applied on an appropriately prepared

metal surface. Inorganic coatings include enamels, glass linings, and conversion coatings. Since porcelain enamel coatings are inert in water, they are commonly used on appliances and plumbing fixtures. In industries where corrosion or contamination of the product is a concern, glass-lined metals are used. Conversion coatings are generally adherent corrosion product of metal of interest, which are produced by controlled corroding of the metal surface. Examples of conversion coating are aluminum oxide film on the aluminum metal produced by anodizing the aluminum and phosphatizing for the protection of automobile bodies.

To slow down or even prevent the corrosion, corrosion inhibitors are added in small concentrations to the corrosive environment. The effectiveness of the corrosion inhibitors depends on the metal to be protected as well as the chemical nature of the corrosive environment. One major concern about the corrosion inhibitors is their toxicity. Environmental regulations can limit the use of these agents. Inhibitors are classified into environmental conditioners and interface inhibitors. Environmental conditioners in general decrease the corrosivity of the environment by scavenging the corrosive substances from the environment. One example of this type of inhibitor is the use of hydrazine which in near-neutral and alkali solutions decreases the oxygen content leading to corrosion control[81]. On the other hand, interface inhibitors, control corrosion by forming a film at the metal / environment interface and inhibiting anodic and / or cathodic reactions. In Chapter 5, the efficiency of calcium gluconate and a few commercial inhibitors are examined using the new methodology based on wire triggers.

#### **1.4.4 Corrosion Detection**

In addition to corrosion inhibition and preventing, corrosion monitoring and detection are essential to control the corrosion and reduce the cost of corrosion and keep the structures healthy. Often corrosion reactions take time to initiate, therefore by accurate monitoring and predicting the

corrosion progress, appropriate control measures can be applied at early stages of corrosion. Visual, ultrasonic, radiographic, thermal imaging, and electrochemical techniques are among the major technologies used for corrosion monitoring and detection[77, 82].

The oldest and simplest method of corrosion inspection is visual inspection. Visual inspection can be done using naked eye for external surface inspection or using borescopes, fiberscopes, and video imaging systems for inspection of hard to access areas and internal surfaces. Although visual inspection is quick and inexpensive, its result is qualitative and depends on the inspector experience[82].

In corrosion detection by means of ultrasonic technology, high - frequency, (above 0.2 MHz), ultrasonic waves are sent and travel through material, and are reflected from interfaces such as the back surface of the material and where corrosion is in progress[83]. The reflected waves are used to detect any defect in the material. This technique is fast and can detect material and thickness loss with good resolution.

Radiographic inspection utilizes x-ray or  $\gamma$ -ray to inspect both surface and subsurface of materials. The short - wavelength waves penetrate through the material and are adsorbed depending on the thickness or the density of the material. The transmitted waves are recorded by either film or electronic devices. By interpretation of the resulting two-dimensional image, any variation in the material can be detected.

Thermographic imaging is utilized to detect the hidden corrosion based on the temperature distribution over the material. In this technique, infrared radiation emitted by the material is used to make a thermal image. The amount of the emitted radiation depends on the temperature and since many defects affect the thermal properties of the material, the thermal image can be used to detect any variation in the material. Although this technique is a practical

way to detect the hidden corrosion, the thermographic images are usually fuzzy and subject to interpretation.

In electrochemical corrosion detection methods, the electrochemical change by electron transfer is used for corrosion detection[77]. The most common type of these methods is based on the principles of galvanic corrosion. In galvanic corrosion sensors, two dissimilar metals are coupled galvanically and are kept isolated from each other. When an electrolyte condenses on the sensor, the gap between electrodes is bridged, as a result a current is developed which is used as a measure of corrosion[84].

In Chapter 6, corrosion of a thin wire is used to develop a passive wireless corrosion sensor. Various corrosion sensors have been developed based on fiber optics, electrochemical, and other techniques[85, 86]. Many of these sensors require power and complex wiring and hence they are expensive. Also some un-powered binary sensors based on radio frequency resonance phenomenon have been developed which utilize the corrosion of a surrogate wire[87, 88]. However, due to the analog nature of these devices, the response of the device changes with corrosion, which makes data interpretation problematic. To overcome these difficulties, a wireless sensor was developed using a standard radio-frequency identification (RFID), tag. This device is inexpensive, wireless, and requires no internal power. The response of the sensor can be easily read using an radio-frequency identification reader and the lack of the signal indicates that the wire is corroded.

## CHAPTER II

### THEORETICAL PREDICTION OF UV-VIS SPECTRA FOR MOLYBDENUM OXIDE CLUSTERS

In this chapter, the UV-Vis spectra of molybdenum oxide clusters are simulated theoretically by means of Time-Dependent Density Functional Theory (TDDFT) calculations. An overview of the computational methodology can be found in the introduction. The effects of cluster size and the variation of the formal charge of the molybdenum atoms on UV-Vis spectra are investigated. Adopting the geometrical parameters of yellow  $\beta$ -MoO<sub>3</sub>•H<sub>2</sub>O, the layered crystal structure of the molybdenum oxide is constructed step by step using chains and ribbons of connected tetrahedras containing 2, 3, and 4 molybdenum atoms. To easily identify the clusters the following numbering method has been adopted (see Figure 2-1):

abc(ij-kl,mn-op)

, where a is the number of layers, b is the number of chains in each layer, c is the number of molybdenum atoms in a chain, i, j, k, l, m, n, o, and p are the oxidation number of molybdenum atoms, "-" is used to separate the chains, and "," is used to separates the layers.

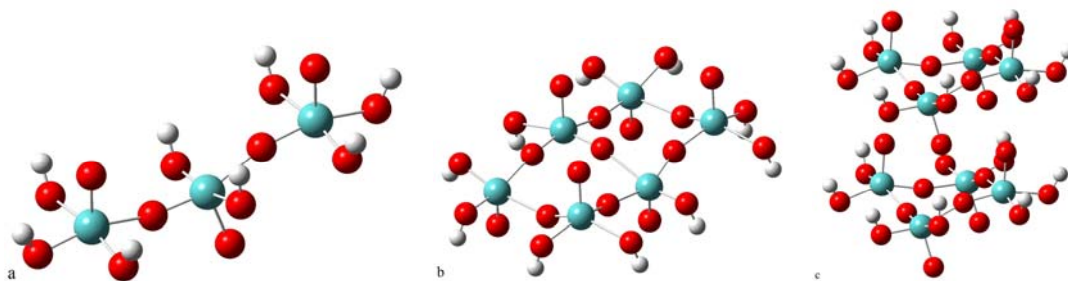


**Figure 2-1.** Molybdenum oxide cluster structures.

(a) 113(666) chain, (b) 123(666-666) ribbon, (c) 222(66-66,66-66) layer

## 2.1 Computational Procedure

All calculations were performed with Gaussian 09 software[89]. Molecular orbitals and electron density cube files were generated using standard cubegen and cubman utilities of Gaussian 09 software and visualized using GaussView 5 [90] software. Excitations were convoluted and UV-Vis spectra were visualized utilizing GaussSum software using a full width at half maximum (FWHM) of  $3000\text{ cm}^{-1}$  [91]. Except with explicitly noted, calculations were performed using Becke three parameter hybrid functional[92] with Lee, Yang and Parr correlation[93], which includes both local and non-local terms (B3LYP). The cc-pVTZ valence triple zeta basis set was employed for all oxygen and hydrogen atoms[94]. The molybdenum atoms were modeled with the Stuttgart-Dresden, (MWB28)[95], effective core potential and basis set augmented with two f-type and one g-type polarization functions with 0.265, 0.825, and 0.627 exponents respectively[16]. In some cases, other density functional theory functionals and basis sets were employed.

The time-dependent density functional theory calculations of the visible absorption spectra were performed in gas phase on clusters of different sizes keeping geometry parameters fixed. After which, the clusters geometries were optimized utilizing same method, basis sets, and core potential. time-dependent density functional theory calculations of the optical spectra were

performed on these optimized clusters. Vibrational frequency analysis was also performed to confirm that all stable structures have no imaginary modes.

## 2.2 Results and Discussion

Adopting the geometrical parameters from Kuzman and Purans [15], time-dependent density functional theory calculations were done for clusters of various sizes modeling the  $\beta$ - $\text{MoO}_3 \cdot \text{H}_2\text{O}$  structure. To model the cluster structure, polymeric chains, ribbons, and layer structures were studied (Figure 2-1). The stoichiometric relations were maintained by terminating all dangling bonds with hydrogen atoms. Finally, to fix the formal charge of selected molybdenum atoms to 5+, one hydrogen atom was attached to the oxygen atom connecting to the corresponding molybdenum atom.

For the molybdenum oxide, the valence band (VB) is comprised of the oxygen 2p orbitals, and the conduction band (CB) is the result of overlapped molybdenum 4d and 5s orbitals[96]. Thus, we expect to see an electron transfer from oxygen to molybdenum atoms from an optical excitation. By reducing one or more Mo(VI) atoms to Mo(V) in cluster by means of hydrogen insertion, a new band is generated (defect band, DB), which lays between valence and conduction bands, and is mainly composed of 4d and 5s orbitals of Mo(V) atoms (Figure 2-4). As a result, in addition to O-Mo electron transfers, Mo(V)-Mo(VI) electron transfers are also possible. In this dissertation, ligand to metal charge transfer (LMCT), and intervalence charge transfer (IVCT), terms are used for former and later types of electron transfers, respectively.

### 2.2.1 Chains

Keeping the structural parameters fixed at the expected crystallography locations, time-dependent density functional theory calculations were performed for chains consisting of two,

**Table 2-1.** HOMO and LUMO energies and HOMO to LUMO excitation wavelengths for chains. ( $E_H$ ) HOMO energy, ( $E_L$ ) LUMO energy, ( $\Delta E_{H-L}$ ) HOMO and LUMO energies difference, and ( $\lambda$ ) wavelength for HOMO to LUMO excitation

Chain	$E_H$ (eV)	$E_L$ (eV)	$\Delta E_{H-L}$ (eV)	$\lambda$ (nm)
112(66)	-7.17	-5.06	2.10	592
112(66)-opt	-8.76	-3.92	4.84	256
113(666)	-6.65	-4.81	1.85	670
113(666)-opt	-8.72	-4.02	4.71	263
114(6666)	-6.53	-4.86	1.66	747
114 (6666)-opt	-8.70	-4.26	4.44	280

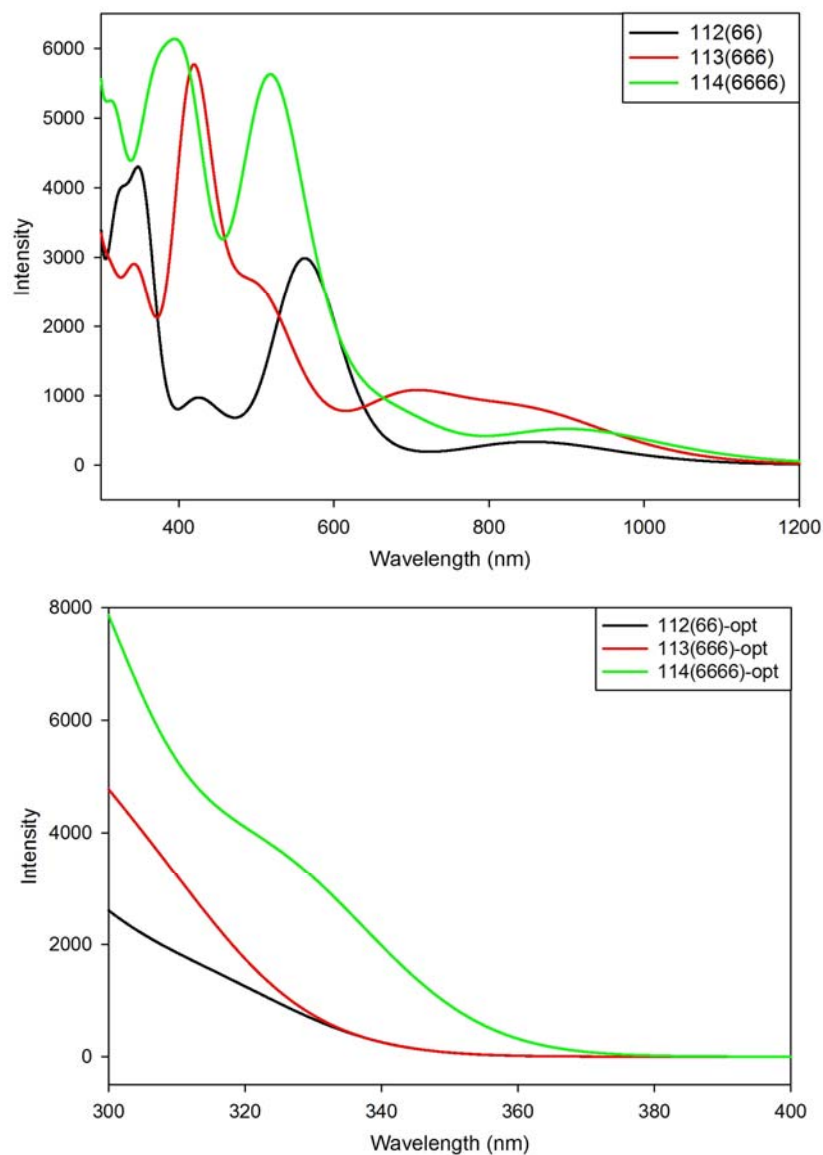


**Figure 2-2.** UV-Vis spectra of molybdenum oxide chains of various sizes (top) non-optimized, (bottom) optimized geometries

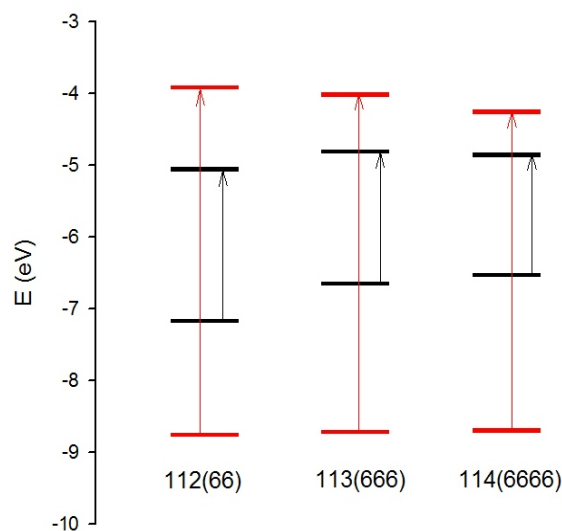


**Figure 2-3.** HOMO and LUMO energy levels for chain structures of various sizes (black) non-optimized, (red) optimized geometries

three, and four Mo(VI) atoms. Also, the clusters were optimized and time-dependent density functional theory calculations were performed for geometry optimized clusters. The energies of highest occupied molecular orbital (HOMO), and lowest unoccupied molecular orbital (LUMO), for these structures as well as expected wavelengths for HOMO to LUMO excitation are summarized in Table 2-1. From calculations, for HOMO to LUMO excitation, we expect absorptions at 592, 670, and 747 nm for 112(66), 113(666), and 114(6666) chains respectively.

The predicted gas phase spectra for these chains are shown in Figure 2-2. Three major peaks are distinguishable around 400, 600, and 800 nm. Upon optimization, all peaks shift to lower wavelengths (below 350 nm) and there is no peak at higher wavelengths, which is consistent with white color of the bulk material.

For non-optimized chains, although HOMO and LUMO energies systematically are increasing by the number of molybdenum atoms in chain, increasing of HOMO orbital energy is greater than that of LUMO orbitals (Figure 2-3), and hence  $\Delta E_{H-L}$  decreases with the number of

**Table 2-2.** HOMO and LUMO energies and HOMO to LUMO excitation wavelengths for 112 chains.

( $E_H$ ) HOMO energy, ( $E_L$ ) LUMO energy, ( $\Delta E_{H-L}$ ) HOMO and LUMO energies difference, and ( $\lambda$ ) wavelength for HOMO to LUMO excitation.

$\alpha$  and  $\beta$  indicate spin up and spin down electrons respectively.

Chain	$E_H$ (eV)		$E_L$ (eV)		$\Delta E_{H-L}$ (eV)		$\lambda$ (nm)	
	$\alpha$	$\beta$	$\alpha$	$\beta$	$\alpha$	$\beta$	$\alpha$	$\beta$
112(66)	-7.17	NA	-5.06	NA	2.10	NA	592	NA
112(66)-opt	-8.76	NA	-3.92	NA	4.84	NA	256	NA
112(56)	-5.86	-7.05	-4.10	-3.90	1.77	3.16	701	393
112(56)-opt	-6.30	-8.54	-3.80	-3.77	2.50	4.76	495	260

molybdenum atoms and corresponding absorption peak shifts to higher wavelengths. By increasing the number of molybdenum atoms in the chain, more energy states are available in both valence and conduction bands resulting in wider energy bands, and hence smaller band gaps, shifting the absorptions to higher wavelengths.

When chains first were optimized, time-dependent density functional theory calculations show a dramatic shift of absorption peaks to shorter wavelengths. The absorption wavelengths for HOMO to LUMO excitation are 256, 263, and 280 nm for 112(66)-opt, 113(666)-opt, and 114(6666)-opt respectively. This is reasonable due to stabilization of chains due to the geometry optimizations. Optimized structures are distorted from layered structure of the bulk material to minimize the energy.

Calculations shows that HOMO energy increases and LUMO energy decreases with the number of molybdenum atoms, (Figure 2-3). Similar to non-optimized chains, absorptions shift to higher wavelengths.

### 2.2.1.1 112 Chains

As mentioned above, time-dependent density functional theory calculations were performed for 112(66) chain utilizing B3LYP method using described basis sets and pseudo

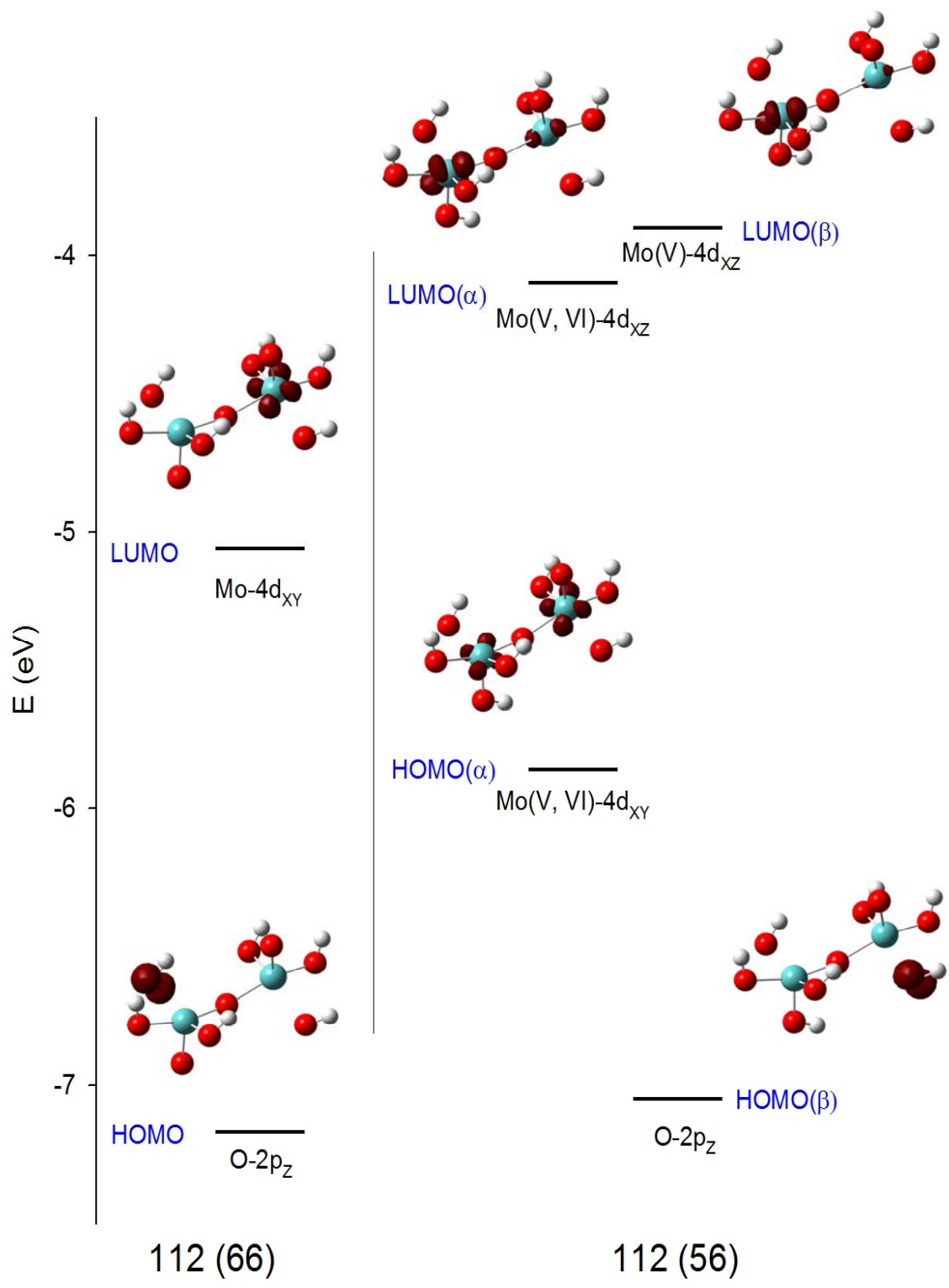
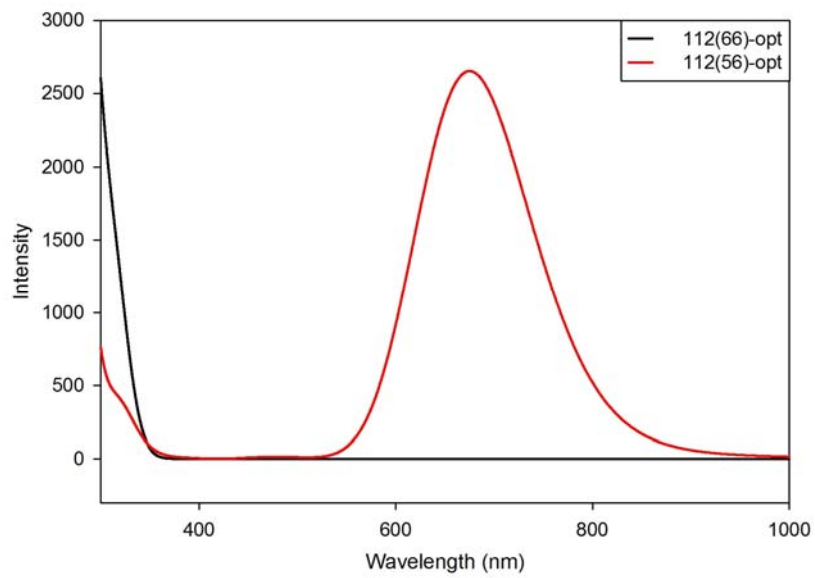
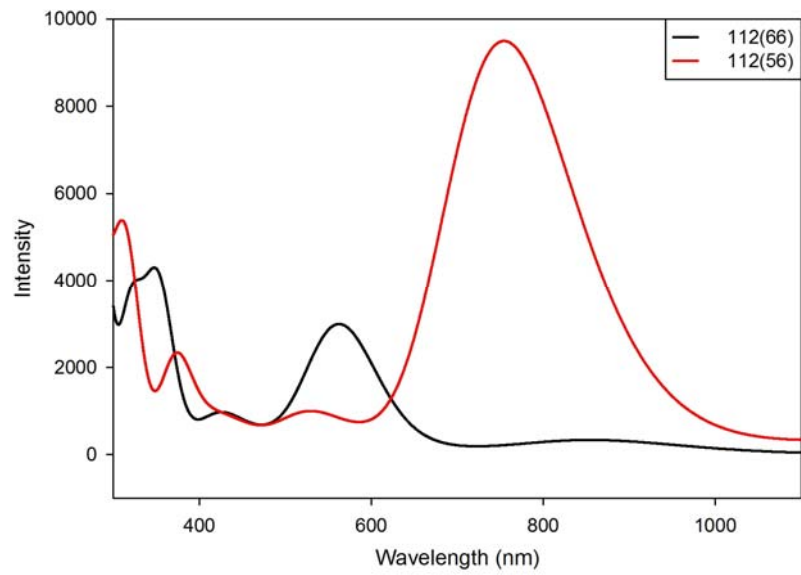


**Figure 2-4.** HOMO and LUMO energy levels for 112(66) and 112(56) chains.

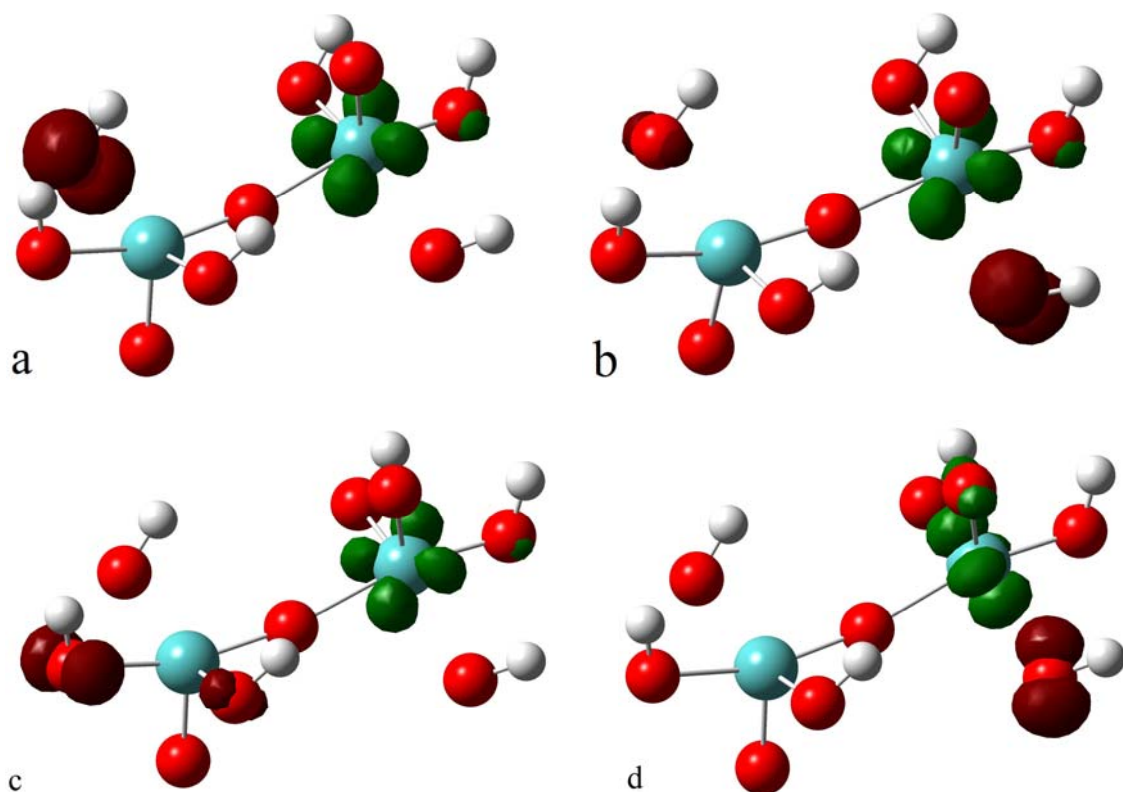
potential. Also, 112(66) chain was first optimized utilizing same method, basis sets, and pseudo potential and time-dependent density functional theory calculation then performed for optimized chain structure. Furthermore, one Mo(VI) atom in the 122(66) chain was reduced to Mo(V) by hydrogen insertion, resulting in 122(56) chain. Time-dependent density functional theory calculations were also performed for 112(56) and geometrically optimized 112(56)-opt chains.

Table 2-2, summarizes the HOMO and LUMO energies for these chains as well as corresponding absorption wavelengths for HOMO to LUMO excitations. Optimization of 112(66) chain, decreases the HOMO and increases the LUMO energies by 1.59 and 1.14 eV respectively and overall, band gap increases by 2.74 eV and hence the absorption peak for the HOMO to LUMO excitation shifts to lower wavelength of 256 nm. As one can see from Figure 2-4, valence band for 112(66) chain is composed of O-2p orbitals and conduction band is composed of Mo-4d orbitals. Upon reducing of one Mo(VI) atom to Mo(V) by means of hydrogen insertion, a new band (defect band, DB) is generated which is energetically lays between valence and conduction bands. This band mainly comprised of Mo(V)-4d orbitals and facilitates new excitations at higher wavelengths.

For 112(66) chain, calculations predicts four main absorptions at 351, 431, 564, and 860 nm, with strongest contributions from HOMO-3 to LUMO+2, HOMO-4 to LUMO, HOMO-1 to LUMO, and HOMO to LUMO excitations respectively (Figure 2-5). Valence band is composed of O-2p orbitals and conduction band is composed of Mo-4d orbitals and hence as expected all excitations are associated with O to Mo electron density transfer (Figure 2-6). For the absorptions at 351 and 564 nm, electron density transfer is from the oxygen atom which is connected to the molybdenum atom, so the associated absorption peak is stronger than those absorptions at 431 and 860 nm where electron density transitions are from farther oxygen atoms. Upon optimization of the chain structure, the structures are bent to minimize the cluster structure, band gap increases



**Figure 2-5.** UV-Vis spectra for 112 chains.  
 (top) non-optimized, (bottom) optimized structures



**Figure 2-6.** Electron density transfers for 112(66) chain. excitations at: (a) 860, (b) 564, (c) 431, and (d) 351 nm (green and brown colors indicate electron density increasing and decreasing, respectively)

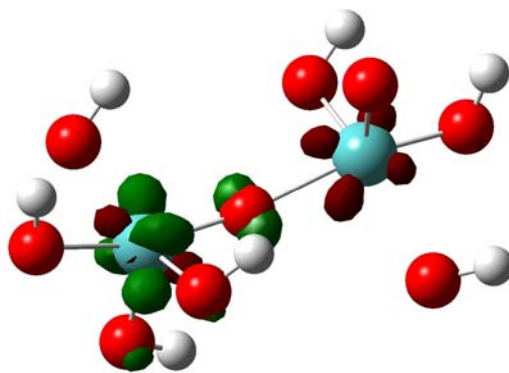


**Figure 2-7.** Electron density transfer for excitation at 750 nm for 112(56) chain

and hence peaks at higher wavelengths disappear. The first absorption peak appears at 319 nm with main contribution from HOMO to LUMO and HOMO-1 to LUMO excitations. Similar to non-optimized chain, electron density transfer for these excitations are of the ligand to metal charge transfer type.

For 112(56) chain, calculations predict five major absorption peaks at 318, 375, 513, 750, and 1264 nm with strongest contributions from HOMO-3( $\alpha$ ) to LUMO+4( $\alpha$ ), HOMO-3( $\beta$ ) to LUMO+1( $\beta$ ), HOMO-1( $\alpha$ ) to LUMO+1( $\alpha$ ), HOMO( $\alpha$ ) to LUMO+1( $\alpha$ ), and HOMO( $\alpha$ ) to LUMO+2( $\alpha$ ) excitations respectively. Similar to 112(66) chain, excitations at 318, 375, 513, and 1264 nm are associated with O to Mo electron density transfer. As mentioned above, when reducing one molybdenum atom to Mo(V), a defect band is generated and new type of excitations involving Mo(V) orbitals are expected. Figure 2-5 shows a strong absorption at 750 nm, a closer look at the electron density transfer (Figure 2-7) for this absorption reveals that an intervalence charge transfer is associated with this excitation. Mulliken atomic charge distribution confirms that as expected, the charge transfer is of the Mo(V) to Mo(VI) form. Similar to the 122 (66) chain, upon optimization of the 112(56) structure, band gap increases resulting in the shift of the absorption peaks to the lower wavelengths and the absorption peak corresponding to intervalence charge transfer shifts to 674 nm.

### 2.2.1.2 113 Chains

Similar to 112 chains, time-dependent density functional theory calculations were performed for 113 chains with and without geometry optimization. To study the intervalence charge transfer in these chains, one or two molybdenum atoms were reduced to Mo(V) by hydrogen insertion. As illustrated in Figure 2-8, for the non-optimized chains, there are two main absorption wavelength regions at around 420 and 750 nm and one more absorption for 113(565) chain at around 1400 nm. Investigation of electron densities reveals that for the 113(666), as

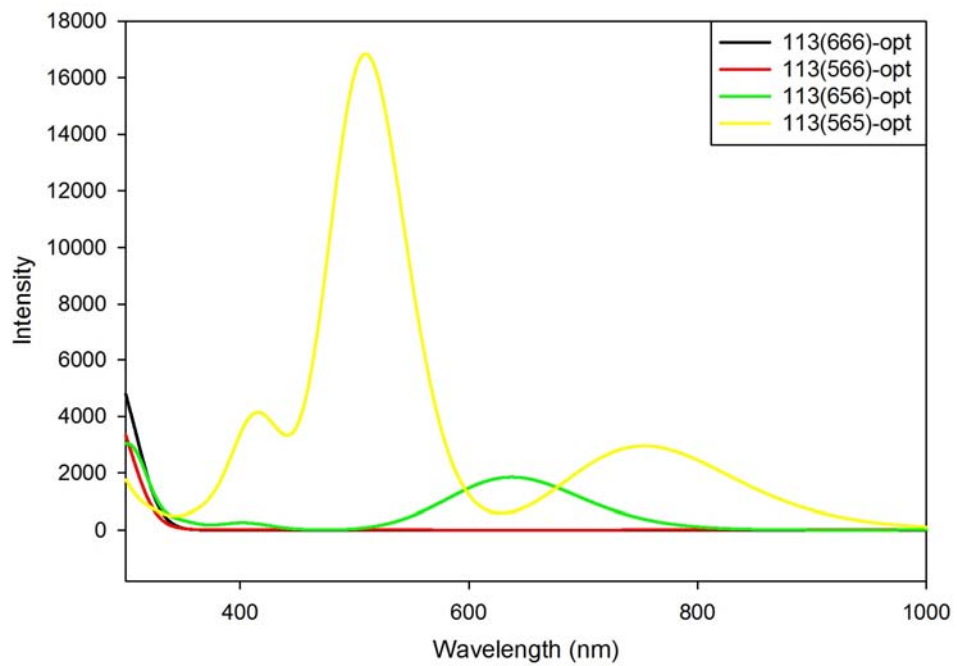
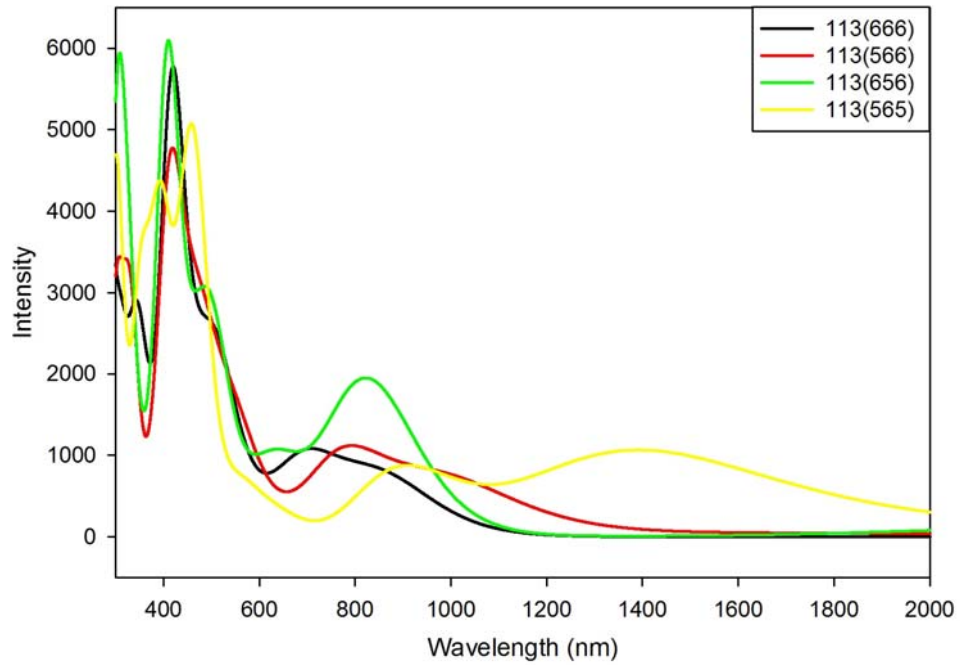


**Figure 2-8.** UV-Vis spectra for 113 chains.

(top) non-optimized, (bottom) optimized structures

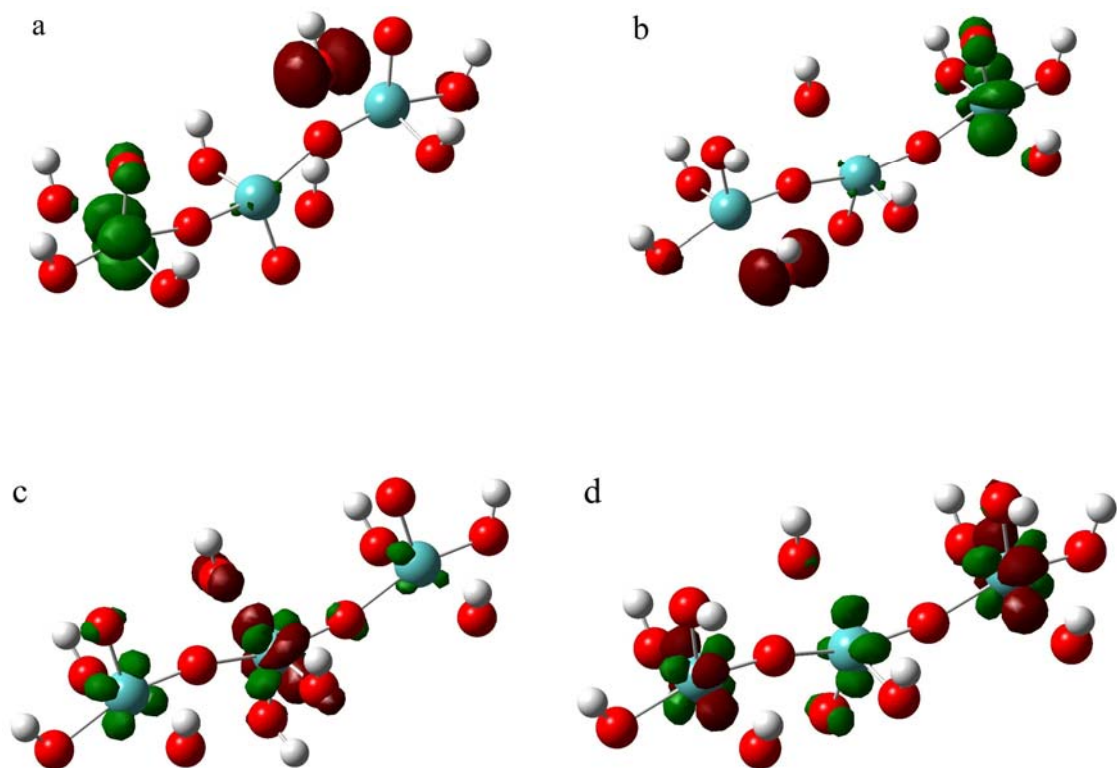


**Figure 2-9.** Examples of ligand to metal (LMCT) and intervalence (IVCT) charge transfer for 113 chains.

(a) LMCT for 113(666), (b) LMCT for 113(566)

(c) IVCT for 113(656), (d) IVCT for 113(565)

expected all the excitations are associated with ligand to metal charge transfer (O to Mo). In the case of 113(566) chain, the absorptions in the visible wavelengths are also due to ligand to metal charge transfer, while HOMO( $\alpha$ ) to LUMO( $\alpha$ ) excitation is associated with intervalence charge transfer (Mo(V) to Mo(VI)) which appears as a weak absorption at 1800 nm. For the 113(656) and 113(565) chains, the absorptions associated with intervalence charge transfer appear at 750 and 1400 nm respectively and all the other absorptions below 750 nm are due to ligand to metal charge transfer. Examples of electron density transfers of both types are demonstrated in Figure 2-9.

Upon geometry optimization of 113 chains, band gap increases and hence all the absorption peaks shift to lower wavelengths. For the 113(666)-opt and 113(566)-opt chains, all the peaks appear out of visible wavelengths while for 113(656)-opt and 113(565)-opt chains strong peaks corresponding to intervalence charge transfer appear at visible wavelengths. For the 113(565)-opt chain, the Mo(V)/Mo(VI) ratio is twice the ratio for other multivalence 113 chains and hence more energy states are available in defect band. This increases the probability of excitation from the defect band energy states resulting in stronger absorption peak for excitations associated with intervalence charge transfer (Figure 2-8).

### 2.2.1.3 114 Chains

The result of time-dependent density functional theory calculations on 114 chains are in agreement with the results for 112 and 113 chains. For the case of non-optimized chains, there are two main absorptions below 600 nm which are associated with ligand to metal charge transfer. For the 114(6666) chain, HOMO to LUMO excitation, also due to ligand to metal charge transfer appears at 908 nm as a weak absorption. For the 114(5666) chain, in addition to absorptions below 600 nm, there are two weak absorptions at 1548 and 2239 nm for the HOMO-1( $\alpha$ ) to LUMO+1( $\alpha$ ) and HOMO-1( $\alpha$ ) to LUMO( $\alpha$ ) excitations, respectively which are associated with intervalence charge transfer. Similarly, absorptions associated with the intervalence charge transfer for the 124(6566) cluster appear as two weak peaks at 1142 and 1367 nm due to the HOMO-1( $\alpha$ ) to LUMO+1( $\alpha$ ) and HOMO-1( $\alpha$ ) to LUMO( $\alpha$ ) excitations, respectively. There is an absorption for the 114(5656) chain at 1200 nm with main contribution from HOMO to LUMO+5 excitation associated with intervalence charge transfer. This absorption, due to higher Mo<sup>5+</sup>/Mo<sup>6+</sup> ratio of the chain is much stronger comparing to the absorptions corresponding to intervalence charge transfer for the other chains (Figure 2-10). Examples of ligand to metal and intervalence charge transfers for these chains are illustrated in Figure 2-11.

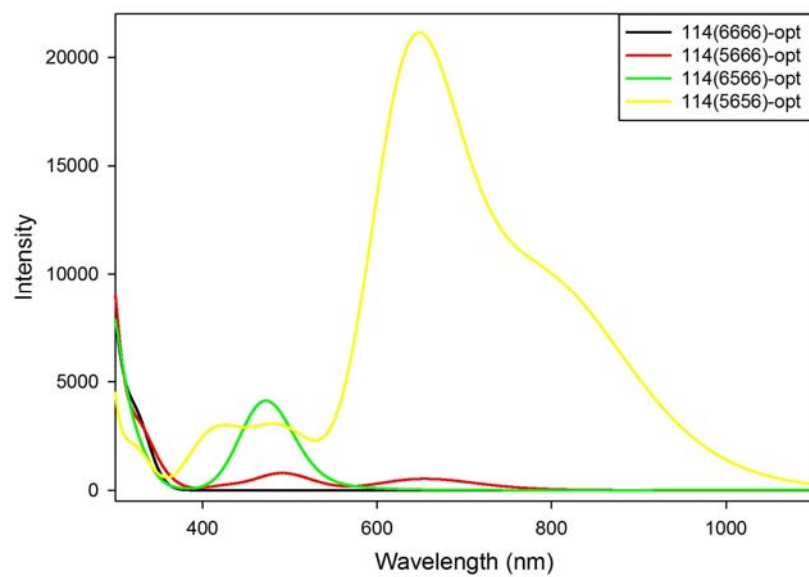
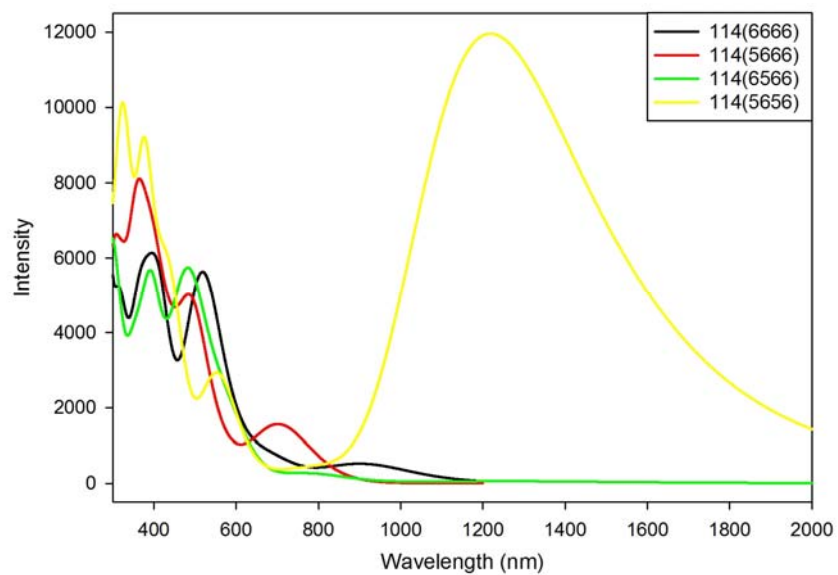


**Figure 2-10.** UV-Vis spectra for 114 chains.  
 (top) non-optimized, (bottom) optimized structures

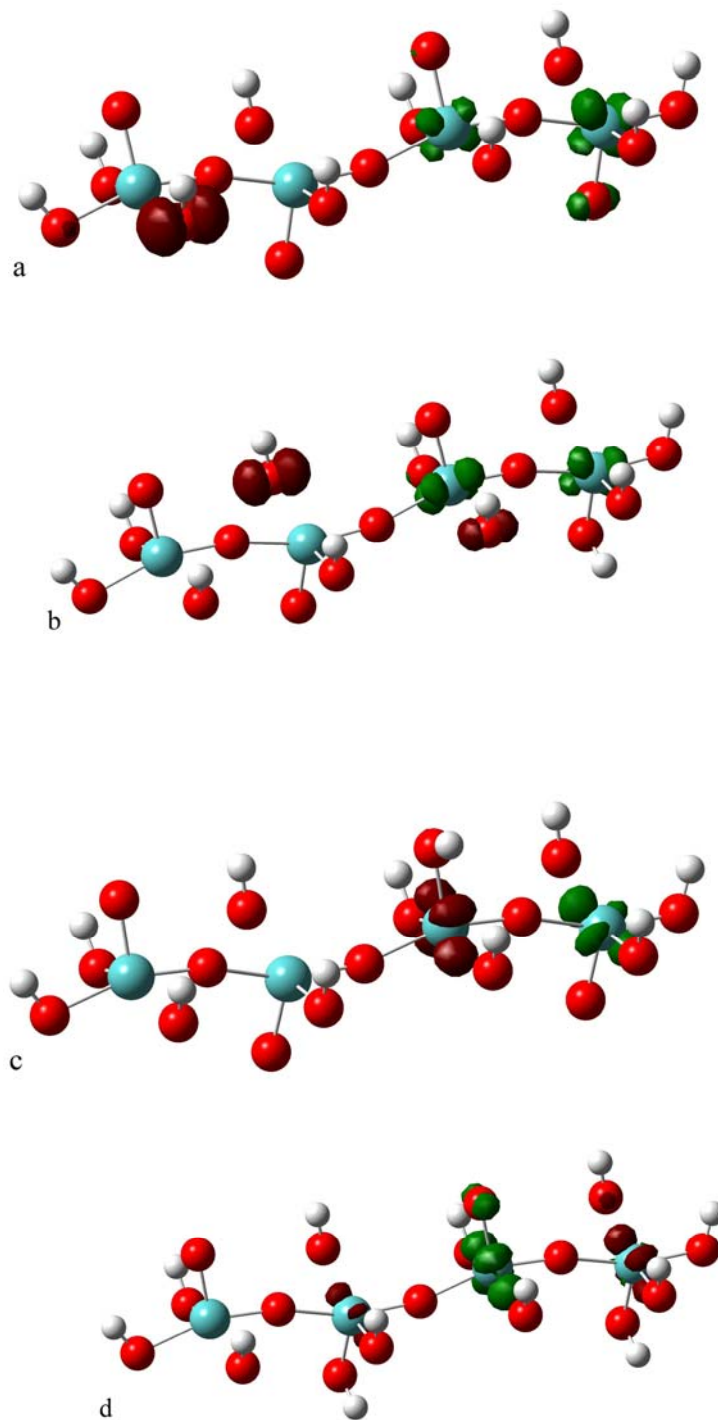


**Figure 2-11.** Examples of ligand to metal (LMCT) and intervalence (IVCT) charge transfers for 114 chains.

(a) LMCT for 114(6666), (b) LMCT for 114(5666),  
(c) IVCT for 114(6566), and (d) IVCT for 114(5656) chains

Upon optimization of the chains, calculation results reveal that all absorptions associated with ligand to metal charge transfer, due to larger band gaps, shift to lower wavelengths out of visible range and peaks associated with intervalence charge transfer shift to lower wavelengths in visible range (Figure 2-10). For the 114(5666)-opt cluster, HOMO( $\alpha$ ) to LUMO+1( $\alpha$ ) and HOMO( $\alpha$ ) to LUMO( $\alpha$ ) absorptions, both associated with intervalence charge transfer, appear at 493 and 654 nm, respectively. For the 114(6566)-opt cluster, there are three absorptions due to intervalence charge transfer, one strong absorption at 476 nm associated with HOMO( $\alpha$ ) to LUMO+3( $\alpha$ ) excitation and two weaker absorptions at 558 and 660 nm associated with HOMO( $\alpha$ ) to LUMO+1( $\alpha$ ) and HOMO( $\alpha$ ) to LUMO( $\alpha$ ) excitations, respectively. And finally, for the 114(5656)-opt chain, the peaks associated with intervalence charge transfer appear at 423 nm due to HOMO to LUMO+4 excitation and a broad strong absorption at 644 nm with main contributions from HOMO to LUMO and HOMO to LUMO+2 excitations.

## **2.2.2 Ribbons**

Ribbons were constructed by connecting two chains of two, three, and four molybdenum atoms. Similar to chains, time-dependent density functional theory calculations were performed for non-optimized and optimized ribbons. Figure 2-12 shows that, there are three major absorptions at approximately 340, 430, and 520 nm for non-optimized ribbons and one major absorption at about 320 nm for the optimized ribbons. Investigation of electron density transfers reveals that as expected all the excitations are associated with ligand to metal charge transfer which can be happen within a chain or between two chains. For the optimized structures, similar to the chains, due to larger band gaps, all the absorption peaks were shifted to the lower wavelengths.

### **2.2.2.1 122 Ribbons**

As illustrated in Figure 2-13, for the 112(66-66) ribbon, HOMO to LUMO excitation appears as a small peak at 517 nm and three other major absorption peaks are distinguished at

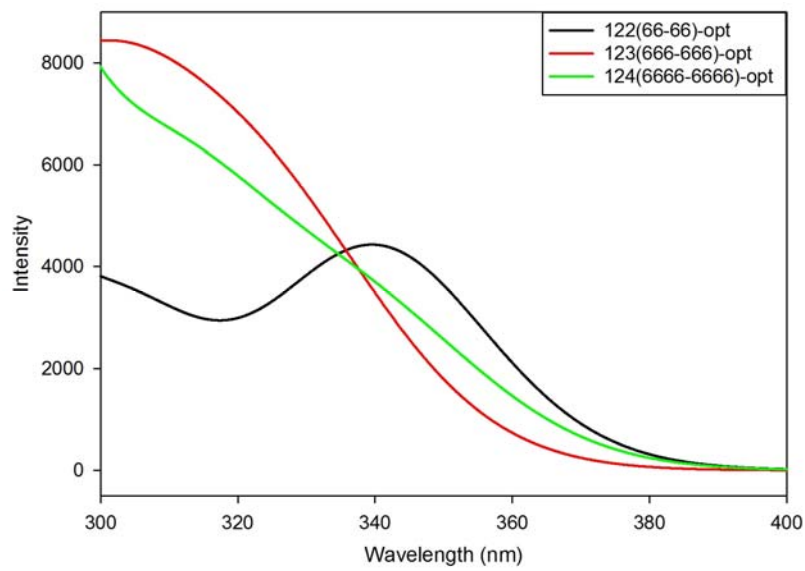
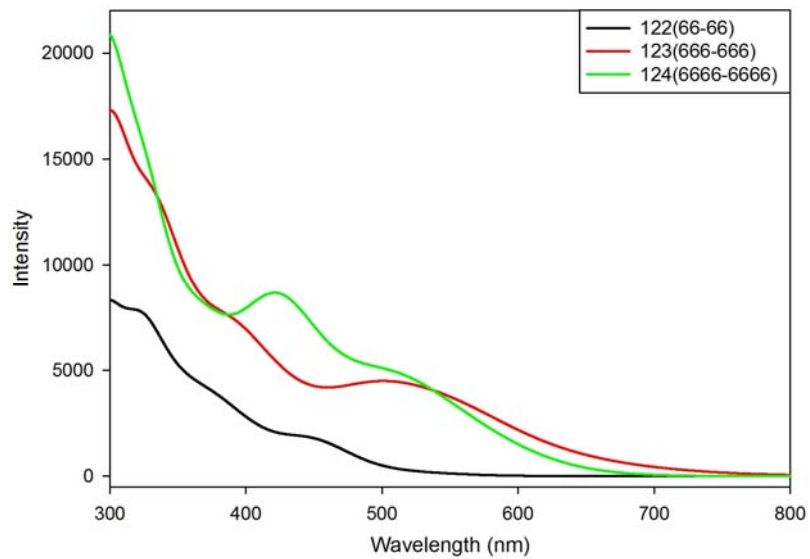


**Figure 2-12.** UV-Vis spectra for ribbons of various sizes.  
 (top) non-optimized, (bottom) optimized structures

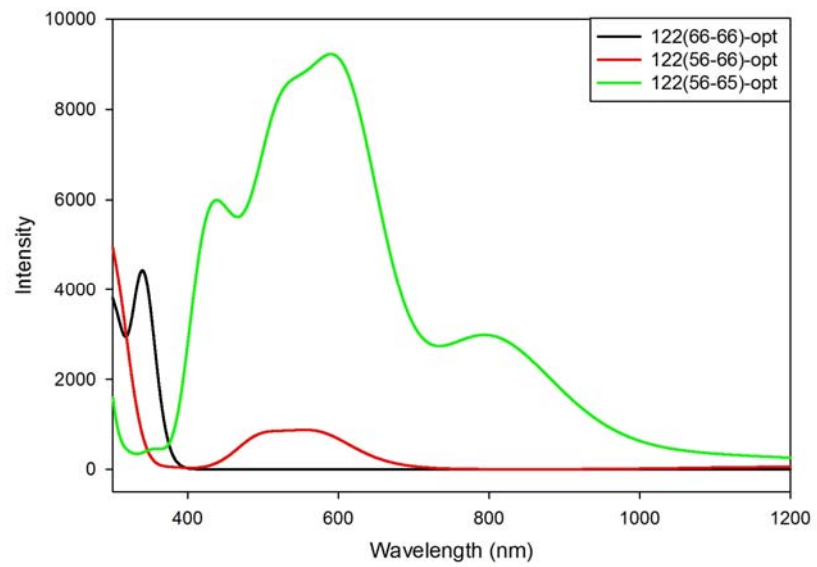
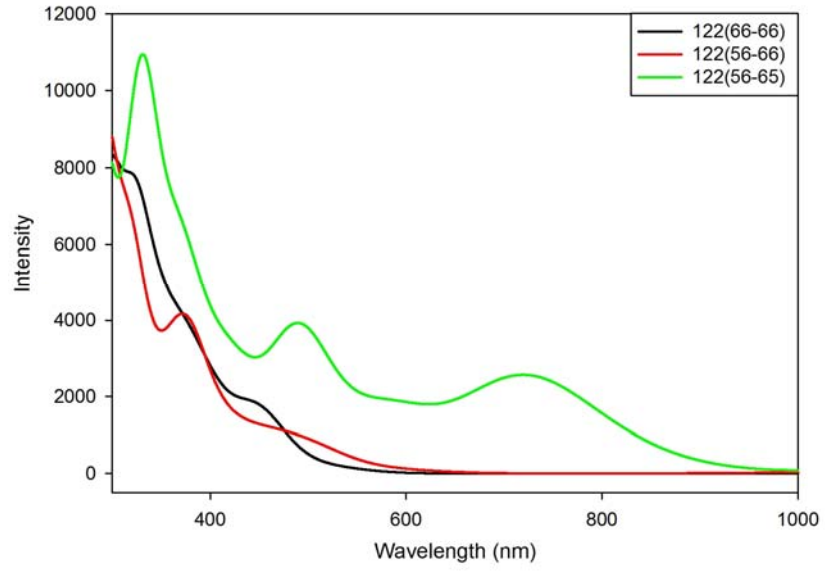


**Figure 2-13.** UV-Vis spectra for 122 ribbons.  
(top) non-optimized, (bottom) optimized structures

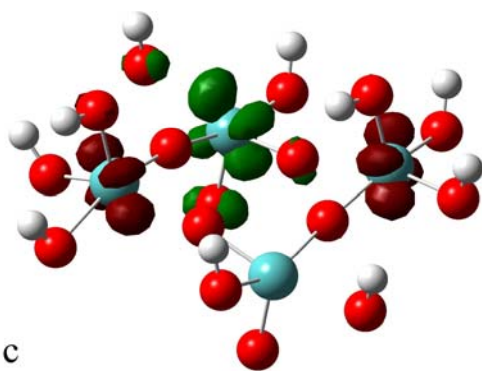
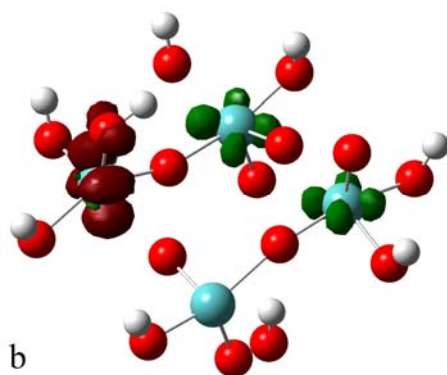
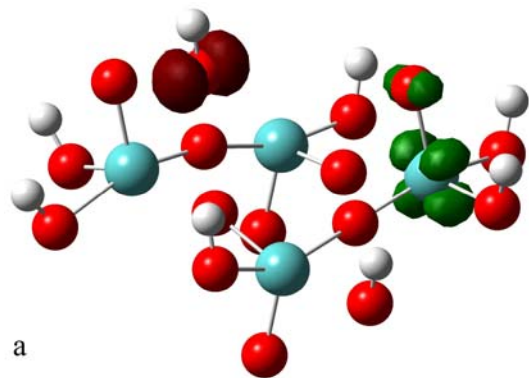


**Figure 2-14.** Examples of ligand to metal (LMCT) and intervalence (IVCT) charge transfers for 122 ribbons.

(a) LMCT for 122(66-66), (b) IVCT for 122(56-66), and (c) IVCT for 122(56-65)

347, 377, and 450 nm with main contributions from HOMO-6 to LUMO, HOMO-2 to LUMO+1, and HOMO-1 to LUMO+1 excitations respectively. Upon geometry optimization, due to larger band gap, all peaks shift to lower wavelengths and HOMO to LUMO excitation peak appears at 362 nm. For this ribbon structure, as expected, all the excitations are associated with ligand to metal charge transfer.

As discussed earlier for chains, reduction of one or more Mo(VI) atoms to Mo(V), generates the defect band which in turn facilitates the intervalence charge transfer. Since the defect band lays between valence and conduction bands, comparing to absorptions associated with ligand to metal charge transfer, the absorptions due to intervalence charge transfer appear at higher wavelengths. For the non-optimized and optimized 122(56-66) ribbons, these excitations are at 512 nm for non-optimized and 497 and 572 nm for optimized structures, respectively. By reducing of two Mo(VI) atoms in the structure, the probability of intervalence charge transfer increases. The absorption peaks for the non-optimized 122(56-65) ribbon at about 490 and 710 nm and peaks for optimized 122(56-65) ribbon at about 440, 600, and 800 nm are more intense than the corresponding absorption for 122(56-66) ribbon (Figure 2-13). Examples of ligand to metal charge transfer and intervalence charge transfer for 122 ribbons are illustrated in Figure 2-14. As can be seen from this figure, electron density transfer can occur within one chain or between two chains in the ribbon structure.

#### **2.2.2.2 123 Ribbons**

123 ribbons are constructed by attaching two chains of three molybdenum atoms. Figure 2-15 shows that the resulting spectra from time-dependent density functional theory calculations are similar for 123(666-666) and 123(566-666) ribbons with three major absorptions at around 330, 400, and 500 nm; also similar spectra are predicted for 123(656-666) and 123(565-656) ribbons with three major absorptions at around 350, 500, and 800 nm.

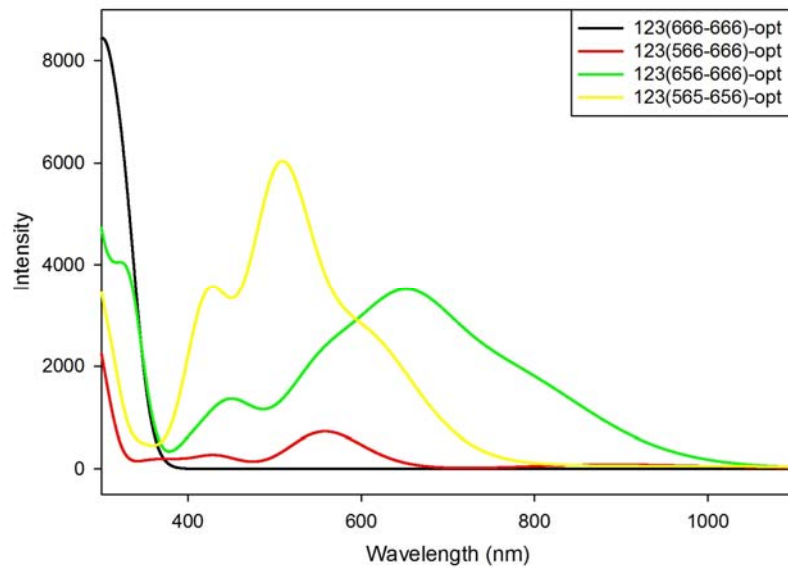
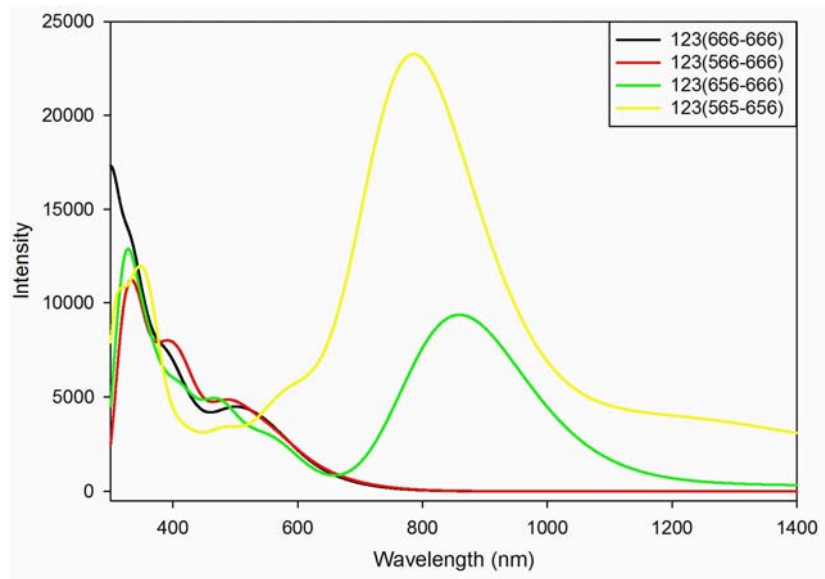


**Figure 2-15.** UV-Vis spectra for 123 ribbons.  
(top) non-optimized, (bottom) optimized structures

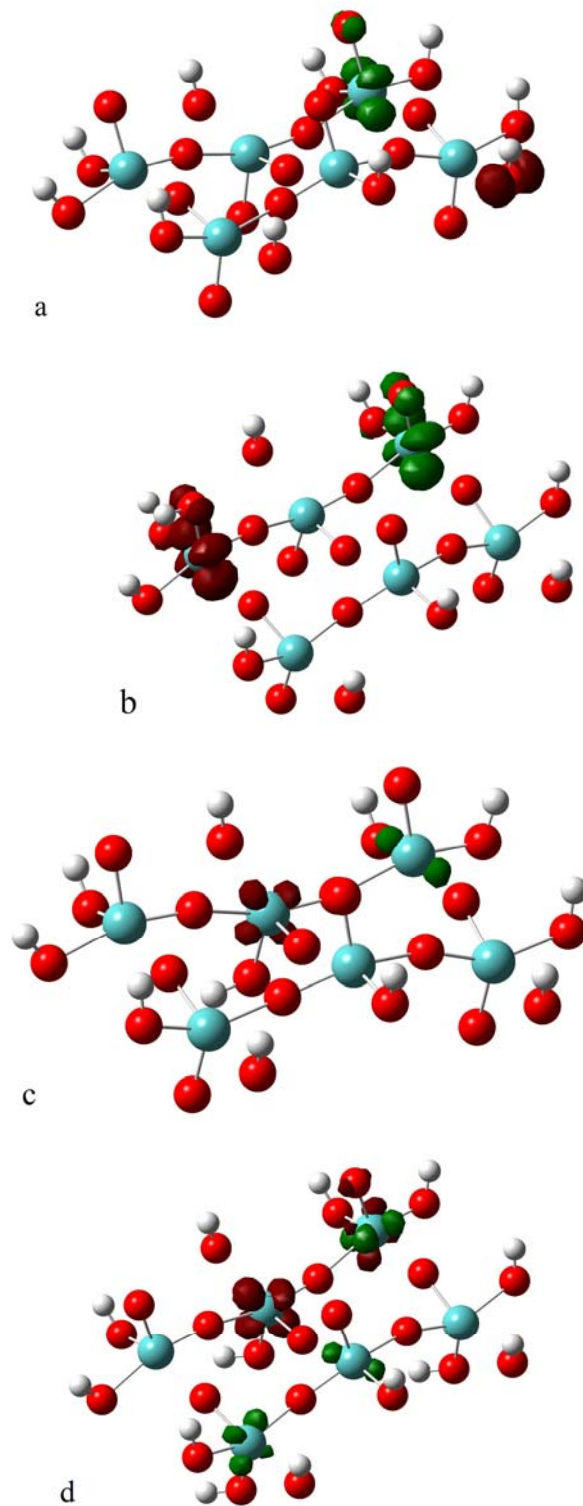


**Figure 2-16.** Examples of ligand to metal (LMCT) and intervalence (IVCT) charge transfers for 123 ribbons.

(a) LMCT for 123(666-666), (b) IVCT for 123(566-666),  
(c) IVCT for 123(656-666), and (d) IVCT for 123(565-656) ribbons

Electron density transfer investigation for these major absorptions reveals that, all the excitations for the 123(666-666) are associated with ligand to metal charge transfer which upon optimization of the ribbon structure shift to below 350 nm. The spectra for the 123(566-666) ribbon is very similar to that of 123(666-666) ribbon; all absorptions in visible range are associated with ligand to metal charge transfer and HOMO to LUMO excitation which is associated with intervalence charge transfer appears as a weak absorption at 1708 nm. For this ribbon, geometry optimization distorts the structure from flat bulk material structure to minimize the energy, all the excitations associated with ligand to metal charge transfer shift to below 300 nm. HOMO to LUMO excitation which is shifted to 891 nm, along with two new absorptions at 435 and 566 nm are associated with intervalence charge transfer.

The spectra for 123(656-666) and 123(565-656) ribbons are similar with a strong and broad absorption above 700 nm and two weaker absorptions at about 350 and 500 nm. The investigation of electron density transfers shows that for both ribbons, absorptions below 500 nm are associated with ligand to metal charge transfer and the absorptions at higher wavelengths are associated with intervalence charge transfer. Also, it can be seen from Figure 2-15 that the ratio of the strongest absorptions intensities for these ribbons at around 800 nm, is approximately 3, which is in agreement with the ratio of the number of Mo(V) atoms in the ribbon structures. Examples of both ligand to metal charge transfer and intervalence charge transfer for 123 ribbons are shown in Figure 2-16.

### **2.2.2.3 124 Ribbons**

Similar to the case of 123 ribbons, the predicted spectra by calculations for 124(6666-6666) and 124(5666-6666) ribbons are similar with three major absorptions at about 330, 400, and 500 nm and spectra for 124(6566-6666) and 124(6565-5656) ribbons are similar with four major absorptions at about 330, 350, 450, and 800 nm (Figure 2-17).

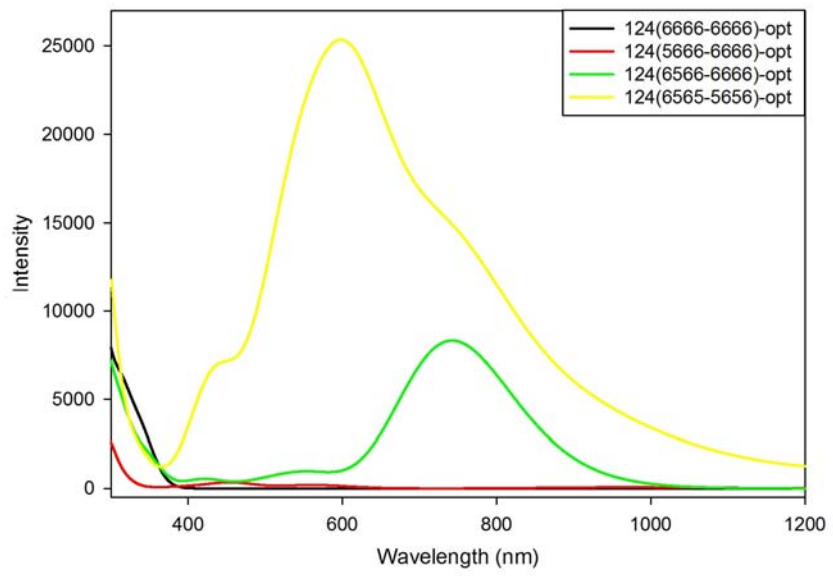
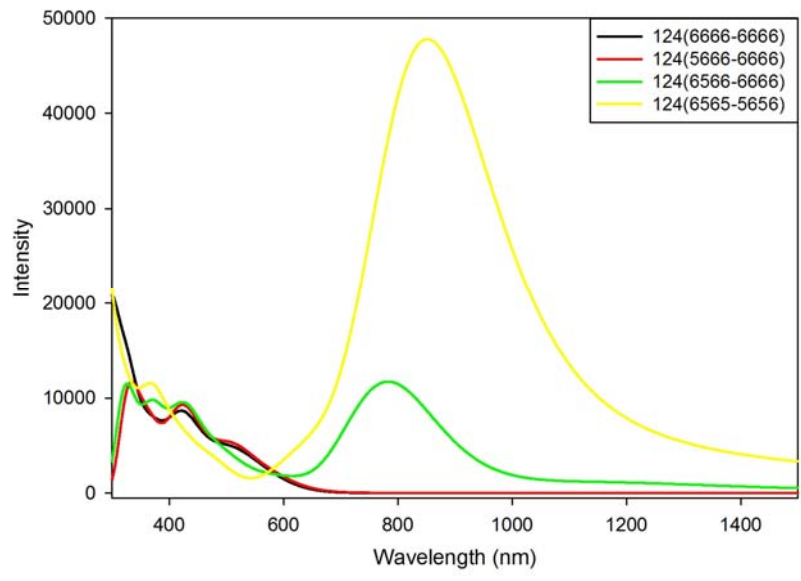


**Figure 2-17.** UV-Vis spectra for 124 ribbons.  
 (top) non-optimized, (bottom) optimized structures

The absorptions for the 124(6666-6666) ribbon are at 347, 377, and 450 nm with major contributions from HOMO-6 to LUMO, HOMO-2 to LUMO+1, and HOMO-1 to LUMO+1 excitations respectively, which are associated with ligand to metal charge transfer. These absorptions, upon geometry optimization of the ribbon, shift to lower wavelengths below 400 nm. The spectra for 124(5666-6666) ribbon is very similar to 124(6666-6666) ribbon, except that for this ribbon HOMO( $\alpha$ ) to LUMO( $\alpha$ ) excitation which is associated with intervalence charge transfer, appears as a small absorption at 1518 nm. Upon optimization of the ribbon geometry, HOMO( $\alpha$ ) to LUMO( $\alpha$ ) excitation peak shifts to 965 nm, peaks associated with ligand to metal charge transfer shift below 400 nm, and new absorptions at 456 and 564 nm are associated with intervalence charge transfer.

Figure 2-17 shows that for 124(6566-6666) and 124(6565-5656) ribbons, there is a strong broad absorption at about 800 nm with main contribution from HOMO( $\alpha$ ) to LUMO( $\alpha$ )+7 and HOMO( $\alpha$ )-1 to LUMO( $\alpha$ )+4 excitations respectively, and a few other absorptions below 600 nm. Electron density transfer investigations for these absorptions reveals that for these ribbons, the absorption at about 800 nm is associated with intervalence charge transfer and all the other absorptions at lower wavelengths are associated with ligand to metal charge transfer. Some of the electron density transfers for 124 ribbons are represented in Figure 2-18.

Upon optimization of the ribbon, similar to the other clusters, structure distorts from flat geometry to minimize the energy, all the absorptions associated with ligand to metal charge transfer shift to lower wavelengths below 305 nm and the absorptions at wavelengths higher than 400 nm are due to intervalence charge transfer. The spectra for the 124(6565-5656)-opt ribbon consists of five major absorptions at 310, 369, 445, 635, and 845 nm, for this ribbon more Mo(V) atoms are available and hence more absorptions due to intervalence charge transfer are expected. Electron density transfer investigations show that, absorptions above 369 nm are associated with intervalence charge transfer while the absorptions below are associated with ligand to metal

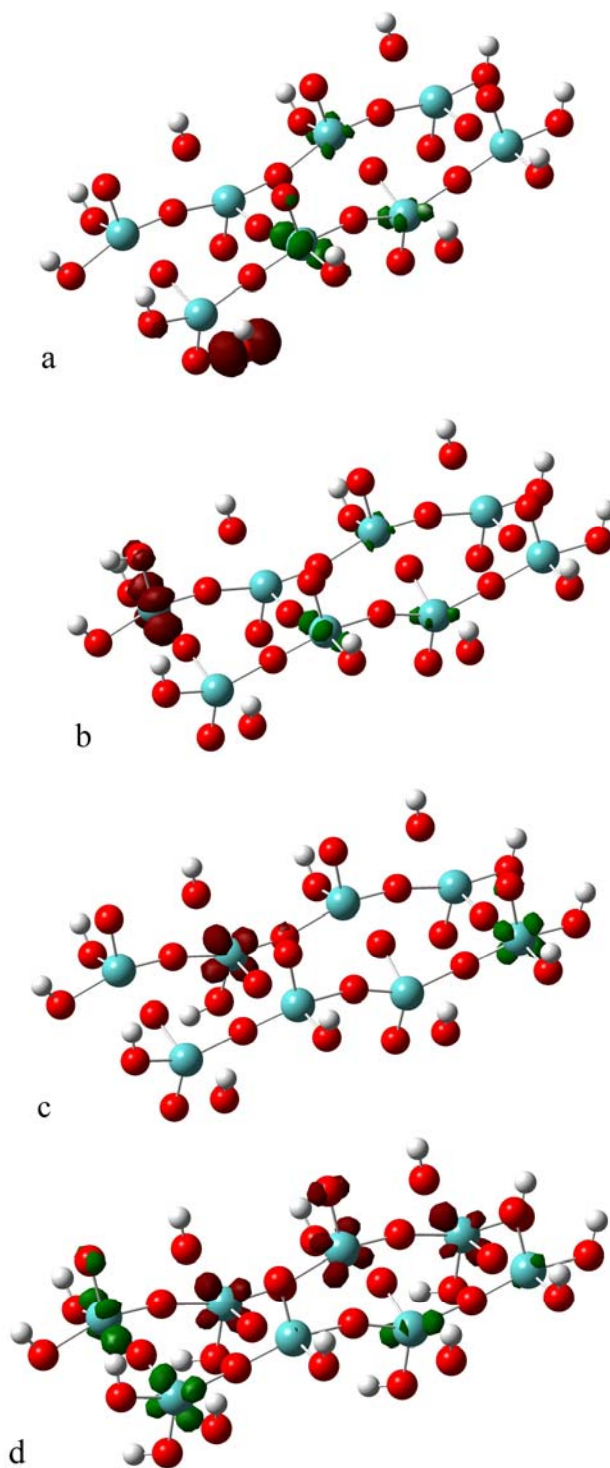


**Figure 2-18.** Examples of ligand to metal (LMCT) and intervalence (IVCT) charge transfers for 124 ribbons.

(a) LMCT for 124(6666-6666), (b) IVCT for 124(5666-6666),  
(c) IVCT for 124(6566-6666), and (d) IVCT for 124(6565-5656) ribbons

charge transfer. Also the ratio of intensities of the absorptions at around 800 nm for 124(6565-5656) and 124(6566-6666) ribbons is approximately 4, directly reflecting the ratio of the number of Mo(V) atoms in the ribbon structures.

### 2.2.3 Layers

To simulate the layer structure of the molybdenum oxide, one 122 ribbon was placed over another 122 ribbon (Figure 2-1). Time-dependent density functional theory calculations were performed for 222(66-66,66-66) layer with all molybdenum atoms of 6+ valence and 222(56-66,66-66) layer with one Mo(VI) atom reduced to Mo(V). As seen from Figure 2-19, similar to chains and ribbons, the spectra for the layer where one terminal Mo(VI) is reduced to Mo(V) is very similar to the spectra of the layer where all the molybdenum atoms have 6+ valence.

For the 222(66-66,66-66) layer, in addition to HOMO to LUMO excitation which appears as a small peak at 768 nm, three major absorptions at 377, 415, and 476 nm are predicted with main contributions from HOMO-9 to LUMO+1, HOMO-3 to LUMO+7, and HOMO-1 to LUMO+7 excitations respectively (Figure 2-19). Electron density transfer analysis reveals that, all these absorptions are associated with ligand to metal charge transfer either within a ribbon or between two ribbons in the layer structure. By reducing one terminal Mo(VI) atom to Mo(V) by means of hydrogen insertion, intervalence charge transfer is also possible. In fact electron density transfer analysis for the 222(56-66,66-66) layer structure shows that the absorption at 414 nm along with two weaker absorptions at 2176 and 3410 nm are associated with intervalence charge transfer. These absorptions are due to HOMO( $\alpha$ ) to LUMO+11( $\alpha$ ), HOMO( $\alpha$ ) to LUMO+1( $\alpha$ ), and HOMO( $\alpha$ ) to LUMO( $\alpha$ ) excitations, respectively.

Upon optimizing the structures, for 222(66-66,66-66)-opt layer all peaks shift to wavelengths below 400 nm. In the case of 222(56-66,66-66) layer, three major absorptions appear at about 440, 530, and 660 nm with major contribution from HOMO( $\alpha$ ) to LUMO+6( $\alpha$ ),

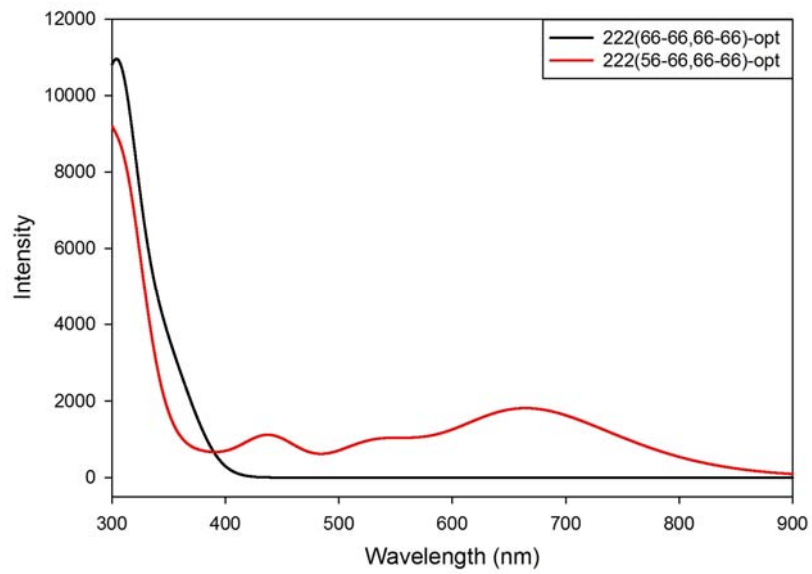
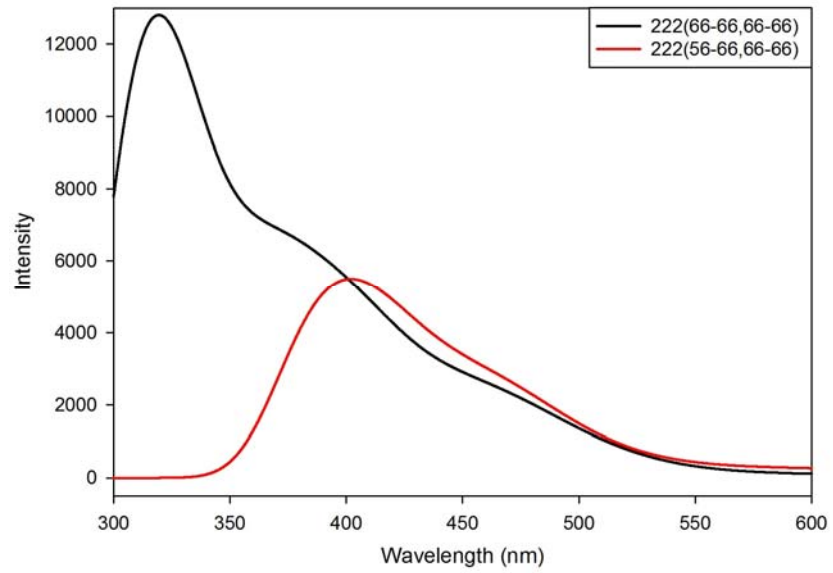


**Figure 2-19.** UV-Vis spectra for 222 layer.  
 (top) non-optimized, (bottom) optimized structures

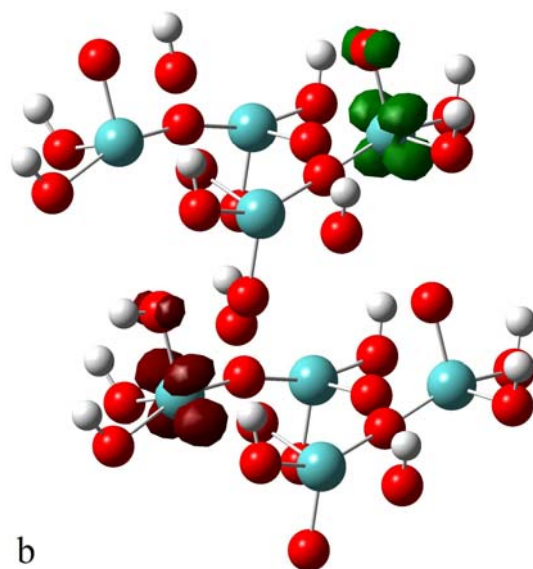
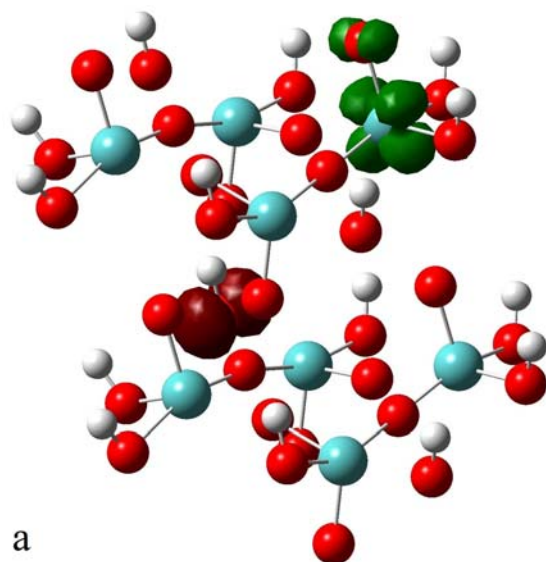


**Figure 2-20.** Examples of ligand to metal (LMCT) and intervalence (IVCT) charge transfers for 222 layer.

(a) LMCT for 222(66-66,6666), (b) IVCT for 222(56-66,66-66)

HOMO( $\alpha$ ) to LUMO+2( $\alpha$ ), and HOMO( $\alpha$ ) to LUMO( $\alpha$ ) excitations, respectively. These absorptions are due to intervalence charge transfer and peaks corresponding to ligand to metal charge transfer appear below 400 nm.

### 2.3 Summary

Valence and conduction bands of MoO<sub>3</sub> are composed of O-2p and Mo-4d orbitals respectively, and hence all absorptions in UV-Vis spectra predicted by time-dependent density functional theory calculations for molybdenum oxide clusters (chains, ribbons, and layer) containing Mo(VI) atoms are associated with ligand to metal charge transfer. As cluster size increases more energy states are available in valence and conduction bands and hence with smaller band gap, absorptions shift to higher wavelengths (Table 2-1). However, all absorptions are out of visible wavelengths range which is consistent with white color of the bulk molybdenum oxide.

Upon reducing of one or more Mo(VI) atoms in the structure to Mo(V) by means of hydrogen insertion, a new band (defect band, DB), is generated which is mainly composed of Mo(V)-4d orbitals and energetically lays between valence and conduction bands (Figure 2-4). The generation of defect band facilitates the intervalence charge transfer and corresponding absorption peaks appear at higher wavelengths comparing to peaks associated with ligand to metal charge transfer. Giving that these absorptions are in visible wavelengths, calculation results describe the color of bronzes. The ratio of the absorption intensities associated with intervalence charge transfer for the structures of the same size with different number of Mo(V) atoms, directly reflects the ratio of the number of Mo(V) atoms in the clusters.

## CHAPTER III

### DENSITY FUNCTIONAL STUDIES OF DIMETHYL PEROXIDE ADSORPTION AND DISSOCIATION ON $\text{MoO}_3(100)$ AND $\text{H}_{0.33}\text{MoO}_3(100)$ SURFACES

Molybdenum oxide and its bronzes with other metals and hydrogen are very valuable compounds in various industries. These compounds act as catalyst in many processes either directly or supported on other materials, but still there is no agreement between researchers about the catalytic activity and its mechanism. Most of the researches in this regard are experimental and there are a few theoretical studies.

In this chapter the adsorption and dissociation mechanism of dimethyl peroxide (DMP), on (100) surface of molybdenum oxide ( $\text{MoO}_3$ ), and its bronze with hydrogen ( $\text{H}_{0.33}\text{MoO}_3$ ), will be discussed theoretically by means of density functional theory calculations. An overview of the computational methodology can be found in the introduction. To model the  $\text{MoO}_3(100)$  surface, a cluster containing six molybdenum atoms constructed adopting the geometrical parameters from the Kihlberg [97]. Also, adopting the geometrical parameters from Adams et. al. [26] the hydrogen molybdenum bronze  $\text{H}_{0.33}\text{MoO}_3(100)$  surface is modeled as a cluster of six molybdenum atoms where two hydrogen atoms are attached to bridging oxygen atoms of molybdenum oxide cluster (Figure 3-1).

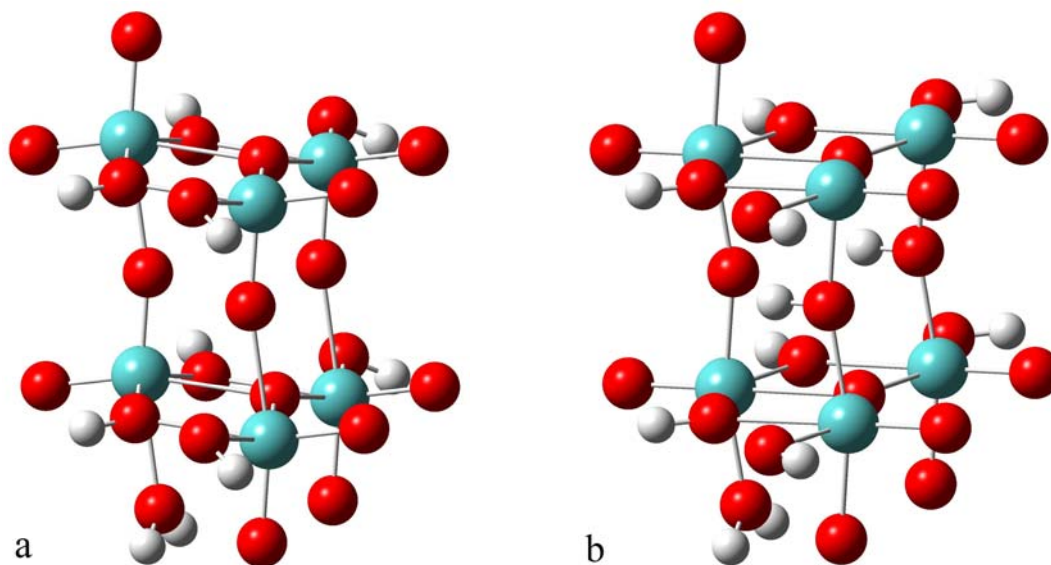


**Figure 3-1.** (a) Molybdenum oxide and (b) Hydrogen molybdenum bronze clusters

### 3.1 Computational Procedure

All calculations were done with Gaussian 09 software[89]. Molecular orbitals and electron density cube files were generated using standard cubegen and cubman utilities of Gaussian 09 software. To model the  $\text{MoO}_3$  and  $\text{H}_{0.33}\text{MoO}_3$  (100) surfaces, clusters containing six molybdenum atoms were used and all dangling bonds were terminated with hydrogen atoms producing the clusters with stoichiometry of  $\text{Mo}_6\text{O}_{23}\text{H}_{10}$  and  $\text{Mo}_6\text{O}_{23}\text{H}_{12}$  for molybdenum oxide and hydrogen molybdenum bronze, respectively. To model hydrogen molybdenum bronze cluster  $\text{H}_{0.33}\text{MoO}_3$ , two hydrogen atoms were attached to bridging oxygen atoms of molybdenum oxide cluster (Figure 3-1). Except with explicitly noted, calculations were performed using Becke three parameter hybrid functional[92] with Lee, Yang and Parr correlation[93], which includes both local and non-local terms (B3LYP). The 6-311++G(d,p) valence triple zeta basis set with two diffuse functions and the polarization d-and p- functions on non-hydrogen and hydrogen atoms respectively was employed for oxygen, and hydrogen atoms[98, 99]. Molybdenum atoms were

modeled with the LanL2DZ basis set, which includes the D95 double-zeta basis set, combined with the Los-Alamos effective core potentials[100, 101].

In all simulations, cluster atoms were kept fixed and dimethyl peroxide was allowed to relax on the (100) surface of the cluster. Energies of adsorbed model and isolated cluster and dimethyl peroxide were calculated and the difference considered as the adsorption energy. The energies were corrected for basis set superposition error (BSSE)[102] which was calculated for all structures using the standard counterpoise procedure built in the Gaussian 09 code. Vibrational frequency analysis was also performed for each structure to confirm that all stable structures have no imaginary modes and all transition states possess exactly one negative normal mode. To confirm that each computed transition state connects the correct initial and final structures, the Intrinsic Reaction Coordinate (IRC) method was utilized.

### **3.2 Results and Discussion**

The applicability of the chosen basis sets and functionals for this study have been discussed by Kadassov[19]. For further check, the geometry of dimethyl peroxide was optimized and compared to experimental values obtained by electron diffraction[103, 104], the difference between experimental and computed values for bond lengths and bond angles are 0.01Å and 0.6° respectively, which are acceptable for our purpose.

Frontier orbitals analysis was used to find possible adsorption sites for dimethyl peroxide on molybdenum oxide and hydrogen molybdenum bronze (100) surface. Figure 3-2 illustrates the highest occupied molecular orbital (HOMO), and the lowest unoccupied molecular orbital (LUMO), for dimethyl peroxide and (100) surface of clusters. The electron densities of HOMO and LUMO of dimethyl peroxide and clusters suggest that: for the molybdenum oxide cluster, dimethyl peroxide can be adsorbed in molecular form on the cluster (100) surface via making a

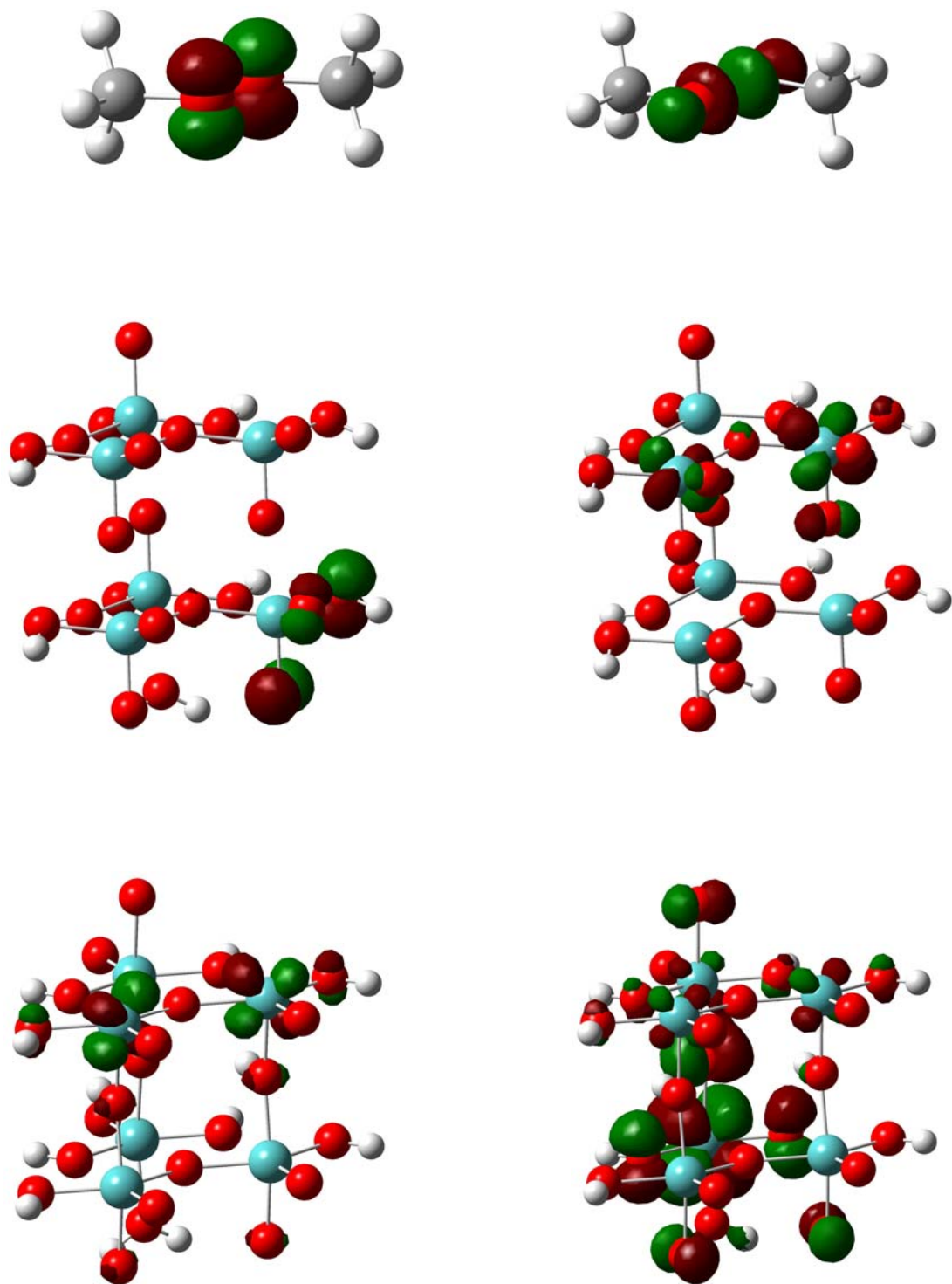


**Figure 3-2.** Frontier orbitals: (left) HOMO, (right) LUMO  
 (top) Dimethyl peroxide, (middle) MoO<sub>3</sub>, and (bottom) H<sub>0.33</sub>MoO<sub>3</sub>

dative bond between dimethyl peroxide O-2p and cluster Mo-4d orbitals. Since there is no significant electron density on the surface of cluster, we do not expect dissociative adsorption of dimethyl peroxide on the molybdenum oxide cluster.

In the case of hydrogen molybdenum bronze, molecular adsorption via dimethyl peroxide O-2p and cluster Mo-4d orbitals is possible. Also, HOMO of cluster shows significant electron density on the surface and hence dissociative adsorption of dimethyl peroxide is expectable.

### **3.2.1 Adsorption of Dimethyl Peroxide on the MoO<sub>3</sub> (100) Surface**

As mentioned above, dimethyl peroxide can be adsorbed in molecular form on the cluster surface making a dative bond between surface molybdenum and dimethyl peroxide oxygen atoms. Calculations started with putting a dimethyl peroxide molecule on top of the MoO<sub>3</sub>(100) surface, cluster's atoms were kept fixed and dimethyl peroxide molecule was relaxed on the surface. Relaxation of dimethyl peroxide on the cluster surface results in three stable structures, M1, M2, and M3 which are basically same structures with different spatial orientation of the dimethyl peroxide on the cluster surface (Figure 3-3). Also, vibrational frequencies were calculated to confirm that there is no imaginary vibration for these structures. The geometry parameters and adsorption energies for these structures along with those of dimethyl peroxide are summarized in Table 3-1. The adsorption energies for all three adsorbed forms are negative and approximately the same, so all three structures are favorable with a Mo-O bond length of about 2.5Å. As can be seen from the Table 3-1, all the parameters are almost the same except the CO<sub>1</sub>O<sub>2</sub>C dihedral angle due to the different orientations of dimethyl peroxide on the surface.

Density functional theory calculations performed to locate the transition state for the inter-conversion of M1, M2, and M3 structures. The transition states were confirmed by

**Table 3-1.** Structural parameters and adsorption energies of isolated and molecularly adsorbed dimethyl peroxide (DMP) forms and transition states for their conversion on MoO<sub>3</sub> cluster

	Mo-O <sub>1</sub> (Å)	O-O (Å)	C-O <sub>1</sub> (Å)	C-O <sub>2</sub> (Å)	CO <sub>1</sub> O <sub>2</sub> C (°)	E <sub>ads</sub> (kJmol <sup>-1</sup> )
DMP	NA	1.468	1.413	1.413	180.0	NA
M1	2.532	1.459	1.439	1.430	95.0	-40.3
M2	2.550	1.464	1.436	1.424	126.9	-39.7
M3	2.481	1.455	1.436	1.427	109.7	-40.0
M1M2	2.503	1.456	1.432	1.424	112.8	-30.7
M1M3	2.652	1.455	1.434	1.421	117.7	-22.9

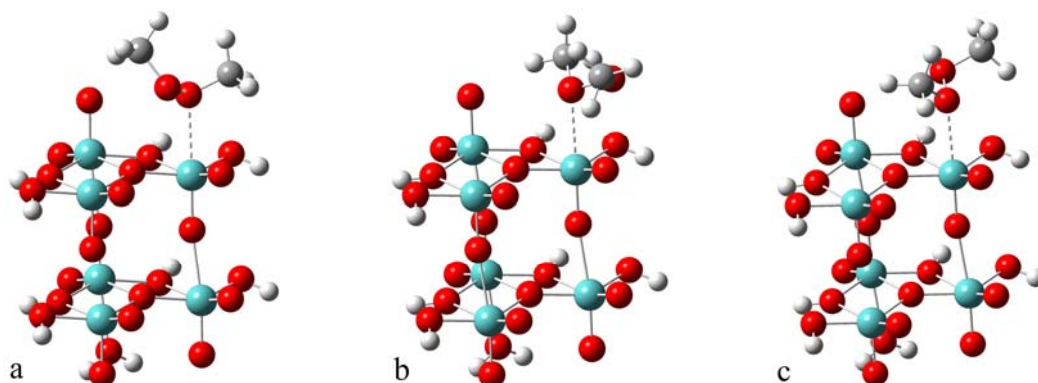


**Figure 3-3.** Molecularly adsorbed dimethyl peroxide (DMP) forms on MoO<sub>3</sub>(100) surface

(a) M1, (b) M2, and (c) M3

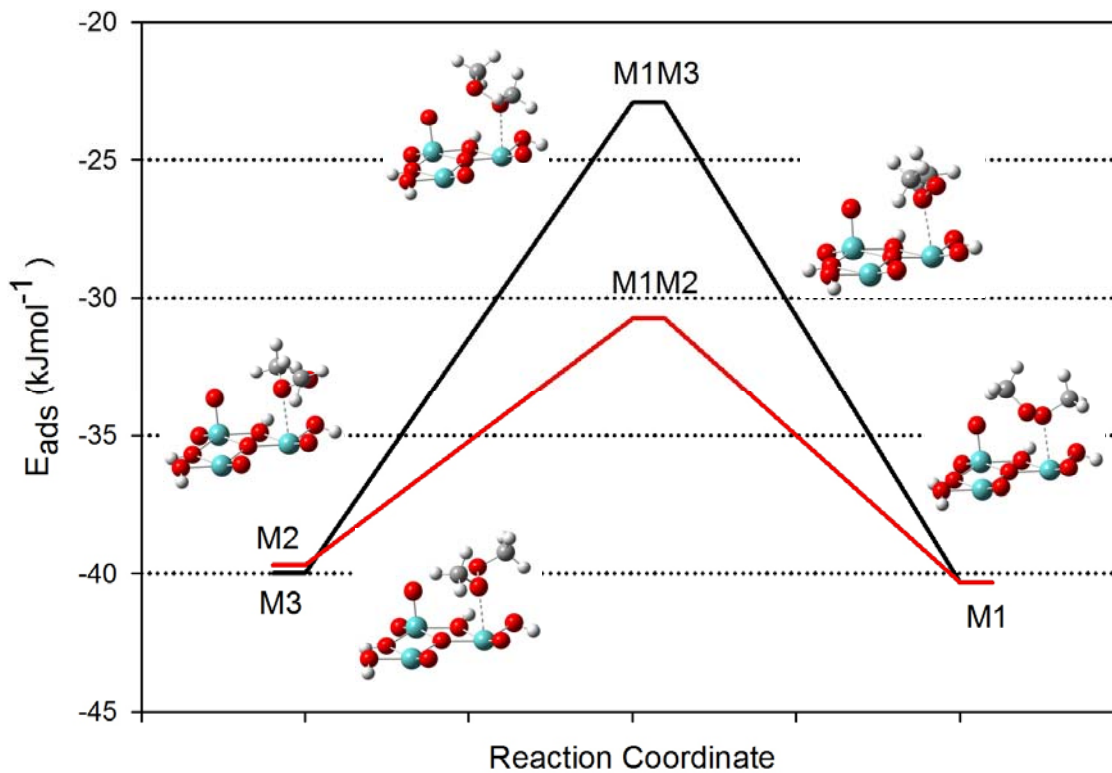


**Figure 3-4.** Reaction coordinate between molecularly adsorbed dimethyl peroxide (DMP) forms on MoO<sub>3</sub> (100) surface (only the surface atoms of cluster are shown)

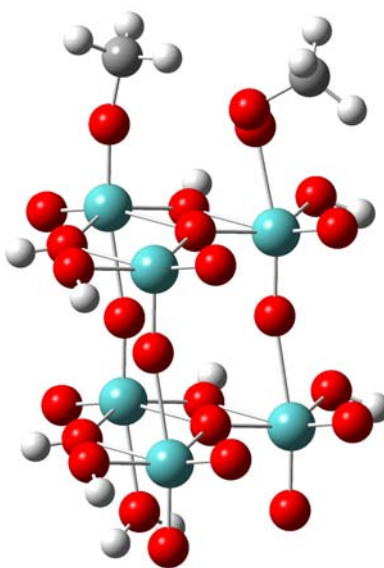


**Figure 3-5.** Stable structure from dimethyl peroxide C-O bond dissociation on MoO<sub>3</sub>(100) surface

vibrational frequency analysis. Each state contained only one imaginary frequency. In addition, Intrinsic Reaction Coordinate (IRC) calculations performed utilizing Gaussian 09 to confirm that the transition state connects desired initial and final structures.

Calculations show that M2 and M3 convert to M1 structure by clockwise and counter-clockwise rotation of dimethyl peroxide around Mo-O bond, respectively through transition states M1M2 and M1M3 (Figure 3-4). The energy barriers for M2 and M3 conversions to M1 are 9.0 kJmol<sup>-1</sup> and 17.1 kJmol<sup>-1</sup>, respectively. Due to spatial restrictions on counter-clockwise rotation of dimethyl peroxide on the surface, for the conversion of M3 to M1, Mo-O bond length must be elongated by 0.2 Å, and this explains the higher barrier for this conversion comparing to barrier for conversion of M2 to M1.

### **3.2.2 Dissociation of Dimethyl Peroxide on the MoO<sub>3</sub>(100) Surface**

Although HOMO and LUMO electron densities of MoO<sub>3</sub> and dimethyl peroxide do not suggest dissociative adsorption of dimethyl peroxide on molybdenum oxide cluster, possibilities of this type of adsorption were also considered. Dissociative adsorption can happen through either O-O or C-O bond cleavage. Among the various possibilities, computations show that the only stable case of dissociative adsorption happens through C-O bond cleavage, where CH<sub>3</sub> group attaches to cluster surface oxygen atom and OCH<sub>3</sub> group attaches to molybdenum atom (Figure 3-5). Geometry optimization calculation for this adsorption results in a stable structure with positive adsorption energy (168.8 kJmol<sup>-1</sup>) and hence the dissociation of dimethyl peroxide on MoO<sub>3</sub>(100) surface energetically is not possible.

### **3.2.3 Adsorption of Dimethyl Peroxide on the Bronze H<sub>0.33</sub>MoO<sub>3</sub> (100) Surface**

As mentioned above, similar to MoO<sub>3</sub> cluster, dimethyl peroxide can be adsorbed molecularly on the (100) surface of H<sub>0.33</sub>MoO<sub>3</sub> bronze through making a dative bond between

dimethyl peroxide O-2p and cluster Mo-4d orbitals resulting in three forms, BM1, BM2, and BM3 with different spatial orientations (Figure 3-6). The geometry parameters and adsorption energies for these structures along with those of dimethyl peroxide are summarized in Table 3-2. Adsorption energies for all three forms are negative, so these adsorptions are energetically favorable. These molecularly adsorbed forms have similar geometrical parameters except for CO<sub>1</sub>O<sub>2</sub>C dihedral angles due to different spatial orientations.

The most stable molecularly adsorbed dimethyl peroxide form is BM2 with adsorption energy of -104.2 kJmol<sup>-1</sup>. Attempts to find the pathways for the inter-conversion of these forms shows that counter-clockwise rotation of dimethyl peroxide about Mo-O bond, converts BM3 to BM1 through BM1M3 transition state with a barrier of 15.8 kJmol<sup>-1</sup>. Further counter-clockwise rotation about Mo-O bond converts BM1 to BM2 through BM1M2 transition state with a barrier of 14.5 kJmol<sup>-1</sup> (Figure 3-7). These conversions are simple rotations about Mo-O bond and hence have similar energy barriers

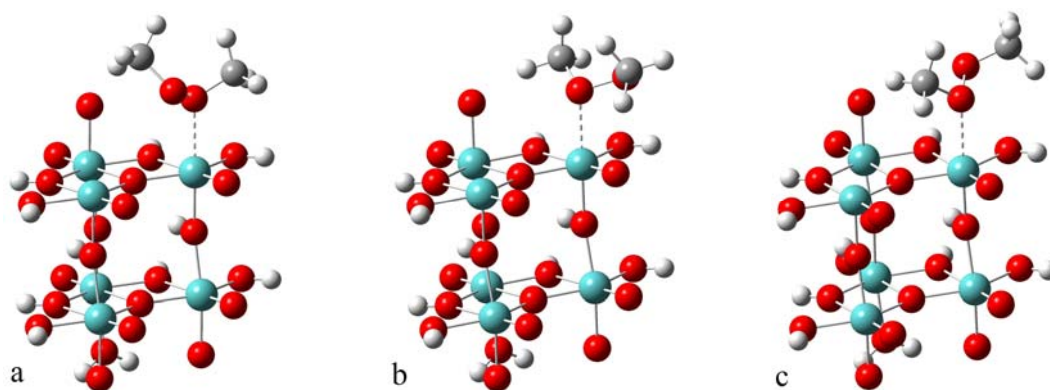


**Figure 3-6.** Molecularly adsorbed dimethyl peroxide (DMP) forms on H<sub>0.33</sub>MoO<sub>3</sub>(100) surface

(a) BM1, (b) BM2, and (c) BM3

**Table 3-2.** Structural parameters and adsorption energies of isolated and molecularly adsorbed dimethyl peroxide (DMP) forms and transition states for their conversion on  $H_{0.33}MoO_3$  bronze cluster

	Mo-O <sub>1</sub> (Å)	O-O (Å)	C-O <sub>1</sub> (Å)	C-O <sub>2</sub> (Å)	CO <sub>1</sub> O <sub>2</sub> C (°)	E <sub>ads</sub> (kJmol <sup>-1</sup> )
DMP	NA	1.468	1.413	1.413	180.0	NA
BM1	2.268	1.461	1.444	1.440	96.0	-92.7
BM2	2.270	1.472	1.451	1.427	123.2	-104.2
BM3	2.292	1.458	1.450	1.424	114.2	-81.0
BM1M2	2.263	1.448	1.441	1.430	105.0	-78.2
BM1M3	2.329	1.462	1.441	1.425	126.1	-65.2

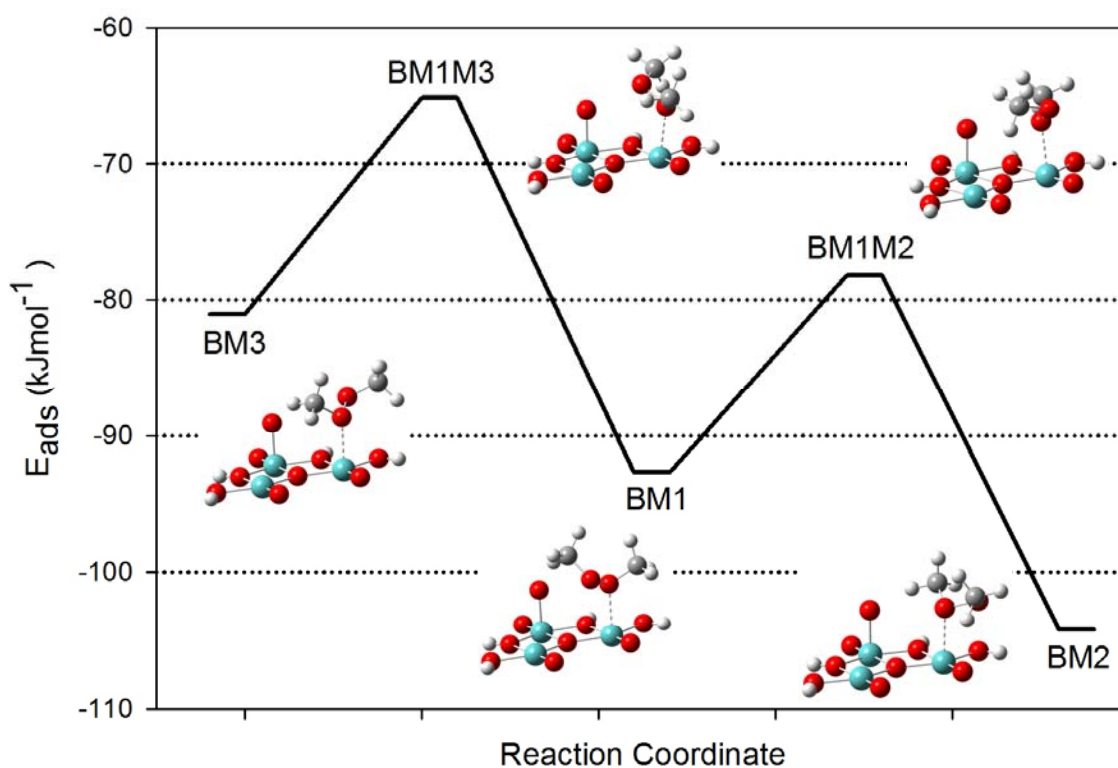


**Figure 3-7.** Reaction coordinate between molecularly adsorbed dimethyl peroxide (DMP) forms on  $H_{0.33}MoO_3$  (only the surface atoms are shown)

**Table 3-3.** Structural parameters and adsorption energies of molecularly adsorbed dimethyl peroxide (DMP) on MoO<sub>3</sub> and H<sub>0.33</sub>MoO<sub>3</sub> (Mo-O) surface molybdenum atom to dimethyl peroxide oxygen bond length, (O-H) surface oxygen to dimethyl peroxide hydrogen distance

	Mo-O (Å)	O-H (Å)	E <sub>ads</sub> (kJmol <sup>-1</sup> )
M1	2.532	2.237	-40.3
M2	2.550	2.216	-39.7
M3	2.481	2.425	-40.0
BM1	2.268	2.039	-92.7
BM2	2.270	1.921	-104.2
BM3	2.292	2.124	-81.0

Comparison of the adsorption energies of BM1, BM2, and BM3 to analogous forms for molybdenum oxide cluster, M1, M2, and M3, shows that, having lower adsorption energies, the adsorption of dimethyl peroxide is more favorable on bronze than molybdenum oxide. This is reflected on Mo-O bond length which is 0.2Å shorter for adsorptions on bronze. Two factors are important in adsorption energy when comparing molybdenum oxide and hydrogen molybdenum oxide bronze. As illustrated in Figure 3-2, LUMO of hydrogen molybdenum oxide bronze has electron density on surface oxygen atom which provides possibility of interaction between this oxygen atom and hydrogen atom from dimethyl peroxide molecule. Also, spatial orientation of Mo-4d orbitals facilitates head to head interactions with HOMO of dimethyl peroxide. Overall orbital interactions of dimethyl peroxide and hydrogen molybdenum oxide bronze are stronger and hence adsorption energies are lower. These effects are reflected as shorter Mo-O bond lengths and O-H (surface oxygen atom to dimethyl peroxide hydrogen atom) distance (Table 3-3).

### 3.2.4 Dissociation of Dimethyl Peroxide on the Bronze Surface Through O-O bond

#### Cleavage

The HOMO of bronze cluster shows that there is a significant electron density on the surface of the cluster. This suggests the possibility of formation of covalent bond, which results in

**Table 3-4.** Structural parameters and adsorption energies of molecularly adsorbed dimethyl peroxide (DMP) and forms produced by O-O bond cleavage and transition states for molecularly adsorbed form conversion to these structures on bronze cluster

	Mo-O (Å)	O-O (Å)	C-O <sub>1</sub> (Å)	C-O <sub>2</sub> (Å)	E <sub>ads</sub> (kJmol <sup>-1</sup> )
BM1	2.268	1.461	1.444	1.440	-92.7
BOO1	1.875	NA	1.406	1.405	-409.6
BOO2	1.940	1.428	1.405	1.428	-190.7
BM1OO1	2.017	1.974	1.413	1.368	-26.2
BM1OO2	2.176	1.792	1.416	1.429	-16.4

dissociative adsorption of dimethyl peroxide on the surface of bronze cluster. Two types of dissociative adsorptions are possible either by cleavage of O-O or C-O bond of dimethyl peroxide. For the O-O bond cleavage, OCH<sub>3</sub> groups can be attached to molybdenum atoms or surface oxygen atom. Considering these possibilities density functional theory calculations were performed and two stable structures (BOO1 and BOO2) were located. The HOMO of bronze cluster (Figure 3-2), shows that the electron density is mainly located on surface molybdenum atom, hence as expected, BOO1 where two OCH<sub>3</sub> groups are attached to molybdenum atoms is more stable than BOO2 structure where OCH<sub>3</sub> groups are attached to surface molybdenum and oxygen atom. Structural parameters and adsorption energies of these structures are summarized in Table 3- 3.

Starting from molecularly adsorbed forms, a series of computations were performed to locate transition state structures for the dissociation of molecularly adsorbed forms to BOO1 and BOO2 structures. Computations shows that only BM1 can dissociate to BOO1 and BOO2 through transition states BM1OO1 and BM1OO2, respectively (Figure 3-8). The geometry parameters and adsorption energies for these transition states along with those of BM1 are summarized in Table 3-4. Both dissociations are associated with O-O bond cleavage with energy barriers of 66.5 and 76.3 kJmol<sup>-1</sup> respectively. The intrinsic reaction coordinate calculations show

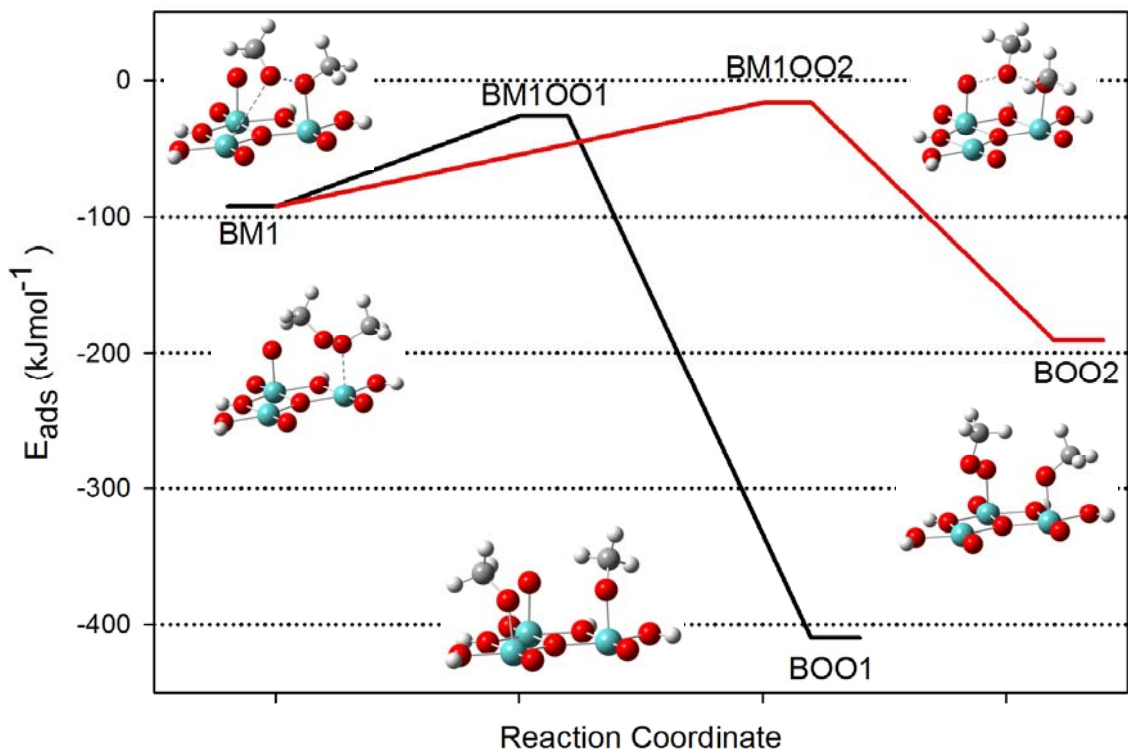


**Figure 3-8.** Reaction coordinate between molecularly adsorbed dimethyl peroxide ( DMP) and structures produced by O-O bond cleavage on bronze cluster (only the surface atoms are shown)

that the conversion of BM1 to BOO1 starts with O-O bond elongation by 0.5 Å toward the other molybdenum atom, followed by migration of OCH<sub>3</sub> group to molybdenum atom and rotation of CH<sub>3</sub> group on other molybdenum atom to produce the final BOO1 structure. The conversion of BM1 to BOO2 starts with clockwise rotation of dimethyl peroxide around Mo-O bond, followed by elongation of O-O bond by 0.3 Å toward surface oxygen atom. Then, methoxy group migrates to surface oxygen atom and the methyl group on the methoxy group attached to the molybdenum atom rotates counter-clockwise to produce final BOO2 structure.

As can be seen from Figure 3-8, BOO1 is more stable than BOO2, so possible pathways were considered for the BOO2 to BOO1 conversion. For this conversion to occur, one methoxy

group must migrate to surface oxygen atom and the methyl group on the other methoxy group must rotate to produce the final structure. Attempts to locate the transition state for this conversion show that this conversion is a two-step process through a stable intermediate (BOO3) (Figure 3-9). BOO3 is the result of the methyl group rotation about Mo-O bond in BOO2 structure. This conversion occurs by a simple rotation and as expected its energy barrier is as low as 0.8 kJmol<sup>-1</sup>. The second step of BOO2 to BOO1 conversion is the migration of the methoxy group from surface oxygen to molybdenum atom, which occurs through conversion of BOO3 to BOO1. This migration is associated with O-O bond cleavage and the energy barrier for this migration (63.6 kJmol<sup>-1</sup>) is in the same order of energy barriers for the conversion of BM1 to BOO1 and BOO2. The structural parameters and adsorption energies for all structures involved in BOO2 to BOO1 conversion are summarized in Table 3-5. It can be seen from this table that, O-O bond length is elongated by 0.4 Å for BOO3 to BOO1 conversion to be occur.

**Table 3-5.** Structural parameters and energies of stable structures and transition states for the BOO2 to BOO1 conversion

	Mo-O (Å)	O-O (Å)	C-O <sub>1</sub> (Å)	C-O <sub>2</sub> (Å)	E <sub>ads</sub> (kJmol <sup>-1</sup> )
BOO1	1.875	NA	1.406	1.405	-409.6
BOO2	1.940	1.428	1.405	1.428	-190.7
BOO3	1.916	1.431	1.398	1.424	-194.6
BOO3OO1	1.888	1.870	1.401	1.400	-131.0
BOO2OO3	1.932	1.431	1.402	1.427	-189.9

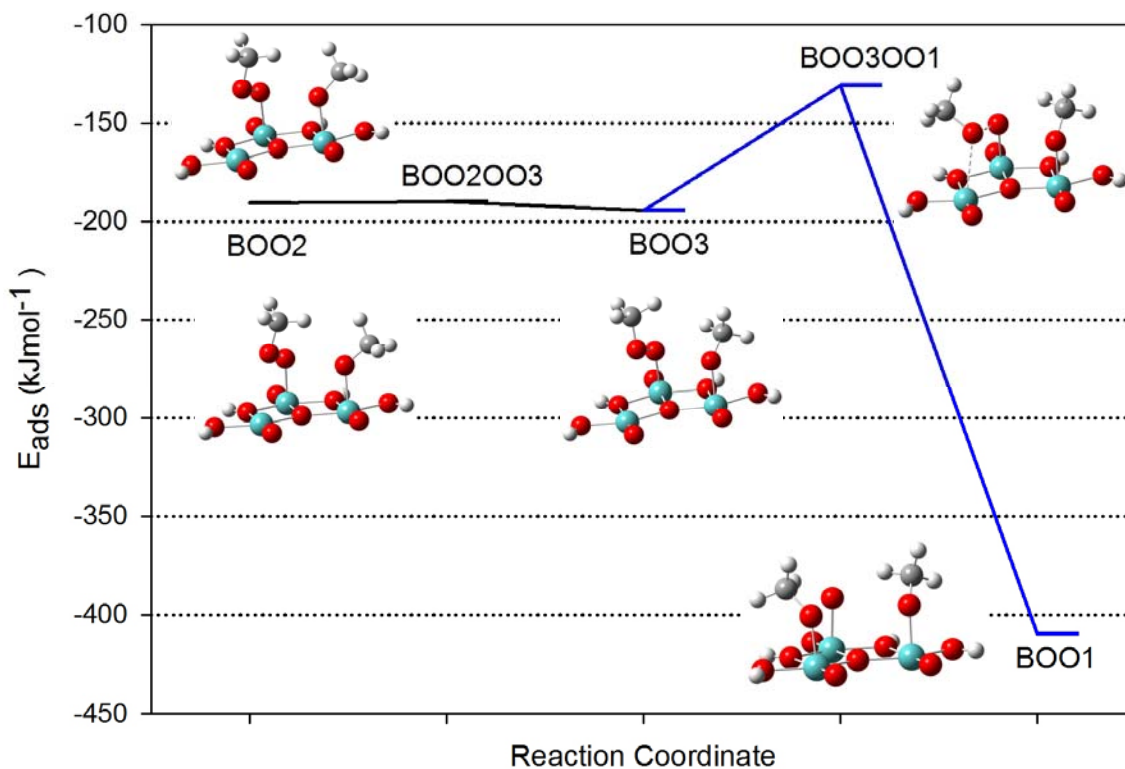


**Figure 3-9.** Pathway for conversion of BOO2 to BOO1 on bronze surface

### 3.2.5 Dissociation of Dimethyl Peroxide on the Bronze Surface Through C-O Bond

#### Cleavage

Similar to dissociation of dimethyl peroxide on the surface of bronze cluster through O-O bond cleavage, it can dissociate through C-O bond cleavage. Considering all the possibilities, several stable structures were located by calculations. The methyl group from C-O bond cleavage can attach either to molybdenum atom, BCO1 and BCO2, or to surface oxygen atom, BCO3 and BCO4 (see Figure 3-10).

To find the pathways for the C-O bond dissociation on the bronze surface, starting from the molecularly adsorbed structures (BM1, BM2, and BM3), all the possibilities considered to locate the transition states. Calculations show that C-O bond cleavage in BM3 results in BCO1

**Table 3-6.** Structural parameters and adsorption energies of molecularly adsorbed dimethyl peroxide (DMP) and forms produced by C-O bond cleavage and transition states for molecularly adsorbed form conversion to these structures on bronze cluster

	Mo-O <sub>1</sub> (Å)	Mo-C (Å)	O-O (Å)	C-O <sub>1</sub> (Å)	C-O <sub>2</sub> (Å)	E <sub>ads</sub> (kJmol <sup>-1</sup> )
BM2	2.270	NA	1.472	1.427	1.451	-104.2
BM3	2.292	NA	1.458	1.450	1.424	-81.0
BCO1	1.944	2.154	1.390	1.433	NA	-51.3
BCO2	1.948	2.152	1.411	1.430	NA	-38.0
BCO3	1.977	NA	1.450	1.422	1.409	-187.9
BCO4	1.984	NA	1.429	1.421	1.399	-187.2
BM3CO1	2.053	3.281	1.412	1.425	2.428	148.3
BM2CO2	2.036	2.975	1.412	1.427	2.308	156.1
BM2CO3	2.102	NA	1.442	1.428	2.231	88.9
BM2CO4	2.215	NA	1.440	1.422	1.918	69.1

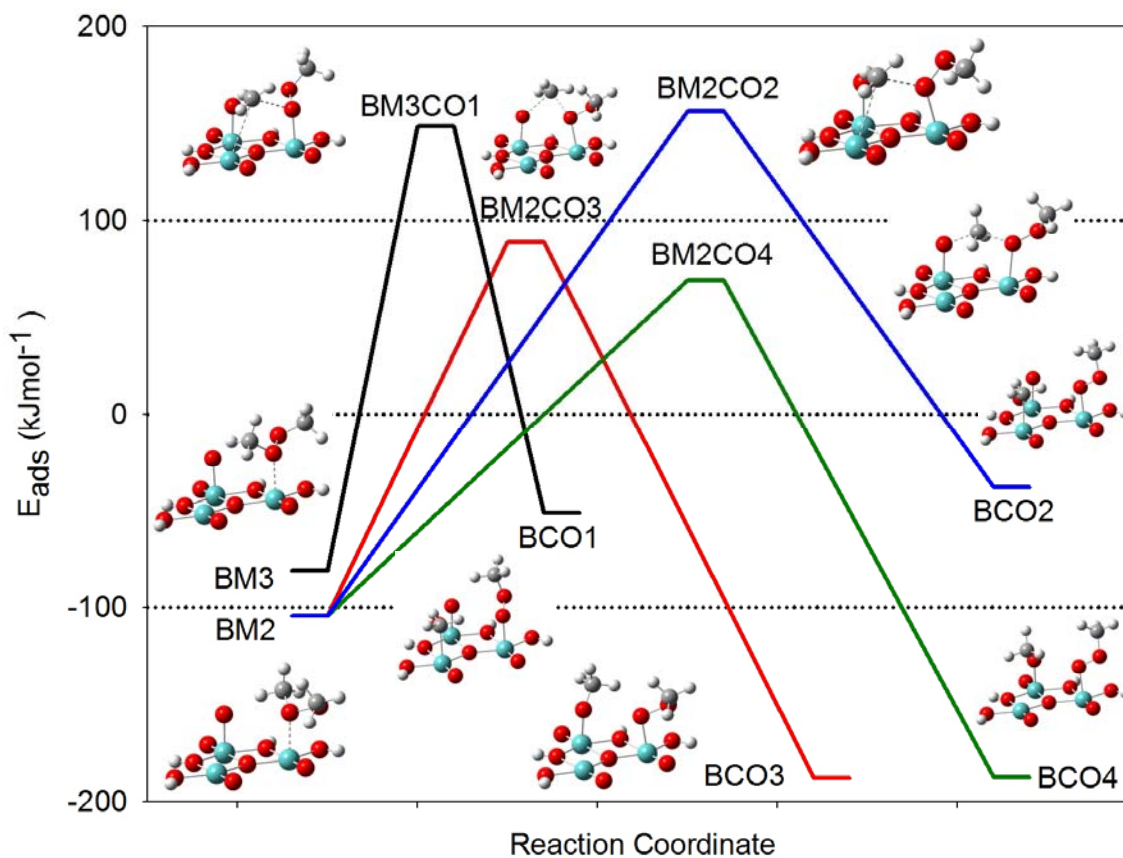


**Figure 3-10.** Reaction coordinate between molecularly adsorbed dimethyl peroxide (DMP) and structures formed by C-O bond cleavage on bronze cluster (only the surface atoms are shown)

structure. BCO<sub>2</sub>, BCO<sub>3</sub>, and BCO<sub>4</sub> are the results of C-O bond cleavage in BM<sub>2</sub> ( see Figure 3-10). Structural parameters and adsorption energies for all stable and transition state structures are summarized in Table 3-6. Figure 3-10 and Table 3-6 show that, although products of C-O bond cleavage have negative adsorption energies and are stable, the adsorption energies for the conversion of molecularly adsorbed forms to these structures are all positive. As a results, transition state structures are not formed, and molecularly adsorbed species are expected to desorbed from the surface.

### 3.3 Summary

Dimethyl peroxide is adsorbed molecularly on (100) surface of MoO<sub>3</sub> and H<sub>0.33</sub>MoO<sub>3</sub> bronze clusters, making a dative bond between O-2p and Mo-4d orbitals. Three molecularly adsorbed forms were identified for both oxide and bronze clusters which can convert to each other by simple rotations about Mo-O bond.

Dimethyl peroxide dissociation on the cluster surface occurs either by O-O or C-O bond cleavage. While the O-O bond cleavage on the oxide cluster does not result in a stable structure, one stable structure is produced from C-O bond cleavage where CH<sub>3</sub> and OOCCH<sub>3</sub> groups are attached to surface oxygen and molybdenum atoms respectively. However, the adsorption energy for this structure is positive and hence energetically is not possible.

Unlike the oxide cluster, hydrogen molybdenum oxide bronze has a significant electron density on (100) surface from HOMO, which provides the possibility of dissociation of dimethyl peroxide on the cluster surface. For the O-O bond cleavage, two main products were identified where one OCH<sub>3</sub> group is attached to molybdenum atom and the other one is either attached to surface oxygen (BOO<sub>2</sub>), or molybdenum atom (BOO<sub>1</sub>). BOO<sub>1</sub> is more stable than BOO<sub>2</sub> and calculations show that BOO<sub>2</sub> can convert to BOO<sub>1</sub> through stable intermediate structure (BOO<sub>3</sub>).

For the C-O bond cleavage case, four stable structures were located: BCO1, BCO2, BCO3, and BCO4. The most stable structures are BCO3 and BCO4 where CH<sub>3</sub> and OOCCH<sub>3</sub> groups are attached to surface oxygen and molybdenum atoms respectively. Also there are two other stable structures, BCO1 and BCO2, where both CH<sub>3</sub> and OOCCH<sub>3</sub> groups are attached to molybdenum atoms. The adsorption energies of transition state structures for all possible conversion of molecularly adsorbed forms to these stable structures are positive and hence dimethyl peroxide is desorbed from the cluster surface upon C-O bond dissociation. As a result, the only possible pathway for dissociation of dimethyl peroxide, is through O-O bond cleavage on the hydrogen molybdenum bronze cluster surface.

## CHAPTER IV

### EXPERIMENTAL AND THEORETICAL STUDIES OF MOLYBDENUM-GLUCONIC ACID COMPLEXES

Catalytic activity of molybdenum oxide in many industrial and pharmaceutical processes involving organic molecules is due to complexation of these organic ligands with molybdenum. The complexation of organic ligands with molybdenum has been subject of many experimental studies but there are not much theoretical studies to provide insight on the bonding and reaction mechanisms.

In this chapter, complexation of molybdenum with D-Gluconic acid (GL), and the existing equilibrium between molybdenum gluconate complexes with different metal to ligand ratios studied experimentally by means of UV-Vis spectroscopy is explained. Furthermore, theoretical calculations performed to support the experimental data will be discussed. More detailed information about computational method used in this study can be found in Chapter 1.

## 4.1 Experimental Procedure

UV-Vis spectra obtained with Varian Cary 5000 instrument. To take the spectra, molybdenum gluconate dimer complex solution diluted 100 times and 1.0 cm path length cuvette was used. To find the absorption peaks associated with the complex color, the UV-Vis spectrum was measured from 200 to 1200 nm. For the kinetics work, UV-Vis spectra were taken from 400-1100 nm wavelength range over a temperature range from 20 to 80 °C. As discussed below, this data was used to calculate the activation energy  $E_a$ , and Gibbs free energy  $\Delta G$ , for the equilibrium.

## 4.2 Computational Procedure

All calculations were done with Gaussian 09 software[89]. Molecular orbitals and electron density cube files were generated using standard cubegen and cubman utilities of Gaussian 09 software. Each excitation considered as a Gaussian function, excitations convoluted and UV-Vis spectra were visualized utilizing GaussSum software[91]. Except with explicitly noted, calculations were performed using Becke three parameter hybrid functional[92] with Lee, Yang and Parr correlation[93], which includes both local and non-local terms (B3LYP). The 6-311++G(d,p) valence triple zeta basis set with two diffuse functions and the polarization d- and p-functions on non-hydrogen and hydrogen atoms respectively was employed for all oxygen, carbon, and hydrogen atoms[98, 99]. The molybdenum atoms were modeled with the LanL2DZ basis set, which includes the D95 double-zeta basis set, combined with the Los-Alamos effective core potentials[100, 101]. In some cases other density functional theory functionals and basis sets were also employed.

The structure of all species optimized in gas phase and in addition, vibrational frequency analysis was performed for each configuration to confirm that all stable structures have no imaginary modes. Also, the data from vibrational analysis calculation was used to calculate the

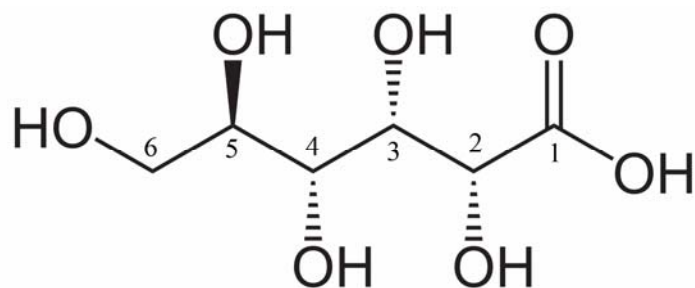


**Figure 4-1.** D-gluconic acid structure.

$\Delta G$  of equilibrium. Optimization and vibrational frequency analysis calculations were also done in aqueous solution. For the calculations in solution, Self-Consistent Reaction Field (SCRF) methods, which model the solvent as a continuum of uniform dielectric constant (reaction field), were used. Onsager (Dipole)[105], Polarizable Continuum (PCM)[106], Conductor Polarizable Continuum (CPCM)[68], and Universal Solvation (SMD) models by choosing proper parameters were also used for comparison.

The Dipole model places the solute in a spherical cavity within the solvent reaction field. To use this model, the volume of the solute was calculated using "Volume" keyword of Gaussian 09 in gas phase. PCM and CPCM models create the solute cavity via a set of overlapping spheres. Also as recommended by Marenich and coworkers, for  $\Delta G$  calculations Universal Solvation Model (SMD)[69] was used which is based on solute electron density on a continuum model of the solvent defined by the bulk dielectric constant and atomic surface tensions.

### 4.3 Results and Discussion

Ramos and coworkers[45] found that depending on the pH, concentration, and metal to ligand molar ratio, gluconic acid forms 8 complexes with molybdenum(VI). At any pH with 1:2 metal to ligand ratio, gluconic acid molecules attach to molybdenum by oxygen atoms of OH





I

To study the thermodynamic properties and kinetics of this equilibrium, UV-Vis spectroscopy is used in this research.

#### 4.3.1 Experimental

Blue dimer complex was provided by Apblett's group. The stock solution was diluted 100 times and the UV-Vis spectrum was taken (see Figure 4-3). There are four major absorption features in visible region at approximately 400, 580, 660, and 800 nm. The strong absorptions above 500 nm describe the blue color of the solution and the absorption below 500 nm corresponds to yellow color of the complex.

Figure 4-4 shows that results of the UV-Vis spectrum was a function of time for the dimer solution at 40 °C. As can be seen, the intensity of absorptions above 500 nm decreases by time and after 20 min, there is just one strong absorption below 400 nm which describes the final yellow color of the solution.

To calculate the  $E_a$  and  $\Delta G$  for proposed equilibrium I, kinetic measurements performed at 20, 40, 60, and 80 °C and absorptions were measured at 830 nm (Figure 4-5). Experimental data (blue line) looks like exponential decay, so they fitted to  $y = y_0 + a(1 - e^{-bx})$  equation at each temperature. This equation used to calculate initial changes in absorption (black line) and the data from this part of graphs is used to calculate the activation energy for the equilibrium I.

For the activation energy ( $E_a$ ) Calculation, the initial absorptions were plotted against time. The slope of each plot is the forward reaction rate constants  $k$ , at corresponding temperature.

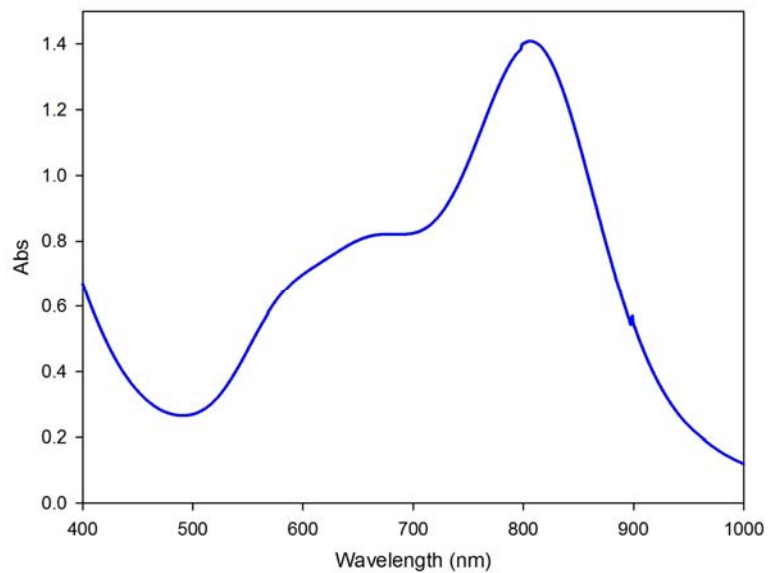


**Figure 4-3.** UV-Vis spectrum of blue dimer complex.

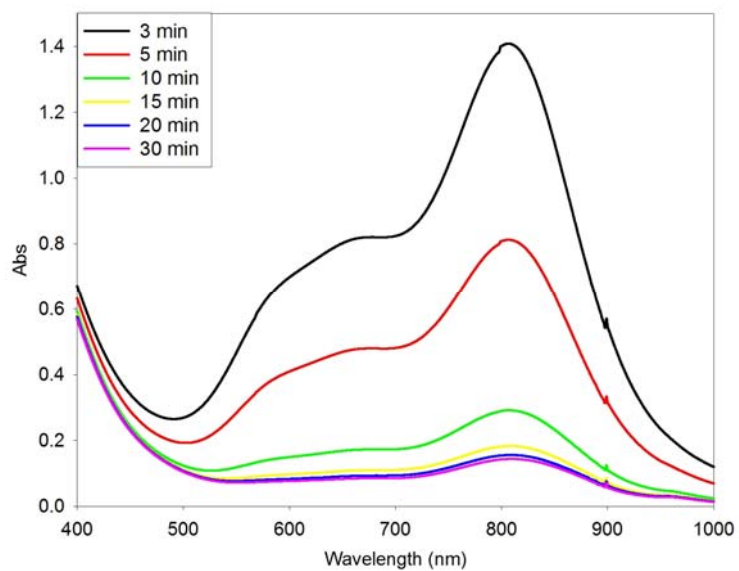


**Figure 4-4.** UV-Vis spectrum of 2:1 blue complex as function of time after heated from room temperature to 40 °C.

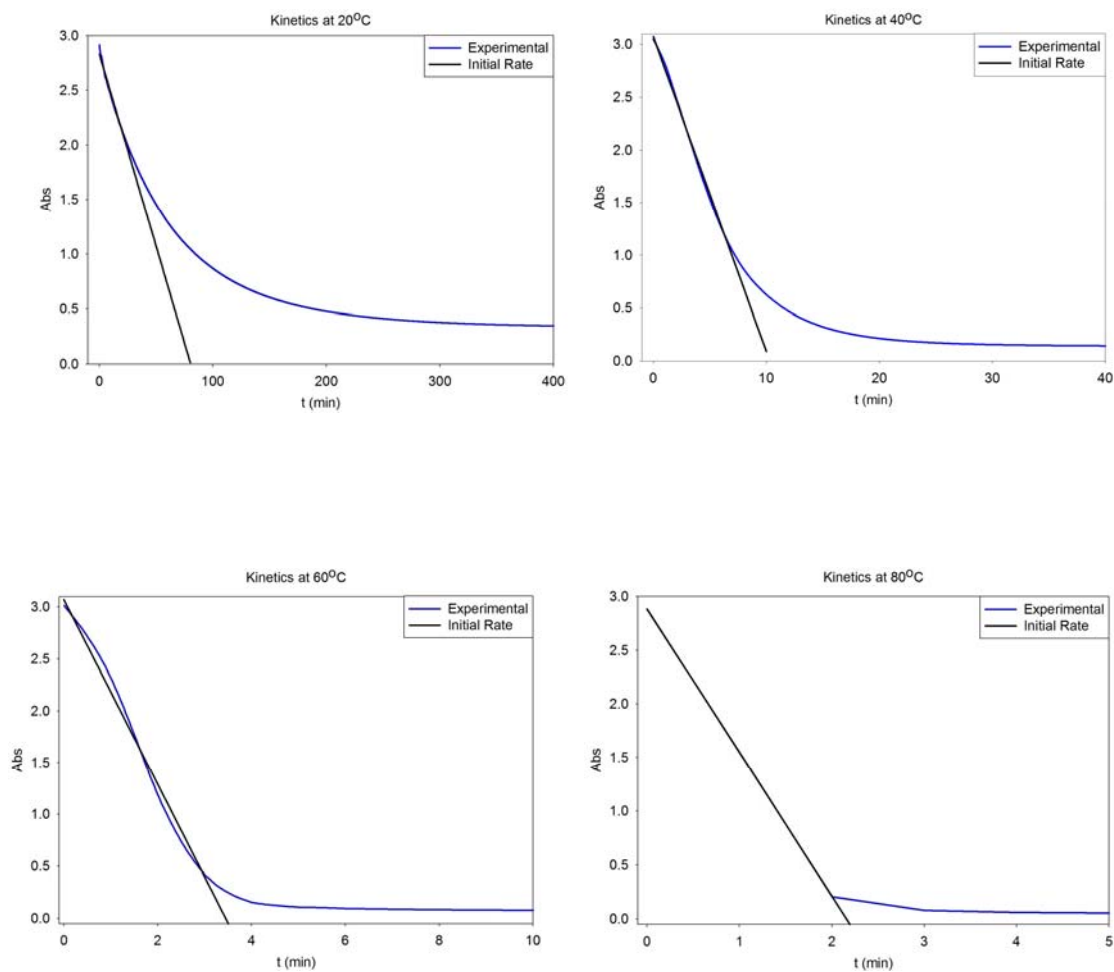


**Figure 4-5.** Kinetics measurements at 20, 40, 60, and 80 °C for diluted blue dimer.

Absorptions measured at 830 nm

Arrhenius equation describes the dependence of rate constants on temperature,

$$k = Ae^{-E_a/RT} \quad (4-1)$$

**Table 4-1.** Experimental data used to calculate activation energy ( $E_a$ ) for the dissociation of the dimer (Reaction I)

T(K)	1/T(K <sup>-1</sup> )	Experimental Data	
		k	lnk
293.15	0.003411	0.0352	-3.3467
313.15	0.003193	0.2984	-1.2093
333.15	0.003002	0.8907	-0.1158
353.15	0.002832	1.3376	0.2909

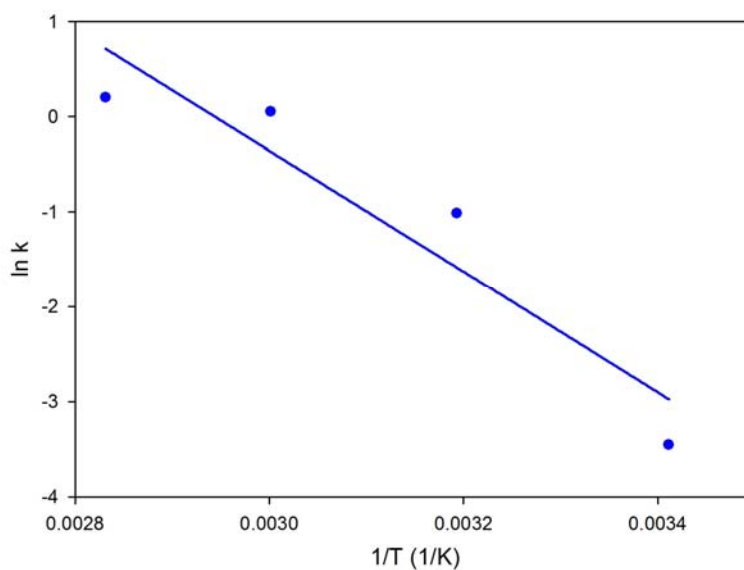


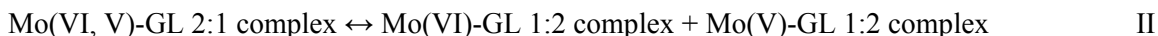
**Figure 4-6.** Arrhenius plot to calculate the activation energy ( $E_a$ ) for the dissociation of the dimer (Reaction I)

, where  $k$  is rate constant,  $A$  is a constant,  $E_a$  is activation energy,  $R$  is gas constant, and  $T$  is temperature. Using the slope of the  $\ln k$  vs  $1/T$  plot, activation energy is calculated. Table 4-1 and Figure 4-5 show the data and plot used to calculate the activation energy,  $E_a$ . The calculated activation energy is  $53 \pm 14 \text{ kJmol}^{-1}$  based on experimental data which is consistent with Bussan result ( $57 \text{ kJmol}^{-1}$ )[107].

For  $\Delta G$  calculation, equation 4-2 is used which relates the equilibrium constant to  $\Delta G$ :

$$K = \exp\left(-\frac{\Delta G}{RT}\right) \quad (4-2)$$

, where  $K$  is equilibrium constant,  $\Delta G$  is Gibbs free energy,  $R$  is gas constant, and  $T$  is temperature. Based on this equation, using the slope of  $\ln K$  vs  $1/T$  plot the  $\Delta G$  can be calculated. To calculate the equilibrium constants at various temperatures, two assumption are made: we assumed that the following equilibrium (Reaction II) is valid and the initial amount of 1:2 monomer complexes are negligible:



Based on Beer-Lambert law,  $A = \varepsilon lc$ , absorbance is directly proportional to concentration and since path length,  $l$ , and molar absorptivity,  $\varepsilon$ , are the same, absorbances can be used instead of concentrations to calculate the equilibrium constant. Using the equilibrium II and assumptions made, the equation for equilibrium constant calculation can be written as bellow:

$$K = \frac{[\text{Mo(VI)-GL 1:2 complex}] \times [\text{Mo(V)-GL 1:2 complex}]}{[\text{Mo(VI, V)-GL 2:1 complex}]} \propto \frac{(A_0 - A)^2}{A} \quad (4-3)$$

, where  $A_0$  is the initial absorbance and  $A$  in the absorbance at equilibrium.

Table 4-2 summarizes the data used to calculate the Gibbs free energy. Using the slope of the  $\ln K$  vs  $1/T$  plot (Figure 4-7), the calculated Gibbs free energy is  $42 \pm 5 \text{ kJmol}^{-1}$  which is also in good agreement with Bussan result ( $48.8 \text{ kJmol}^{-1}$ )[107].

**Table 4-2.** Data used to calculate Gibbs free energy( $\Delta G$ ) for the dissociation of the dimer (Reaction II)

T (K)	293.15	313.15	333.15	353.15
$A_0$	2.802	3.288	3.213	2.956
A	0.354	0.135	0.052	0.027
$A_0-A$	2.448	3.153	3.161	2.929
K	16.912	73.823	191.735	317.829
$\ln K$	2.828	4.302	5.256	5.762

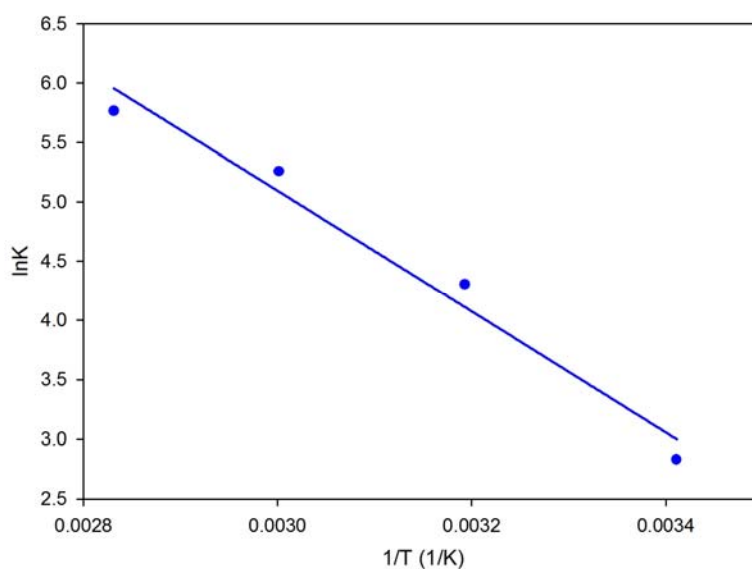


**Figure 4-7.**  $\ln K$  vs  $1/T$  plot to calculate the Gibbs free energy( $\Delta G$ ) for proposed dissociation of the dimer (Reaction II)

### 4.3.2 Computation Analysis

To support the experimental data and confirm the validity of the equilibrium II, UV-Vis spectra of monomer and dimer molybdenum gluconate complexes were simulated by time-dependent density functional theory calculations both in gas and solution phases. In addition,  $\Delta G$  was calculated for the equilibrium utilizing frequency calculations in gas and solution phases. The structure of Mo(VI, V)-GL, Mo(V, V)-GL, Mo(VI)-GL, and Mo(V)-GL complexes were optimized in gas phase utilizing B3LYP method using LANL2DZ basis set and effective core potential (ECP) for molybdenum atoms and 6-311++G(d,p) basis set for oxygen, carbon, and hydrogen atoms. To be sure that these optimized structures are not transition structures, vibrational frequency calculation were also done for optimized structures. The data from vibrational frequency analysis were also used to calculate  $\Delta G$ . The optimized structures were used to simulate UV-Vis spectra of the complexes utilizing time-dependent density functional theory calculations and GuassSum software with a FWHM of 3000 nm to simulate the broadening of the spectra due to the finite resolution of the instrumentation, and vibrational and rotational broadening.

There is no experimental data available for geometry parameters of these complexes, hence to validate our methodology we first used this calculation method to optimized the structure of similar complexes with known geometrical parameters. For this purpose, the complexes of Mo(VI) with 2-methoxyethanol (Mo-met), and erythritol (Mo-eryt) which their structures are similar to Mo-GL monomer and dimer complexes are used (Figure 4-8).

The structure of these complexes optimized in both gas phase and aqueous solution and vibrational frequencies also calculated to confirm that the stable structures are not transition structure. The calculated bond lengths and angles were compared to crystallographic data[108, 109]. The average difference between the computed and experimental bond lengths and angles for

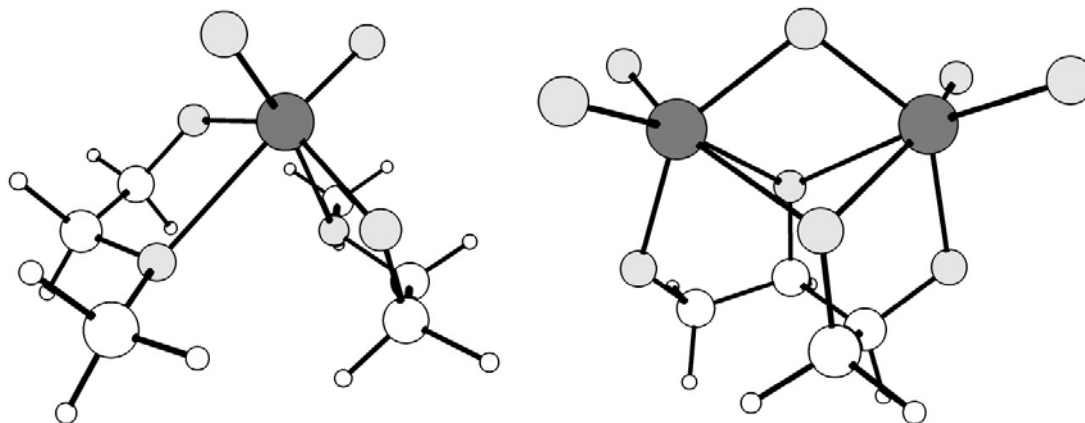


**Figure 4-8.** (left) 2-methoxyethanol, (right) erythritol complexes with Mo(VI)

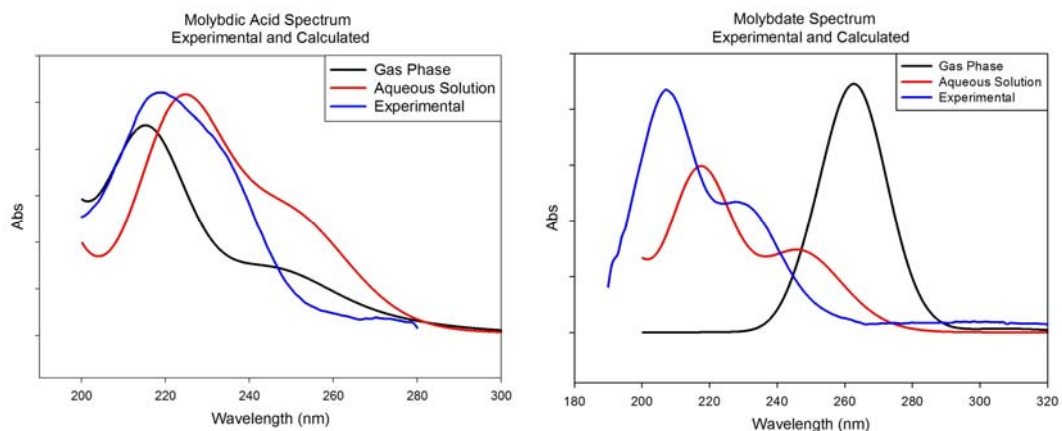


**Figure 4-9.** Computed and experimental spectrums of molybdic acid (left) and molybdate (right)

Mo-met complex are  $0.07 \text{ \AA}$  and  $2.93^\circ$  and  $0.04 \text{ \AA}$  and  $1.71^\circ$  for gas phase and aqueous phase, respectively. These errors for Mo-eryt complex are  $0.15 \text{ \AA}$  and  $1.60^\circ$  for gas phase and  $0.05 \text{ \AA}$  and  $1.60^\circ$  for aqueous solution. This indicates that chosen functional and basis set are appropriate for our calculations.

Furthermore, UV-Vis spectra were simulated utilizing time-dependent density functional theory calculations using same functionals and basis set for molybdic acid and molybdate ion and compared to experimental spectra. Figure 4-9, shows the computed (gas phase and aqueous solution) and experimental spectra for molybdic acid and molybdate ion. The experimental spectrum for molybdic acid shows two absorption features at approximately 220 and 240 nm, and molybdate spectrum has two main absorption features at about 210 and 240 nm. While the simulated spectrum in gas phase for molybdic acid has two absorption features which slightly shifted comparing to experimental spectrum (215 and 250 nm), the gas phase simulated spectrum for molybdate ion shows only one absorption feature at approximately 265 nm.

In gas phase, ions and molecules are considered isolated and intermolecular forces are neglected and for this reason absorptions are shifted. However, in case of molybdate ion, strong electrostatic forces are neglected in gas phase and hence larger shifts in absorption wavelengths are observed. To take these forces into account, geometry minimization and time-dependent density functional theory calculations for molybdic acid and molybdate performed in aqueous solution utilizing default solvation model of Gaussian 09 software (PCM). The simulated spectra in aqueous solution for both molybdic acid and molybdate have same absorption features as experimental spectra, except that absorptions are shifted slightly to higher wavelengths. These results confirms that the chosen functional and basis set are appropriate for simulation of UV-Vis spectrum utilizing time-dependent density functional theory computations for both neutral and charged systems in aqueous solution, and neutral molecules in gas phase; charged systems in gas phase must be dealt with more caution.

The valence of molybdenum atom in complex can be either V or VI, hence for the dimer complex possibilities are Mo(VI, VI), Mo(VI, V), or Mo(V, V). To confirm that the dimer is a multi-valence complex, the geometry of all possibilities were optimized utilizing B3LYP

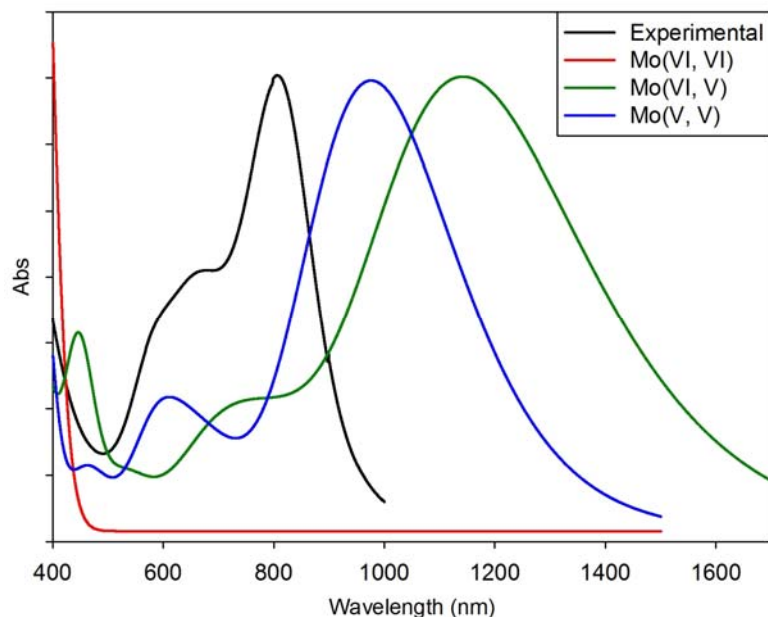


**Figure 4-10.** Experimental and simulated spectra for all possible dimer complexes

functional and optimized geometries were used to run time-dependent density functional theory calculations. Figure 4-10 compares the experimental and simulated spectra for these complexes in gas phase. The spectrum of dimer complex Mo(VI, VI), as expected has one absorption under 500 nm which gives yellow color to complex. The overall absorption features of Mo(VI, V) and Mo(V, V) spectra are similar to experimental spectrum, hence these complexes are acceptable candidates to be the actual dimer complex.

UV-Vis spectra were simulated utilizing time-dependent density functional theory calculations in gas phase and due to neglecting the intermolecular forces, comparing to the experimental spectrum, absorptions are at higher wavelengths. To account for these forces and study the solvent effect on the spectrum, geometry minimization and time-dependent density functional theory calculations for Mo(VI, V) complex performed in a series of solvents with various dielectric constants: heptane ( $\epsilon = 1.9113$ ), pentanal ( $\epsilon = 10.0$ ), and water ( $\epsilon = 78.3553$ ). As can be seen from Figure 4-11, as dielectric constant of the solvent increases, the simulated

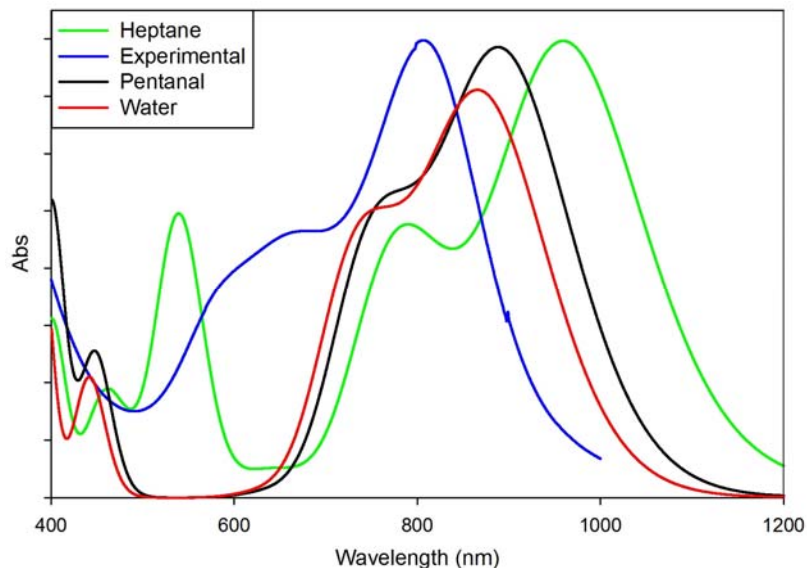


**Figure 4-11.** Experimental and simulated spectra for Mo(VI, V) dimer complex in various solvents

spectra is shifting to lower wavelengths close to experimental spectrum. The solvent with higher dielectric constant can be polarized more easily and hence will stabilize the charges on the complex more efficiently. As a result, excitations need more energy and occur at lower wavelengths. Figure 4-11 shows that the best simulation is when water is used as solvent in calculations.

Geometry optimization and time-dependent density functional theory calculation in water as solvent also performed for the Mo(V, V) complex. Figure 4-12 compares the simulated spectrum of this complex to experimental dimer complex spectrum. The simulated spectrum in water for this complex is very different than that of the experimental one. The spectrum shows strong absorptions below 600 nm of the experimental one which gives a red color to the complex and can not explain the blue color of the dimer complex. As a result, this leaves only one possibility for dimer complex: mixed-valence Mo(VI, V) complex.

As mentioned earlier, for the molybdenum gluconate 1:2 monomer complex, there are two possibilities: Mo(VI) or Mo(V). The simulation results for dimer complex suggest that the

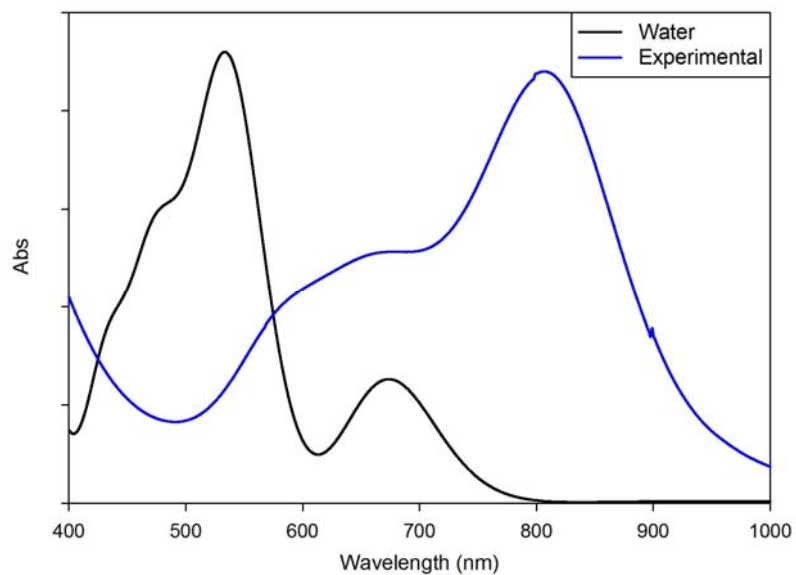


**Figure 4-12.** Experimental and simulated spectra for Mo(V, V) dimer complex in water

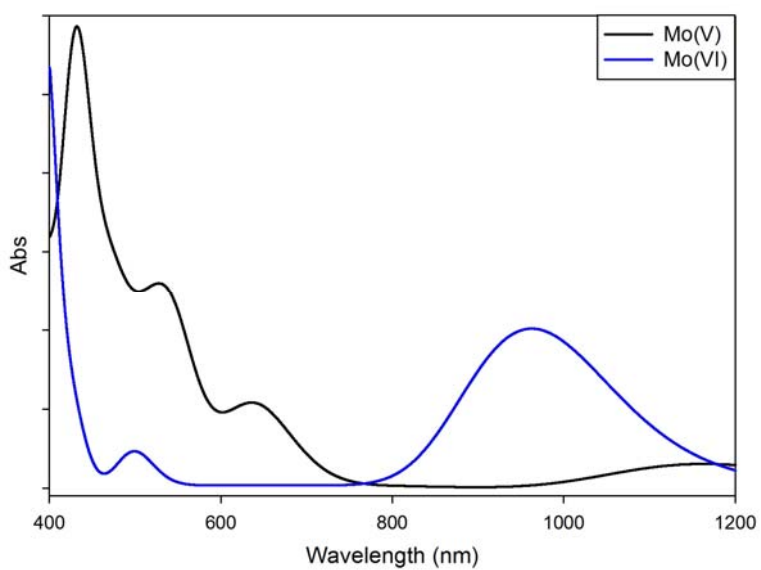
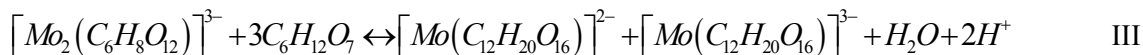


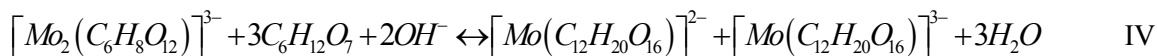
**Figure 4-13.** Simulated spectra for Mo(V) and Mo(VI) monomer complexes in water

best simulation is when the geometry optimization and time-dependent density functional theory calculations performed in water. Hence, geometry minimization and time-dependent density functional theory calculations performed for these monomer possibilities in water as solvent. Figure 4-13 shows the simulated spectra for these monomer complexes in water. The Mo(VI) monomer spectrum shows strong absorption below 500 nm, which gives a yellow color to the complex. In case of Mo(V) monomer absorptions in visible wavelengths are below 700 nm and the strongest one appears below 500 nm, which gives a yellowish color to the monomer complex. As a result, based on the simulated spectra in water for the dimer and monomer complexes the validity of the equilibrium II is confirmed.

Furthermore the vibrational frequencies were computed for these complexes and the thermochemistry data from frequency calculations was used to calculate the  $\Delta G$  for equilibrium II. The balanced dimer - monomer equilibrium can be written as:



This equilibrium can be arranged under basic conditions as:



Geometry optimization and vibrational frequency analysis calculations performed for all reactants and products in equilibrium IV and the Gibbs free energies from the frequency analysis data are used to calculate the Gibbs free energy of the equilibrium using the equation 4-4.

$$\Delta G_{equi} = \sum_{i=1}^{N_{products}} n_i \Delta G_i - \sum_{j=1}^{N_{reactants}} n_j \Delta G_j \quad (4-4)$$

**Table 4-3.** Computed  $\Delta G$  for equilibrium IV in gas phase and aqueous solution (Dipole) thomasi's model, (PCM) polarizable continuum model, (CPCM) conductor polarizable, and (SMD) universal solvation model

Model	Functional	Basis Set	Solvent	$\Delta G_{\text{equi}}$ (kJmol <sup>-1</sup> )
Gas Phase	B3LYP	6-311++G(d,p) LanL2DZ	N/A	64.69
Dipole	B3LYP	6-311++G(d,p) LanL2DZ	Water	130.21
PCM	B3LYP	6-311++G(d,p) LanL2DZ	Water	383.28
CPCM	B3LYP	6-311++G(d,p) LanL2DZ	Water	862.64
SMD	B3LYP	6-311++G(d,p) LanL2DZ	Water	507.97

, where  $\Delta G_{\text{equi}}$ ,  $\Delta G_i$ , and  $\Delta G_j$  are Gibbs free energy of equilibrium, products, and reactants respectively.

$\Delta G_{\text{equi}}$  were calculated in gas phase and in aqueous solution using various polarized continuum models, results are summarized in Table 4-3. Same functional and basis set as time-dependent density functional theory calculations were used for frequency analysis calculations. The gas phase calculation result is on the same order of experimental result.

For the aqueous phase calculations, there is not a universal approach and depending on the parameters used, the results are different. Generally in implicit solvation models, solvent is considered as an uniform dielectric medium characterized by the dielectric constant. Polarization of the solvent is expressed in terms of the surface charge density on the cavity surface, this polarization produces the electric field in the cavity making an effect on the solute. As can be seen from Table 4-3, the Dipole method gives the best result. The Dipole method puts the solute in spherical cavity and computes interaction of solute dipole with solvent. This method works

best for small molecules with dipole, and its better result comparing to other methods is probably because of cancellation of errors due to neglecting cavitation and dispersion. Other PCM models create cavity more realistically by putting spheres on each atom and considering the cavity as the surface created by interlocking of these spheres. The charge density on the surface interacts with the solvent, and cavitation and dispersion are also considered.

SMD model[69] is based on the polarized continuous quantum mechanical charge density of the solute which employs Coulomb radii and atomic surface tension coefficients as parameters. Although this model has been claimed as universal solvation model, it has not been optimized for solutes containing transition metals and utilizing it for molybdenum gluconate complexes does not produce better result comparing to other solvation models.

Comparing the results of various solvation models with gas phase and experimental results shows that these models do not produce acceptable results due to parameters used in these models. To improve the results in aqueous solution, either these models have to be parameterized properly for molybdenum gluconate complexes or more expensive explicit and hybrid implicit-explicit models have to be utilized.

#### **4.4 Summary**

The equilibrium between dimer and monomer molybdenum gluconate complexes were studied experimentally by means of UV-Vis spectroscopy. The calculated activation energy  $E_a$ , for this equilibrium is  $53 \pm 14 \text{ kJmol}^{-1}$ , and the calculated  $\Delta G$  for this equilibrium, assuming that initially there is no monomer complex, is  $42 \pm 5 \text{ kJmol}^{-1}$ .

The structure of several Mo(VI) and Mo(V) complexes were optimized utilizing density functional theory (DFT) calculations and UV-Vis spectra were simulated using time-dependent

density functional theory (TDDFT), framework in both gas and aqueous phases. Simulated spectra in aqueous phase properly describe blue and yellow colors of dimer and monomer complexes.

The attempt to calculate  $\Delta G_{\text{equi}}$  using frequency calculations was unsuccessful, specially for aqueous solution using continuum polarizable solvation models. The error in gas phase is reasonable due to assuming that all species are isolated and there is no interaction. For the aqueous phase calculations the results are much worse than gas phase result. To improve the aqueous phase results, either parameters should be optimized for the complexes, or more expensive explicit and hybrid implicit-explicit models should be used.

## CHAPTER V

### ENVIRONMENTAL CORROSION RATES OF IRON AND ZINC WIRES

American Society for Testing and Materials (ASTM), defines corrosion as "the chemical or electrochemical reaction between a material, usually a metal, and its environment that produces a deterioration of the material and its properties"[110]. Millions of dollars are lost each year because of corrosion induced damage, a large percentage from the corrosion of iron and steel parts of equipments and underground metal structures in various industries. In addition to the corrosion cost directly from metallic structures damage which forces replacement of structures and buildings, other costs of corrosion are related to corrosion control and the cost of designing new materials[71]. Therefore, the study of corrosion and corrosion inhibition have attracted many scientists.

In this chapter, a new data collection method for the corrosion rate, based on the measurement of the resistance of small wires, is presented. Additional background on corrosion can be found in the introduction. This method is used to study the corrosion of iron and zinc wires in sodium chloride solutions. In addition, to demonstrate the potential of this method, corrosion studies with selected corrosion inhibitors were performed.

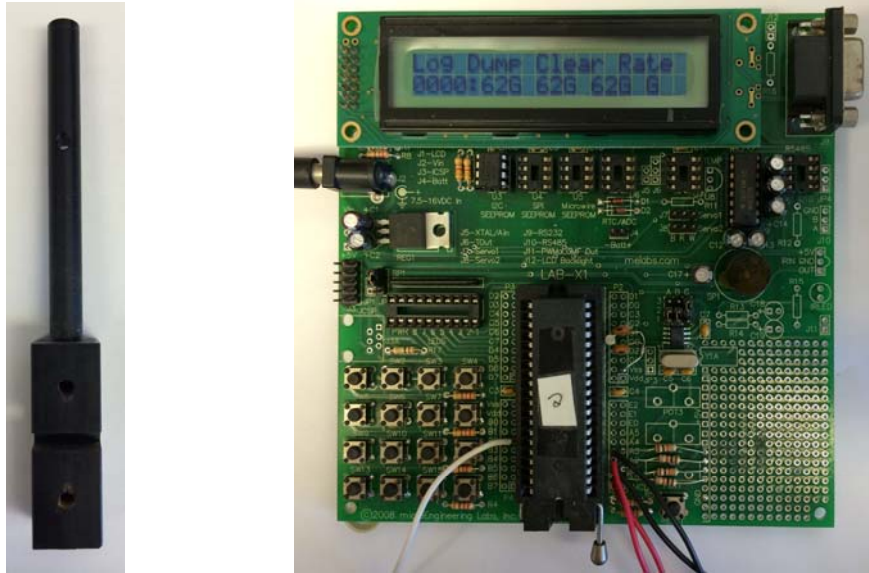


**Figure 5-1.** (left) Wire holder, (right) Data collection board.

### **5.1 Corrosion of Iron and Zinc Wires in Sodium Chloride Solution**

The most common laboratory corrosion test method is the immersion test. In this method sample is immersed in corrosive media for a known period of time and the weight difference before and after immersion is considered as amount of corrosion. This procedure is time consuming, as it requires periodical removing of the sample from the corrosive media and weighting after several cleaning steps. In this dissertation, a new method based on the corrosion of small wires is used to evaluate corrosion. In this method small wires of known radii are installed on a holder, all the connections are sealed and only a known length of the wires are exposed to corrosive media, the wires are connected to a data collection electronic board (Figure 5-1), and immersed in corrosive media. The electronic board measures and saves the resistance of the wire periodically, the wire failure time is detected easily by plotting the wire resistance against time, Figure 5-2 shows a typical plot for corrosion of iron wire ( $r = 0.065$  mm) in sodium chloride 5% solution. Since both the length of wire and the radius are known, the mass exposed to corrosive media can be calculated and weight loss determined. The corrosion rate is then determined from the slope of the plot of weight loss for wires of various radii versus time.

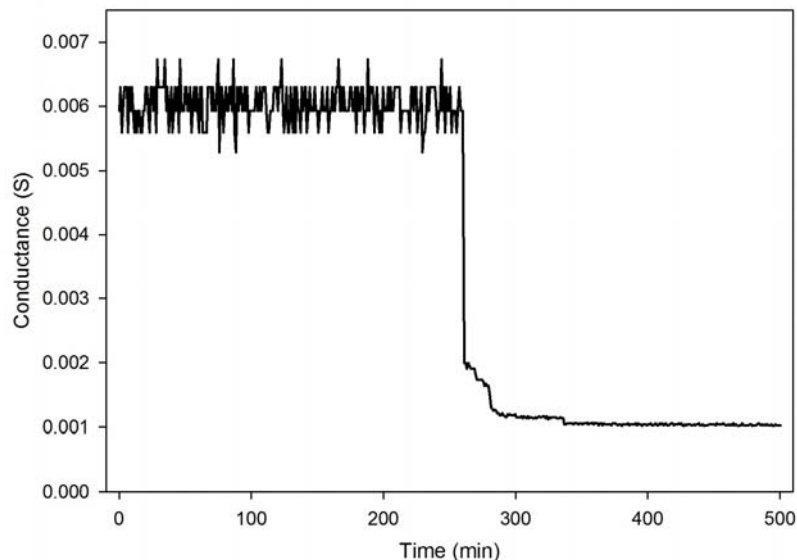


**Figure 5-2.** Wire conductance change with time for iron wire ( $r=0.065$  mm) in sodium chloride 5% solution.

The ASTM G1[111] procedure has been followed for cleaning and preparation of iron and zinc wires (purity >99%, from AlfaAesar and Goodfellow) . In this procedure Oakite solution (6g Oakite from Chemetall dissolved in 100 ml deionized water at 80 °C) and hexamethylenetetramine (HMTA) solution (0.35g hexamethylenetetramine in 50ml deionized water and 50ml concentrated hydrochloric acid) were used. Zinc wires were rinsed with hexane and degreased in Oakite solution for 10 min at 65°C and then rinsed with deionized water, acetone, and hexane and kept in desiccator for future use. Iron wires were rinsed with hexane and degreased in Oakite solution for 10 min at 65°C, rinsed with deionized water, acetone, and hexane. Then any rust were removed using hexamethylenetetramine solution for 10 min. The specimens were then rinsed with deionized water, acetone, and hexane and kept in desiccator for future use.

Following the ASTM G31[112] guide for laboratory immersion test, iron wires of known diameter after cleaning were installed on wire holder, all the connections were covered using

**Table 5-1.** Corrosion time of iron wires in sodium chloride 0.5% and 5% solutions.

r (mm)	Weight (mg)	0.5% NaCl		5% NaCl	
		Time (hr)	STDEV	Time (hr)	STDEV
0.065	0.3343	26.19	6.70	16.72	12.03
0.075	0.4450	20.46	3.40	29.46	5.55
0.1	0.7912	19.89	11.86	28.75	32.08
0.125	1.2362	102.87	10.39	109.63	30.19
0.25	4.9449	259.68	31.15	365.03	46.54

silicon caulk and were left overnight at room temperature to dry, only a known length (3.2 mm) of the wires are in contact with the solution. Then, wires were connected to electronic data collection board and immersed in the corrosive solution. The electronic board reads and saves the resistance of wires in specified time intervals, so corrosion time can be determined. Corrosion times for iron wires in sodium chloride 5% and 0.5% solutions are summarized in Table 5-1 and Figure 5-3 shows the corresponding weight loss versus time plots. It can be seen from plots that, for wires of small radii (up to 0.1 mm), corrosion times are very close and as wire radius increases, the corrosion time increases rapidly. The iron oxide produced by corrosion forms a protective layer on the wire which acts as a barrier for diffusion of corrosive chloride ions to the surface of metal. Thinner wires have small mass and are corroded completely before the iron oxide layer forms.

The corrosion rate is defined as the amount of weight loss in unit time and calculated using equation 5-1:

$$Rate = \frac{\Delta w}{t} \text{ mg/hr} \tag{5-1}$$

, where  $\Delta w$  is weight loss and  $t$  is corrosion time. Using this equation and slopes of plots in Figure 5-3, the corrosion rates in 0.5% and 5% sodium chloride solutions are  $0.018 \pm 0.001$  mg/hr and  $0.014 \pm 0.001$  mg/hr respectively, which are basically same.

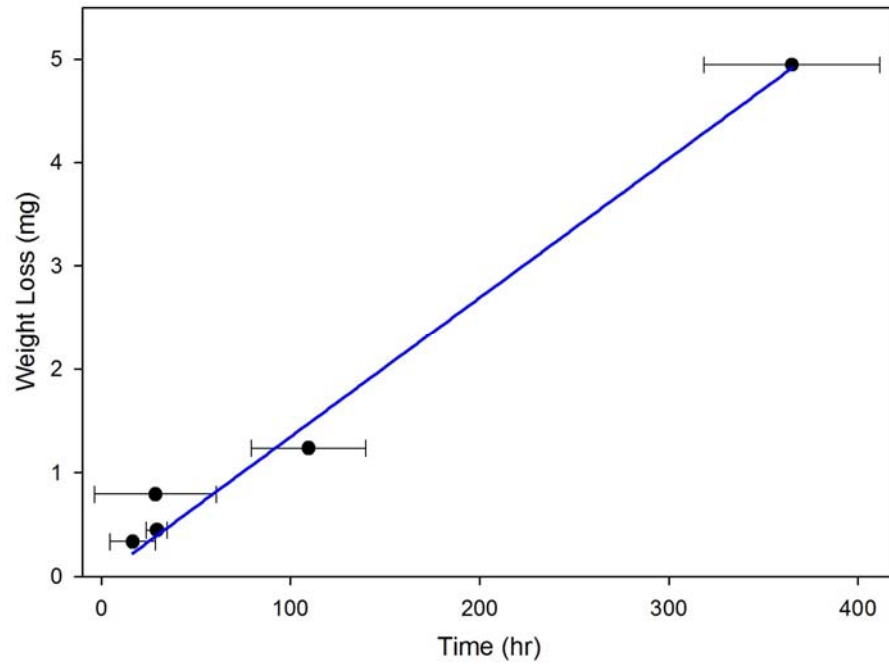
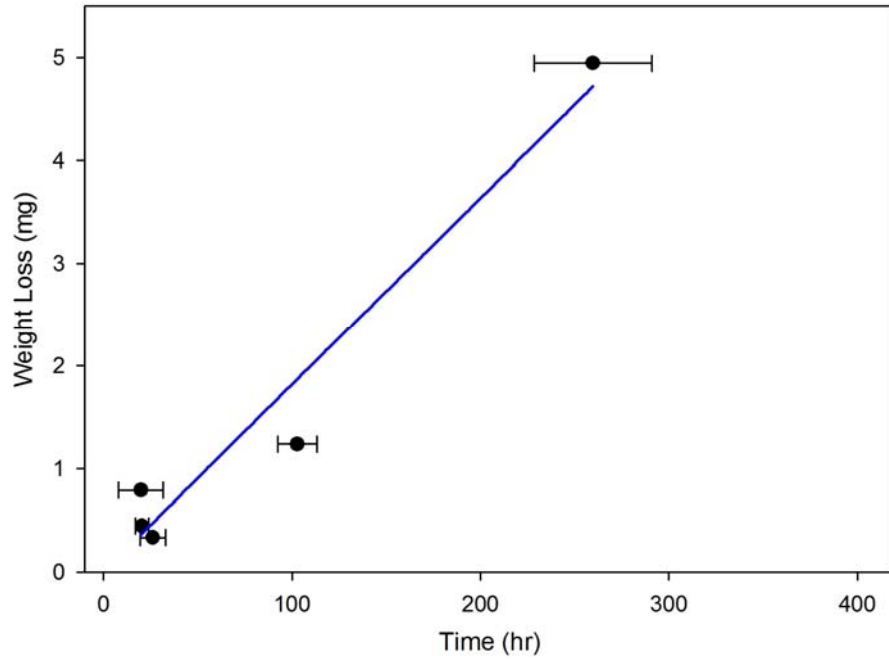


**Figure 5-3.** Weight loss of iron wires in sodium chloride solutions.

(top) NaCl 0.5%, (bottom) NaCl 5%

The corrosion of metals in solution is the result of combination of anodic oxidation of metal and cathodic reduction of oxygen in the solution. In the case of iron corrosion these reactions can be written as bellow:



Oxidation of the iron metal produces  $Fe^{2+}$  ions and reduction of dissolved oxygen results in  $OH^{-}$  ions. The reaction of  $Fe^{2+}$  and  $OH^{-}$  ions produces insoluble iron(II) hydroxide  $Fe(OH)_2$ , ( $K_{SP} = 2 \times 10^{-15}$ ), which gradually is oxidized to iron(III) oxide  $Fe_2O_3$ , in presence of dissolved oxygen. This insoluble film, generated on the surface of the iron wire, acts as a passive film by restricting the diffusion of the oxygen to the iron wire surface. Hence, at the early stages of the corrosion, before generation of the passive film, corrosion is fast and then corrosion rate is controlled by the diffusion of the oxygen to the surface of the metal (Figure 5-3).

In aqueous media, the passive layer reacts with aggressive  $Cl^{-}$  ions in solution and produces iron oxychloride ( $FeOCl$ ). Iron oxychloride in the solution is hydrolyzed gradually producing soluble iron(III) chloride  $FeCl_3$ . Consequently, the passive oxide layer breaks down and corrosion proceeds further[113, 114].



**Table 5-2.** Corrosion time of zinc wires in sodium chloride 5% solution.

r (mm)	Weight (mg)	Time (hr)	STDEV
0.025	0.0448	1.32	0.33
0.05	0.1794	10.90	3.72
0.125	1.210	21.92	5.81
0.25	4.4839	142.19	28.07

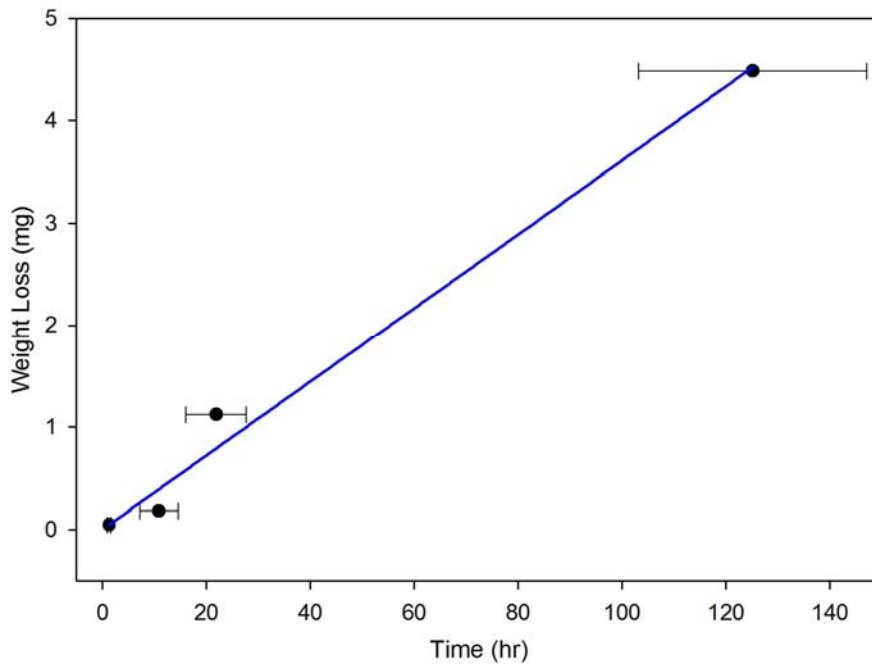


**Figure 5-4.** Zinc wires weight loss in sodium chloride 5% solution

In addition to iron wires, the corrosion of zinc wires in sodium chloride 5% solution was studied following the same procedure as iron wires. Table 5-2 summarizes the corrosion times of zinc wires and data is plotted in Figure 5-4. From the slope of the plot in Figure 5-4, the corrosion rate of the zinc wires in sodium chloride 5% solution is  $0.036 \pm 0.002$  mg/hr. The corrosion of

zinc metal follows the same procedure as iron metal (reactions VII ~ X). It starts with oxidation of zinc metal and reduction of dissolved oxygen resulting in the  $Zn^{2+}$  and  $OH^-$  ions. Then insoluble zinc hydroxide  $Zn(OH)_2$ , ( $K_{sp} = 3 \times 10^{-17}$ ), is produced which gradually generates the zinc oxide,  $ZnO$ . Similar to the case of iron, this passive film breaks down in the presence of  $Cl^-$  ions, producing the soluble zinc chloride,  $ZnCl_2$  and allows the corrosion to proceed[115, 116].



## 5.2 Corrosion Inhibitors

Corrosion is controlled by many methods such as coating, phosphating, anodic or cathodic controls, and corrosion inhibitors. Among these methods, use of solution based inhibitors is both convenient and economical. Hundreds of corrosion inhibitors are reported and the most effective ones are chromates and dichromates[117]. However, these compounds are toxic and the use of them is either restricted or banned by regulations[118]. Therefore, most of the researches focused on the compounds, which are more environmentally friendly. Among these environmentally compatible compounds, gluconates and gluconic acids are the most attractive compounds due to their low cost, effectiveness, and nontoxic nature [119]. There are many reports regarding to ability of gluconates to hinder the corrosion, for example, Rajendran and co-workers[120], studied the corrosion inhibition ability of calcium gluconate on mild steel in 60 ppm  $Cl^-$  ion solution.

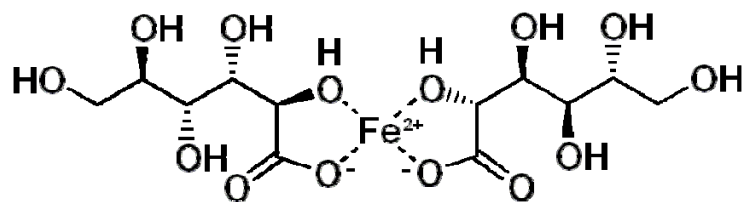
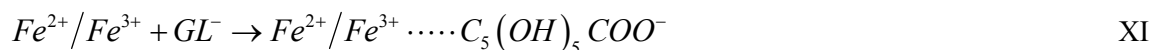


**Figure 5-5.** Iron gluconate complex structure.

The effectiveness of gluconates as corrosion inhibitors on corrosion due to anodic dissolution of metals and cathodic reduction of oxygen, depends on concentration of inhibitor and the nature of cation introduced into the solution[121]. For the corrosion inhibition by gluconates, various mechanism are considered: gluconates are adsorbed on weak spots of protective metal oxide films on metal surface and repair it, gluconates can incorporate in protective metal oxide film formation, and  $Fe^{3+}$  ions generated by anodic dissolution of iron react with gluconates and be precipitated on metal surface again[122].

Calcium gluconate dissociates to  $Ca^{2+}$  and gluconate ion  $GL^-$ ,  $[C_5(OH)_5COO^-]$ , in aqueous medium and gluconate ions form chelate complex with iron ions[123] (Figure 5-5):



When fresh, cleaned iron wire is immersed in sodium chloride solution,  $Fe^{2+}$  ions from oxidation of iron by dissolved oxygen, are chelated by gluconate ions, resulting in further oxidation of iron wire. Then gluconate ions diffuse on the surface of wire and chelate  $Fe^{3+}$  ions of the protective layer. This adsorbed layer blocks the absorption of  $Cl^-$  ions on the oxide surface preventing oxide layer dissolution through soluble iron oxychloride  $FeOCl$ , formation. In this way, calcium gluconate inhibits iron corrosion in presence of corrosive  $Cl^-$  ions.

The same corrosion test method, using wire holder and data collection board, was used to study the corrosion of iron wires in sodium chloride 0.5% solution containing various amounts of calcium gluconate as corrosion inhibitor. Iron wire, ( $r = 0.075$  mm), was cleaned following the ASTM G1 standard procedure, installed on wire holder, all the connections covered with silicon caulk, after drying the caulk, wire connected to data collection board, immersed in the sodium chloride - inhibitor solution and data logging was started. The corrosion times and corrosion inhibition efficiencies for the iron wire are summarized in Table 5-3 and plotted in Figure 5-6. The corrosion inhibition efficiencies (IE) are calculated using equation 5-2:

$$IE = \frac{R_1 - R_2}{R_1} \times 100 \quad (5-2)$$

, where  $R_1$  and  $R_2$  are corrosion rates in absence and presence of inhibitor respectively.

At low concentrations of inhibitor, the corrosion of wire is faster comparing to the case without inhibitor. In other word calcium gluconate accelerate the corrosion, and then corrosion time increases with increasing the inhibitor concentration. This is in excellent agreement with Gunasekaran and co workers[114].

**Table 5-3.** Corrosion inhibition efficiency of calcium gluconate.

Iron wire ( $r = 0.075$  mm) in sodium chloride 0.5% solution

Inhibitor (ppm)	Time (hr)	Rate (mg/hr)	IE (%)
1	11.15	0.0399	-121.74
10	7.30	0.0610	-238.69
50	443.20	0.0010	94.42
100	1460.00	0.0003	98.31

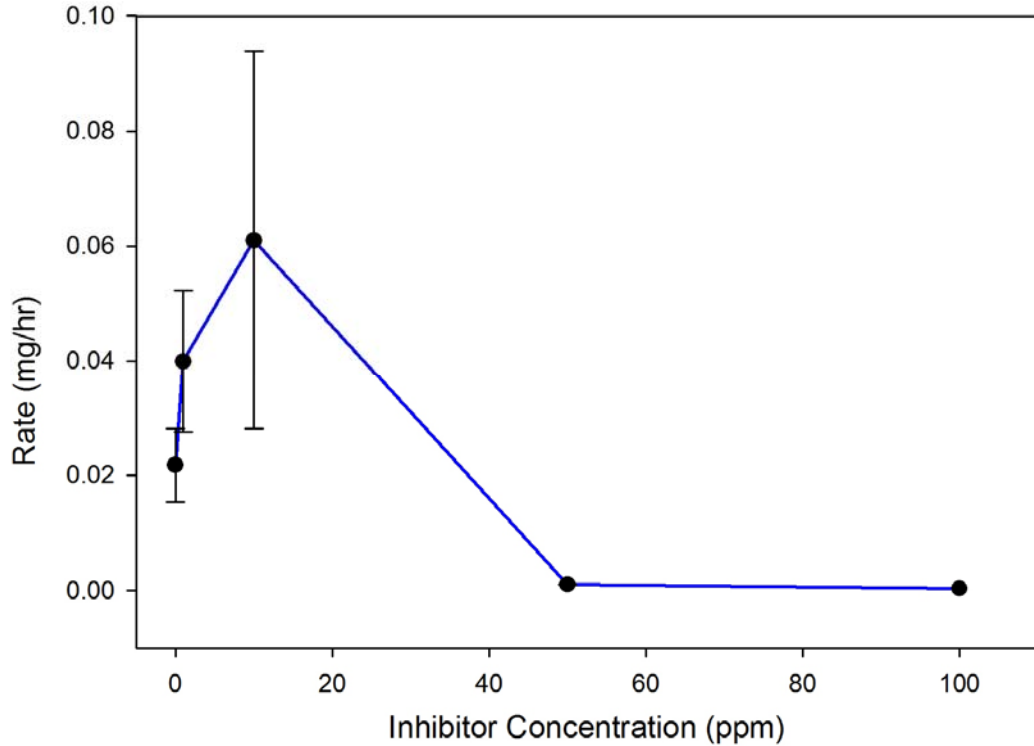


**Figure 5-6.** Iron wire corrosion rate in sodium chloride 0.5% solution in presence of calcium gluconate as inhibitor

To further evaluate the applicability of wire trigger system for corrosion inhibition efficiency tests, corrosion inhibition efficiency for a few commercial inhibitors were examined in sodium chloride 0.5% solution. The results are summarized in Table 5-4. The corrosion time of the iron wire ( $r = 0.075$  mm), was measured at two concentrations of Amerex 507 (from AMEREX Corp.), at recommended concentrations of Prestone antirust (from Prestone Corp.), and Broco RPA antirust (from Singleton Corp.). As can be seen from Table 5-4, Broco RPA at recommended concentration is the most effective inhibitor among the commercial corrosion inhibitors.

**Table 5-4.** Corrosion inhibition efficiency of commercial inhibitors.  
 Iron wire in sodium chloride 0.5% solution  
 (a) Recommended concentration

Inhibitor	Inhibitor (ppm)	Time (hr)	Rate (mg/hr)	IE (%)
Amerex 507	100	576	0.0008	95.71
	10000	898	0.0005	97.25
Prestone	37688 <sup>a</sup>	302	0.0015	94.81
Broco RPA	10000 <sup>a</sup>	2984	0.0001	99.17

### 5.3 Summary

A new wire trigger system was used to run the laboratory corrosion tests. This method is based on the corrosion of small wires while the resistance of wire is measured and collected automatically using an electronic board. The required time for the complete corrosion of the wire is determined from the plot of resistance versus time. Using the wires of various radii and measuring the triggering time, the corrosion rate can be calculated for the metal in the corrosive environment.

The results for the corrosion of iron and zinc wires utilizing this method show that it can be used as a simple method to study the corrosion of metals in corrosive environment. This method also utilized for the evaluation of inhibition efficiency of calcium gluconate and some commercial inhibitors. The results prove that wire trigger system is a simple and effective method, which can be utilized to study the corrosion of metals and determine the efficiency of inhibitors.

## CHAPTER VI

### CORROSION IN SOIL

Although there are many transportation methods, due to safety considerations, the preferred method for the transportation of water, natural gas, oil, and refined hydrocarbons is using the buried pipelines. In the United States there are about 2 million km of buried natural gas pipeline and about 280,000 km of petroleum products pipelines[124]. Material degradation in the soils is very significance economic concern and there are many procedures to evaluate the corrosion of metals in soils. More detailed information about corrosion in soil and corrosion detection methods can be found in the introduction.

In Uhlig's Corrosion Handbook, soils are defined as admixture of rock disintegrated by physical action and modified by weathering, materials precipitated chemically from aqueous solution, and organic matter[124]. Muskegs, Peat Bogs, and Swamps are admixture of decaying organic matter with minor amounts of inorganic material. In contrast other soils consist of mainly inorganic materials broken and weathered to various particle sizes. Given such variety of soil types, various corrosion mechanisms are expected. The main factors that influence the corrosion of materials in soils, based on soil type, can be listed as: moisture content, soluble ion content, and pH.

Since the transportation of ions and oxygen is taken place through water, the presence of moisture in the soil is a key requirement for corrosion. In general, as the soluble ion content of soil increases, the soil conductivity increases, which in turn facilitates the electron transfer leading to faster corrosion. The pH of the soil is another major factor affecting the corrosion of material in the soil. Depending on the soil content, the pH of soil changes, soils containing humified organic matter tend to be acidic. The corrosion of iron increases considerably at pH values less than 4 and at high pH values passivation occurs[125].

In this chapter, the corrosion of mild steel coupons is first studied based on weight loss. After which, a new data collection method for the corrosion rate measurement is used to study the galvanic corrosion of zinc wires in soil. Finally, the results from corrosion of mild steel coupons and galvanic corrosion of zinc wires in soil experiments are used to develop a passive wireless corrosion sensor. This sensor works based on the galvanic corrosion of zinc metal and is used for the corrosion detection in soils containing various amounts of sodium chloride. For the sensor experiments, zinc wire is connected to mild steel coupons or small iron pipes.

## **6.1 Corrosion of Mild Steel Coupons in Soil**

The corrosion of mild steel coupons of 1" × 1" dimensions buried in soil were studied following the ASTM G162 standard procedure[126]. Two types of commercially available soils from Scotts Company LLC were used in this study: Earthgro potting soil (EG), and Miraclegro potting mix (MG). Earthgro soil contains more sand and Miraclegro soil contains more organic matter. Also, to accelerate the corrosion, 0.5% and 5% by weight sodium chloride and soil mixtures were prepared and used for the tests (indicated as EG-0.5, MG-0.5, EG-5, and MG-5).

The coupons were cleaned three times according to the ASTM G1 standard procedure and weighted. After which, the coupons buried in soils following the ASTM G162 standard

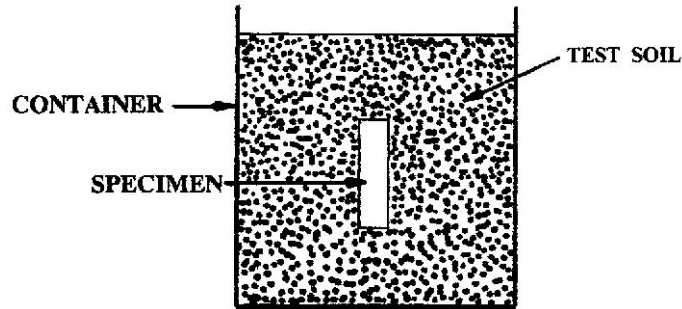


**Figure 6-1.** Apparatus for corrosion test in soil. (Figure adapted from Ref [126])

procedure, 200 ml deionized water added to each test container and sealed (Figure 6-1). Control samples were kept in desiccator. Every two weeks four coupons were taken out of the soils, cleaned three times and weighted. Two control samples for each data point were used, and the difference between weight losses of control samples and samples buried in soils considered as weight loss due to corrosion. The weight loss data for corrosion of mild steel coupons buried in Earthgro and Miraclegro soils are summarized in Table 6-1 and 6-2 and plotted in Figure 6-2 and 6-3, respectively.

Equation 6-1 is used for the calculation of corrosion rates per unit area:

$$Rate = \frac{\Delta w}{t \cdot A} \quad \text{mg/day} \cdot \text{mm}^2 \quad (6-1)$$

, where  $\Delta w$  is weight loss,  $t$  is corrosion time, and  $A$  is the surface area. Based on experimental data, the corrosion rates in soils with various amounts of sodium chloride are summarized in Table 6-3. For both types of soils, the corrosion rate increases as the sodium chloride content increases, and corrosion rates in earthgro soils are lower than those in miraclegro soils. The miraclegro soil, unlike earthgro soil that is composed of mainly sand, contains high amount of organic matter, resulting in better contact between coupons and soil leading to higher corrosion rates. In addition, since the earthgro soil contains high amounts of sand, it is difficult to make a

**Table 6-1.** Weight loss of mild steel coupons in Earthgro (EG) soils with various sodium chloride content.

(EG) earthgro soil, (EG-0.5) earthgro soil with 0.5% by weight sodium chloride, and (EG-5) earthgro soil with 5% by weight sodium chloride

Time (Day)	Soil	14	28	42	56	70	84
Weight Loss (mg/mm <sup>2</sup> )	EG	0.0111	0.0091	0.1235	0.0098	0.0279	0.0115
	EG-0.5	0.0201	0.0211	0.0944	0.1943	0.2679	0.1106
	EG-5	0.0688	0.1196	0.2172	0.3758	0.0572	0.4534

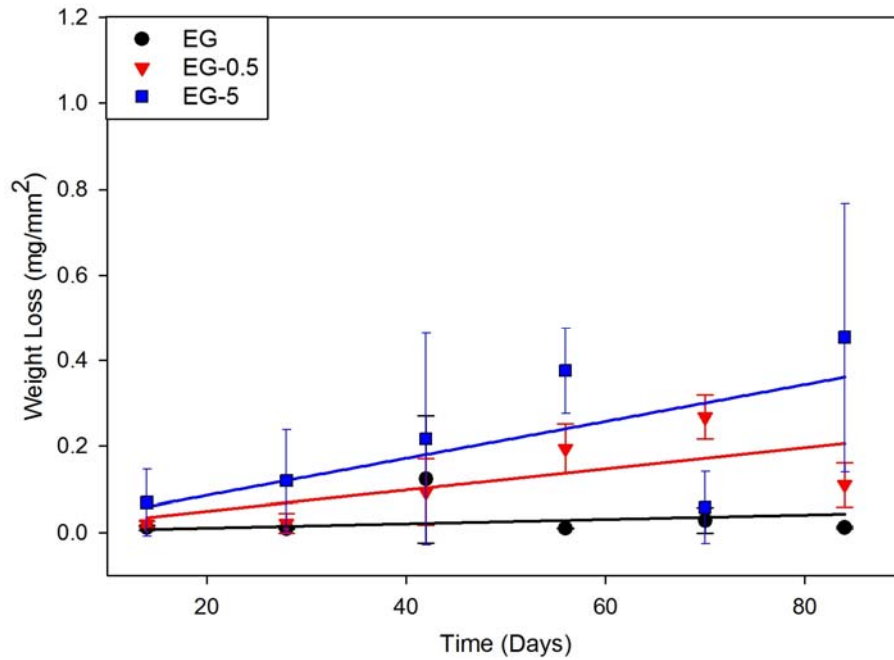


**Figure 6-2.** Weight loss of mild steel coupons in Earthgro (EG) soils with various sodium chloride content.

(EG) earthgro soil, (EG-0.5) earthgro soil with 0.5% by weight sodium chloride, and (EG-5) earthgro soil with 5% by weight sodium chloride

**Table 6-2.** Weight loss of mild steel coupons in Miraclegro (MG) soils with various sodium chloride content.

(MG) miraclegro soil, (MG-0.5) miraclegro soil with 0.5% by weight sodium chloride, and (MG-5) miraclegro soil with 5% by weight sodium chloride

Time (Day)	Soil	14	28	42	56	70	84
Weight Loss (mg/mm <sup>2</sup> )	MG	0.1114	0.1897	0.2835	0.2950	0.3658	0.4314
	MG-0.5	0.1713	0.3495	0.4496	0.6516	0.7225	0.8982
	MG-5	0.1842	0.3817	0.5777	0.8228	0.9539	0.9604

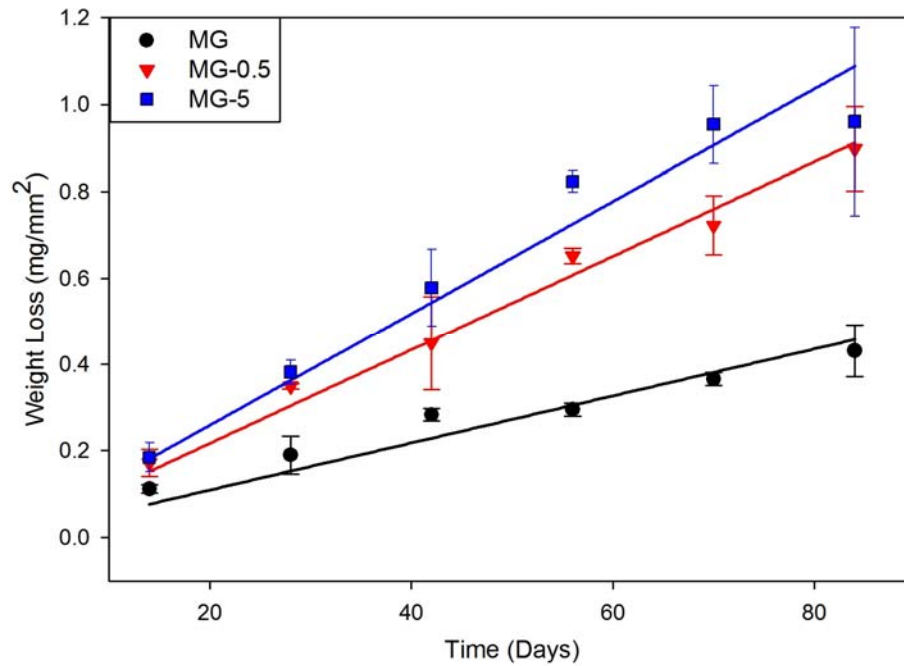


**Figure 6-3.** Weight loss of mild steel coupons in Miraclegro (MG) soils with various sodium chloride content.

(MG) miraclegro soil, (MG-0.5) miraclegro soil with 0.5% by weight sodium chloride, and (MG-5) miraclegro soil with 5% by weight sodium chloride

**Table 6-3.** Corrosion rate of mild steel coupon in soils with various sodium chloride content.

(MG) miraclegro soil, (MG-0.5) miraclegro soil with 0.5% by weight sodium chloride, and (MG-5) miraclegro soil with 5% by weight sodium chloride

Type	Rate (mg/day.mm <sup>2</sup> )
EG	$5 \times 10^{-4} \pm 4 \times 10^{-4}$
EG-0.5	$2.5 \times 10^{-3} \pm 5 \times 10^{-4}$
EG-5	$4.3 \times 10^{-3} \pm 1 \times 10^{-3}$
MG	$5.4 \times 10^{-3} \pm 3 \times 10^{-4}$
MG-0.5	$1.09 \times 10^{-2} \pm 3 \times 10^{-4}$
MG-5	$1.30 \times 10^{-2} \pm 6 \times 10^{-4}$

homogeneous soil environment around the coupons and so the weight loss results for this type of soil are scattered.

## 6.2 Galvanic Corrosion of Zinc Wires in Soil

Galvanic corrosion of metals is one of the most common corrosion types that cause damage to metallic structures. In galvanic corrosion, one metal which is less noble corroded through oxidation (anodic) reaction and the other metal which is more noble reduced (cathodic reaction) in a corrosive medium. The anodic and cathodic reactions are as bellow:



The electrons generated by oxidation at the anode travel to cathode through electrical connection. At the cathode, the electrons reduce the metal oxide generated by a corrosion event. Soil acts as a conduit for ion migration, moving metal ions from the anode to cathode. The anode metal, as a result, corrodes more quickly while cathode metal corrodes more slowly.

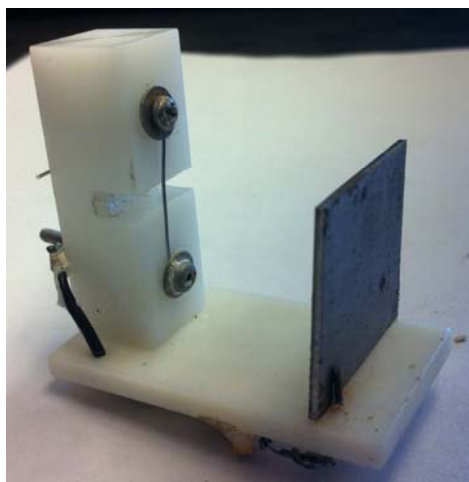


**Figure 6-4.** Zinc wire and mild steel coupon installed on holder for galvanic corrosion test.

To study the galvanic corrosion of zinc in soil, miraclegro type soil was chosen for the test since the corrosion of mild steel coupons in this type of soil is more reproducible (Figure 6-3). To increase the corrosion rate the highest percent of sodium chloride (5%) was chosen to accelerate the test. Zinc wires of known diameter and mild steel coupons were cleaned and prepared for the test following the ASTM G1 standard. The wires and mild steel coupons were installed on holder (Figure 6-4), after which, all the connections were covered with silicon caulk and left overnight at room temperature to dry. The wires were then connected to data collecting board and the holder was buried in miraclegro soil, 200 mL deionized water added and data collection was started.

After complete corrosion of zinc wires, corrosion times were determined by plotting the data (wire resistance versus time) and used to plot the weight loss of zinc wires versus time to calculate the corrosion rate. The galvanic corrosion data of zinc wires are summarized in Table 6-4 and plotted in Figure 6-5. The calculated galvanic corrosion rate of zinc wires connected to mild steel coupons in miraclegro soil containing 5% sodium chloride from the slope of the plot in Figure 6-5 is equal to  $1.04 \pm 0.15 \text{ mg/hr}$ .

**Table 6-4.** Data for galvanic corrosion of zinc wires connected to mild steel coupons in Miraclegro soil containing 5% sodium chloride by weight (MG-5).

r (mm)	Weight Loss (mg)	Time (hr)	STDEV
0.25	4.945	1.5	1.58
0.5	19.780	4.0	0
1	79.118	76.7	3.30

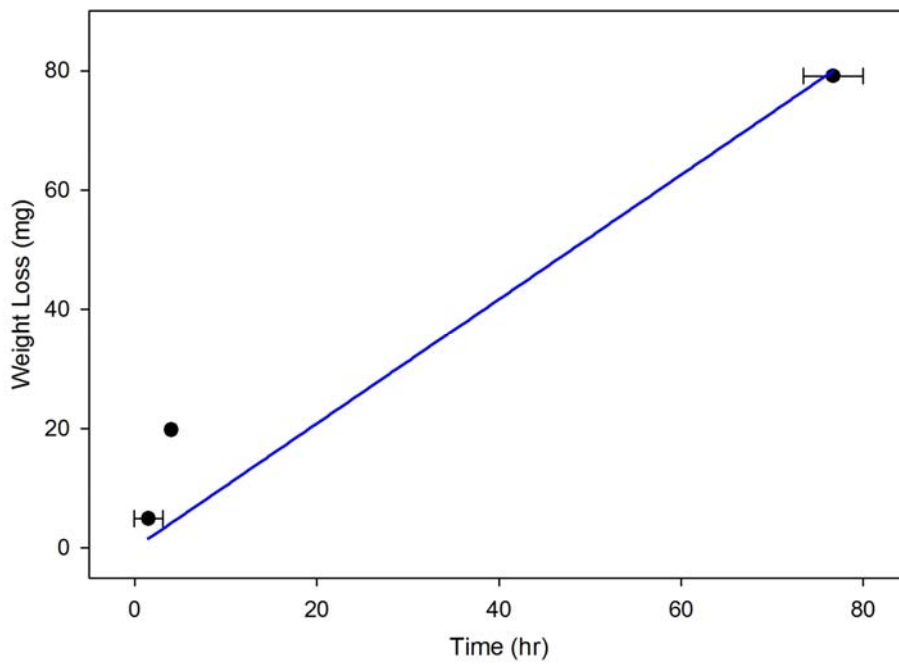


**Figure 6-5.** Weight loss of zinc wires due to galvanic corrosion in miraclegro soil containing 5% sodium chloride by weight (MG-5).

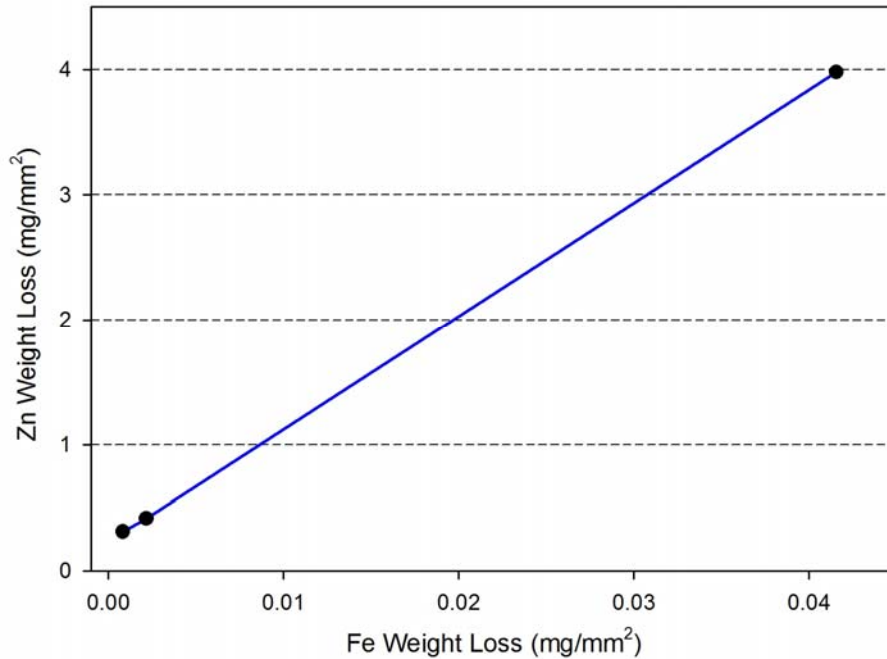


**Figure 6-6.** Galvanic corrosion of zinc wires and expected corrosion of mild steel coupons in miraclegro soil containing 5% sodium chloride by weight (MG-5)

Figure 6-6 compares the weight loss of zinc wire due to galvanic corrosion with expected weight loss of mild steel coupons due to corrosion in miraclegro soil containing 5% sodium chloride. The galvanic corrosion rate for zinc is  $2.48 \pm 0.36$  mg/day.mm<sup>2</sup> when connected to a mild steel coupon. Thus, the galvanic corrosion of zinc is about one hundred times faster than the corrosion of the mild steel coupons and can be used as a measure to monitor the corrosion of mild steel coupons. This concept can be used to determine the mild steel corrosion amount and take the proper actions before losing large amount of mild steel due to corrosion. This idea is used to make a wireless corrosion sensor, which is described in next section.

### 6.3 Corrosion Sensor for Pipelines

Because of the importance of the buried infrastructures such as pipelines and rebars in concrete, detection and monitoring of the corrosion of these infrastructures is very essential

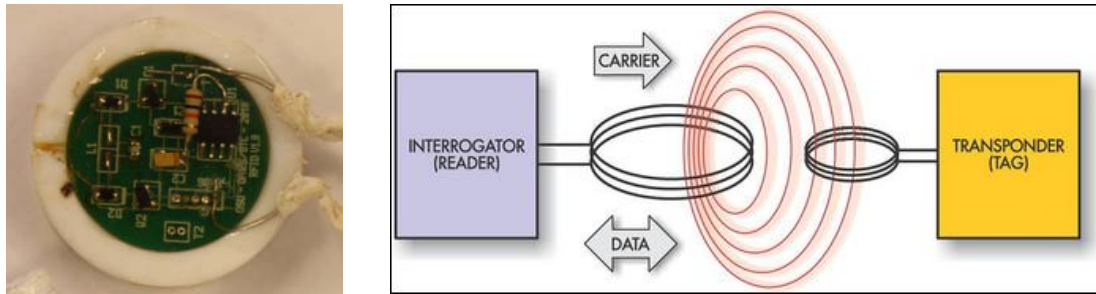


**Figure 6-7.** (left) Passive wireless corrosion sensor  
(right) Passive radio frequency identification (RFID) system

economically. As described in section 6-2, the galvanic corrosion of zinc wires is much faster than the corrosion of mild steel coupons in soil environment. This concept is used to develop a passive wireless sensor using a standard radio frequency identification (RFID) technology tag by replacing a section of the receiver coil, which is wrapped around the parameter of the device (Figure 6-7 left). This device is inexpensive, wireless, and requires no internal power. The response of the sensor can be easily read using an radio frequency identification reader and the lack of the signal indicates that the wire is corroded. This sensor works based on mutual inductance of electromagnetic field. The reader's antenna sends electromagnetic wave to radio frequency identification tag antenna, this wave powers up the tag and reflected electromagnetic wave transmits the radio frequency identification tag information to the reader (see Figure 6-7 right).

To examine the sensor response to the galvanic corrosion of the zinc wire in the soil, three galvanic corrosion tests in miraclegro soil containing 5% sodium chloride by weight were conducted using zinc wire (0.5 mm), connected to a mild steel coupon, a small pipe (38mm×10mm), and the same pipe with a small area exposed to the soil. For the first experiment, mild steel coupon was cleaned following the ASTM G1 standard procedure and along with the zinc wire installed on the holder (Figure 6-8 left). After connecting the zinc wire to the sensor, whole assembly was buried in miraclegro soil containing 5% sodium chloride by

**Table 6-5.** Galvanic corrosion of zinc wires in Miraclegro soil containing 5% sodium chloride by weight (MG-5).

Times collected using the sensor are compared to corrosion time determined using data collecting board.

\* Expected iron mass loss based on coupon corrosion in MG-5 soil.

Set-Up	No Sensor	Sensor		
	Coupon	Coupon	Pipe	Painted Pipe
Corrosion Time (hr)	4±0	6±1	4.4±0.9	46±4
Corrosion Rate (mg/hr)	0.045	0.033	0.041	0.004
Iron Mass Loss (mg/mm <sup>2</sup> )*	0.002	0.003	0.002	0.025

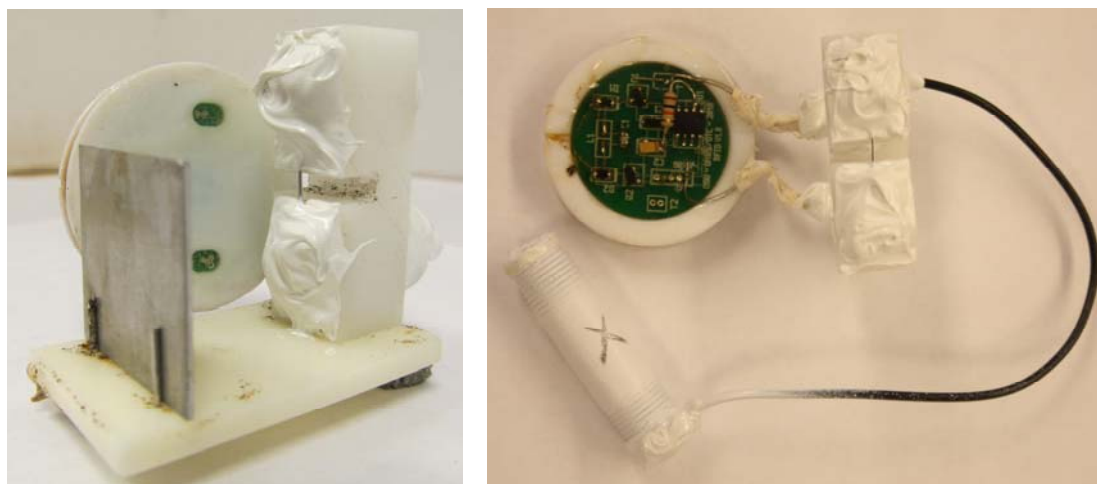


**Figure 6-8.** Sensor system for zinc galvanic corrosion in miraclegro soil containing 5% sodium chloride by weight (MG-5).

(left) Zinc wire connected to mild steel coupon  
(right) Zinc wire connected to small painted pipe

weight, 200 mL de-ionized water added and sensor signal was read periodically. The small pipes were used directly without further cleaning with the same test set-up. In addition, small pipes were covered by semi - gloss protective enamel, a small area of the pipe was exposed to the soil and used as the galvanic connection in the corrosion test, (Figure 6-8 right). As can be seen from Table 6-5, the corrosion time determined by the sensor is in agreement with the galvanic corrosion time of zinc wire determined using data collecting board (Table 3-3). Also, when just a small part of the pipe is exposed to the corrosive environment, the corrosion time is about ten times longer than that of uncovered pipe. The expected mass loss of mild steel coupons during the experiment period were calculated based on the corrosion rate determined for mild steel coupons in section 6-1. The expected mass loss of mild steel in these experiments is small and hence the sensor can be used for detection of mild steel corrosion before significant amount of weight loss occurs.

#### **6.4 Summary**

The corrosion of mild steel coupons in two types of commercially available soils was studied. The results show that the corrosion in Miraclegro soil which contains more organic compounds comparing to Earthgro (EG), which contains more sands, is faster and corrosion times are more reproducible. In addition, in both cases, corrosion rate increases with sodium chloride content of the soil.

Also, zinc wires were connected to mild steel coupons to study the galvanic corrosion of zinc wires in the soil. The results from these experiments shows that the galvanic corrosion of zinc is about two hundred times faster than mild steel coupons corrosion in soil. This difference in corrosion rates can be used to develop a corrosion sensor. A passive wireless corrosion sensor was developed for corrosion detection of underground structures based on galvanic corrosion of zinc wire. The sensor was used in a series of experiments where it was connected to mild steel

coupons, small pipes, and small painted pipes with small exposed area and successfully worked in all cases.

## CHAPTER VII

### CONCLUSION

#### **7.1 Computational**

Molybdenum oxide and its bronzes with other metals and hydrogen are highly important in many industrial processes as catalysts. They also usually have intense colors which upon reaction change. One example is color change of molybdenum hydrogen bronze upon reaction with hydrogen peroxide from dark blue to yellow. These important properties depend on structure of the compound and oxidation number of molybdenum atoms. The adsorption and reaction of chemicals on the surface of the solid plays the most important role in the catalytic activity of these compounds. In this dissertation, to understand how the size of the cluster and formal charge of the molybdenum atoms affect the properties of the cluster, Time-Dependent Density Functional Theory (TD-DFT) calculations used to simulate the UV-Vis spectra of molybdenum oxide clusters of various sizes composed of Mo(VI) and Mo(V) atoms. Then the adsorption and dissociation of dimethyl peroxide (DMP) on the molybdenum oxide and its bronze with hydrogen studied computationally by means of Density Functional Theory (DFT) calculations to understand the mechanism of this process. And finally, Molybdenum complexes with gluconic

acid were studied experimentally and computationally to explain the equilibrium between dimer and monomer complexes.

### 7.1.1 UV-Vis Spectra Simulation of Molybdenum Oxide Clusters

Molybdenum oxide has three main crystal structures:  $\text{MoO}_3 \cdot 2\text{H}_2\text{O}$ ,  $\beta\text{-MoO}_3 \cdot \text{H}_2\text{O}$ , and  $\alpha\text{-MoO}_3$ . To study the structure-properties relationship, adopting the geometrical parameters of yellow molybdenum oxide  $\beta\text{-MoO}_3 \cdot \text{H}_2\text{O}$ , chains and ribbons of connected tetrahedras containing 2, 3, and 4 molybdenum atoms constructed. Keeping the geometries fixed, UV-Vis spectra of clusters were simulated utilizing Time-Dependent Density Functional Theory (TDDFT) calculations. The results show that while the excitations are spread out in a wide range of wavelengths, by increasing the cluster size, more excitations are possible and spectra are more complicated. Valence (VB) and Conduction (CB) bands of  $\text{MoO}_3$  are composed of O-2p and Mo-4d orbitals respectively, and ligand to metal charge transfer (LMCT) during excitations are expected. Electron densities were calculated for orbitals involving in each excitation and visualized. The results confirm that as expected all absorptions in UV-Vis spectra are associated with ligand to metal charge transfers. Also, as cluster size increases more energy states are available in valence and conduction bands and hence with smaller band gap, absorptions shift to higher wavelengths. When geometry of clusters optimized prior to time-dependent density functional theory calculations, clusters are distorted from layered structure of the bulk material and simulation results show that all the excitations are shifted to lower wavelengths due to stability of the clusters. The absorptions occur bellow approximately 500 nm which describes the yellow color of the molybdenum oxide.

Upon reducing one or more Mo(VI) atoms in the structure to Mo(V) by means of hydrogen insertion, a new band (defect band, DB), is generated which is mainly composed of Mo(V)-4d orbitals and energetically lays between valence and conduction bands (Figure 2-4).

The generation of defect band facilitates the electron transfer between molybdenum atoms of different formal charges. The absorptions corresponding to these intervalence charge transfers (IVCT) appear at higher wavelengths comparing to peaks associated with ligand to metal charge transfer. The new absorptions appear approximately between 500 nm and 800 nm which gives a blue color to the cluster.

The ratio of the absorption intensities associated with intervalence charge transfer for the structures of the same size with different number of Mo(V) atoms, directly reflects the ratio of the number of Mo(V) atoms to Mo(VI) atoms in the cluster structures.

### **7.1.2 Adsorption and Dissociation of Dimethyl Peroxide on Molybdenum Oxide and Its Hydrogen Bronze (100) Surface**

In addition to studying how the cluster properties change with size of the structure and formal charges of molybdenum atoms, to better understanding the catalytic activity of molybdenum oxide and its bronzes, the adsorption and decomposition of dimethyl peroxide on the surface on molybdenum oxide and its hydrogen bronze were studied. (100) surface of the molybdenum oxide is the most active surface of the cluster. Adopting the geometrical parameter of  $\alpha$ -MoO<sub>3</sub>, the (100) surface is simulated with clusters of six molybdenum atoms. While keeping the oxide cluster structure fixed, dimethyl peroxide allowed to relax on the surface utilizing density functional theory calculations. Three molecularly adsorbed forms were located which are results of different orientations of dimethyl peroxide on the cluster surface. These forms can convert to each other through simple rotations about Mo-O bond. Utilizing the same calculation method, transition states for these conversions were located and confirmed by standard Intrinsic Reaction Coordinate (IRC) calculations.

Dissociation of dimethyl peroxide can occur either by O-O or C-O bond cleavage. Frontier orbitals analysis suggests that dissociation of dimethyl peroxide is not possible on the surface of the molybdenum oxide. While attempts to locate structures resulting from O-O bond cleavage did not result in any stable structure, one stable structure is produced from C-O bond cleavage. However, the adsorption energy for this structure is positive and hence energetically is not possible.

Depending on the hydrogen content in the compound, there are four phases of hydrogen molybdenum bronze with general formula of  $H_xMoO_3$  ( $0 \leq x \leq 2$ ). The inserted hydrogen first occupy intralayer positions and then start to occupy interlayer positions. To model the hydrogen molybdenum bronze (100) surface, the geometrical parameters of phase I hydrogen molybdenum bronze are adopted which are very similar to those of  $\alpha$ - $MoO_3$ . The modeled bronze is a cluster of six molybdenum atoms with stoichiometric formula of  $H_{0.33}MoO_3$  (Figure 1-3). Utilizing the same methodology, dimethyl peroxide was allowed to relax on the bronze (100) surface. Similar to oxide, three molecularly adsorbed forms were located which can be converted to each other by simple rotations about Mo-O bond. The transition structures for these conversions also located and confirmed using intrinsic reaction coordinate calculations with small energy barriers as expected for rotations.

Unlike the oxide cluster, hydrogen molybdenum oxide bronze has a significant electron density on (100) surface from HOMO which provides the possibility of dissociation of dimethyl peroxide on the cluster surface. For the O-O bond cleavage,  $OCH_3$  groups can attach to surface molybdenum or oxygen atoms. For this bond dissociation two main products were identified: BOO1 and BOO2. As expected from the electron density of surface atoms, BOO1 where both  $OCH_3$  groups are attached to molybdenum atoms is more stable than BOO2. The other stable form is BOO2 where one methoxy group is attached to surface molybdenum atom and the other one is attached to surface oxygen atom. The conversion of BOO2 to BOO1 is possible in two

steps (rotation followed by migration of methoxy group) through a stable intermediate BOO3. Transition state structures for these steps were also located and confirmed using intrinsic reaction coordinate calculations. The attempts to find pathways for the conversion of molecularly adsorbed forms to structures resulting in from bond dissociation, shows that only BM1 has the proper orientation for conversion to BOO1 and BOO2 through corresponding transition structures.

For the C-O bond cleavage case, four stable structures were located: BCO1, BCO2, BCO3, and BCO4. The most stable structures are BCO3 and BCO4 where CH<sub>3</sub> and OOCCH<sub>3</sub> groups are attached to surface oxygen and molybdenum atoms respectively. Two other stable structures are BCO1 and BCO2, where both CH<sub>3</sub> and OOCCH<sub>3</sub> groups are attached to molybdenum atoms. Although calculations show that there are pathways for conversions of molecularly adsorbed forms to these stable structures, the adsorption energies for all related transition state structures are positive and hence energetically dimethyl peroxide will be desorbed before C-O bond cleavage can happen.

### **7.1.3 Molybdenum-Gluconic Acid Complexes**

A solution containing molybdenum and gluconic acid has a dark blue color with intense color change upon heating or reaction with hydrogen peroxide. Depending on molybdenum to gluconic acid ratio, molybdenum makes monomer and dimer complexes with gluconic acid. Considering the blue color of the solution, and the results from the UV-Vis spectra simulations in the first part of this dissertation, it is concluded that the dimer complex is actually is a mixed-valence compound. The dimer complex is decomposed to monomer complexes upon heating or reaction with hydrogen peroxide. The equilibrium between dimer and monomer molybdenum-gluconate complexes was studied experimentally by means of UV-Vis spectroscopy. The kinetics

of this equilibrium studied at various temperatures and using the initial rates, the activation energy ( $E_a$ ) for this equilibrium calculated as  $53 \pm 14 \text{ kJmol}^{-1}$ . Also assuming that the proposed equilibrium is valid and initially there is not any monomer complexes, the Gibbs free energy ( $\Delta G$ ) for this equilibrium calculated as  $42 \pm 5 \text{ kJmol}^{-1}$ .

To validate the proposed equilibrium and support the experimental results for the Gibbs free energy calculations, the equilibrium were also studied theoretically. The structure of complexes were optimized utilizing density functional theory calculations and UV-Vis spectra were simulated using time-dependent density functional theory framework in gas phase. The results of these calculations suggested that although comparing to experimental spectrum absorptions are at higher wavelengths, there are two possibilities for dimer complex: Mo(VI, VI) and Mo(VI, V). To improve the results by considering the solvent effect in calculations, geometry optimization and spectrum simulation for Mo(VI, V) complex performed in solutions with various dielectric constants, the best result was when water is the solvent. Simulated spectra in aqueous phase properly describe blue color of the Mo(VI, V) dimer and yellow / yellowish color of Mo(VI) and Mo(V) monomers.

The attempt to calculate the Gibbs free energy using frequency calculations was unsuccessful, specially for aqueous solution using polarizable continuum solvation models (PCM). The error in gas phase is reasonable due to assuming that all species are isolated and there is no interaction. While the best result for the aqueous phase calculations is from the simplest solvation model (Onsager model), the results are much worth than gas phase result. To improve the aqueous phase results, either parameters should be optimized for the complexes, or more expensive explicit and hybrid implicit-explicit models should be used.

## 7.2 Experimental

Millions of dollars are lost each year because of corrosion of iron and steel parts of equipments and underground metal structures in various industries. So, the study of corrosion, corrosion inhibition, and corrosion detection have attracted many scientists. Among the various methods of corrosion control, the use of inhibitors is more convenient and economic. Because of the enforced regulations, researches focused on the compounds which are environmentally friendly. Gluconates and gluconic acids are the most attractive compounds to scientists, since they are cheap, effective, and non-toxic. Although, corrosion detection sensors have been developed based on various technologies, still there are many researches to develop a cheap and effective sensor.

### **7.2.1 Corrosion of Metal Wires in Solution**

To study the corrosion and effectiveness of corrosion inhibitors in the laboratory, several standard methods are available. In immersion corrosion test small pieces or coupons of the material are exposed to the test medium and the weight loss of the material is measured for a given period of time. This method needs a lot of cleaning and waiting and hence the experiments are normally long. In this dissertation a new method has been introduced and used to collect the corrosion data which can be easily utilized in high-throughput experiments. This method is based on the change in the resistance of small wires by time.

In Chapter 5 the corrosion of iron and zinc wires in sodium chloride solution were studied using the new data collection method. The results show that the corrosion rate for iron wires in sodium chloride 0.5% and 5% are of the same order. For both iron and zinc wires with small radii up to 0.1 mm corrosion time is short and increases rapidly for thicker wires due to the formation of protective oxide layer. Loosing the electron through oxidation reaction dissolves the metal which in turn metal cations react with hydroxyl ions produced by dissolved oxygen reduction. In presence of dissolved oxygen the produced metal hydroxide gradually is oxidized to

insoluble metal oxide which forms a protective film on surface of the metal and protects it from further corrosion and hence corrosion time increases.

To further examine the applicability of the wire trigger system for corrosion experiments, it was utilized to study the corrosion inhibition efficiency of calcium gluconate and a few commercial inhibitors. The results for calcium gluconate are consistent with available results and the wire trigger system is properly applicable to study the inhibition efficiency of commercial inhibitors.

### **7.2.2 Corrosion in Soil**

Corrosion of buried structures is economically very important, so in Chapter 6 the corrosion of metals was studied in soil. In this study weight loss method was used to determine the corrosion rate of mild steel coupons in soils. Two types of commercially available soils containing various amounts of sodium chloride were used. The results show that while the corrosion rate of coupons increases with sodium chloride content of soils, it is faster in Miraclegro (MG) soil which contain more organic compounds. The fastest corrosion rate is for MG-5 soil which is  $1.30 \times 10^{-2} \pm 6 \times 10^{-4} \text{ mg/day.mm}^2$ .

In addition, galvanic corrosion of zinc wires in soil was studied. Zinc wires of various radii were connected to mild steel coupons and buried in Miraclegro soil containing 5% sodium chloride (MG-5) and corrosion time determined using data collection board. The rate for galvanic corrosion of zinc wires is  $1.04 \pm 0.15 \text{ mg/hr}$  which is about 30 times faster comparing to corrosion of zinc wires in sodium chloride 5% solution.

The galvanic corrosion of zinc wire in Miraclegro soil containing 5% sodium chloride (MG-5) is about 200 time faster than the corrosion of mild steel coupons, this rate difference can

be used to build a sensor for corrosion detection. A passive wireless sensor based on galvanic corrosion of zinc wire was developed and examined for corrosion detection of mild steel coupons and small pipes in Miraclegro soil containing 5% sodium chloride (MG-5). The zinc wire trigger times in sensor when connected to mild steel coupon and small pipe are of the same order when data collection board is used and hence sensor can be used effectively for the corrosion detection.

## REFERENCES

1. Liu, H., P. Cheung, and E. Iglesia, *Zirconia-Supported MoO<sub>x</sub> Catalysts for the Selective Oxidation of Dimethyl Ether to Formaldehyde: Structure, Redox Properties, and Reaction Pathways*. Journal of Physical Chemistry B, 2003. **107**(17): p. 4118-4127.
2. Dieterle, M., et al., *Mixed Molybdenum Oxide Based Partial Oxidation Catalyst: 2. Combined X-ray Diffraction, Electron Microscopy and Raman Investigation of the Phase Stability of (MoVW)<sub>5</sub>O<sub>14</sub>-Type Oxides*. Journal of Molecular Catalysis A: Chemical, 2001. **174**: p. 169-185.
3. Gallei, E. and E. Schwab, *Development of Technical Catalysts*. Catalysis Today, 1999. **51**: p. 535-546.
4. Glaeser, L.C., et al., *Identification of Active Oxide Ions in a Bismuth Molybdate Selective Oxidation Catalyst*. J. Chem. Soc., Faraday Trans., 1985. **81**(1): p. 2903-2912.
5. Haber, J., *The Role of Molybdenum in Catalysis*. Climax Molybdenum Co., Ann Arbor, MI, 1981, 1981.
6. Knozinger, H., *Proceedings of the 9th International Congress on Catalysis*, ed. M.J. Philipps and M. Ternan. Vol. 5. 1988.
7. Ozin, G.A., S. Ozkar, and R.A. Prokopowicz, *Smart Zeolites: New Forms of Tungsten and Molybdenum Oxides*. Accounts of Chemical Research, 1992. **25**: p. 553.
8. Bange, K., *Colouration of Tungsten Oxide Films: A Model for Optically Active Coatings*. Solar Energy Materials & Solar Cells, 1999. **58**: p. 1-131.
9. Deb, S.K., *Physical Properties of a Transition Metal Oxide: Optical and Photoelectric Properties of Single Crystal and Thin Film Molybdenum Trioxide*. Proceedings of the Royal Society A, 1968. **304**: p. 211-231.
10. Deb, S.K. and J.A. Chopoorian, *Optical Properties and Color-Center Formation in Thin Films of Molybdenum Trioxide*. Journal of Applied Physics, 1966. **37**(13): p. 4818-4825.
11. Granqvist, C.G., *Electrochromic Materials: Microstructure, Electronic Bands, and Optical Properties*. Applied Physics A, 1993. **57**: p. 3-12.
12. Porter, V.R., W.B. White, and R. Roy, *Optical Spectra of the Intermediate Oxides of Titanium, Vanadium, Molybdenum, and Tungsten*. Journal of Solid State Chemistry, 1972. **4**: p. 250-254.
13. Whitfield, D.M., S. Stojkovsky, and B. Sarkar, *Metal Coordination to Carbohydrates. Structure and Function*. Coord. Chem. Rev., 1993. **122**: p. 171-225.

14. Yano, S., *Coordination Compounds Containing Sugars and Their Derivatives*. Coord. Chem. Rev., 1988. **92**: p. 113-156.
15. Kuzmin, A. and J. Purans, *Dehydration of the Molybdenum Trioxide Hydrates  $MoO_3 \cdot nH_2O$ : in situ X-Ray Absorption Spectroscopy Study at the Mo K Edge*. Journal of Physics: Condens Matter, 2000. **12**: p. 1959-1970.
16. Zhai, H.-J., et al., *Electronic Structure and Chemical Bonding in  $MO_n^-$  and  $MO_n$  Clusters ( $M=Mo, W$ ;  $n=3-5$ ): A photoelectron Spectroscopy and ab Initio Study*. Journal of American Chemical Society, 2004. **126**: p. 16134-16141.
17. Papakondylis, A. and P. Sautet, *Ab initio Study of the structure of the  $MoO_3$  Solid and Study of the Absorption of  $H_2O$  and  $CO$  Molecules on its (100) Surface*. Journal of Physical Chemistry, 1996. **100**: p. 10681-10688.
18. Tsipis, A.C., *Ab initio and Density Functional Electronic Structure Study of Molybdenum Oxide Clusters*. Phys. Chem. Chem. Phys., 2000. **2**: p. 1357-1363.
19. Kadassov, E., A.W. Apblett, and N.F. Materer, *Density-Functional Studies of Hydrogen Peroxide Absorption and Dissociation on  $MoO_3$  (100) and  $H_{0.33}MoO_3$  (100) Surfaces*, 2013.
20. Volta, J.C. and J.M. Tatibouet, *Structure Sensitivity of  $MoO_3$  in Mild Oxidation of Propylene*. Journal of Catalysis, 1985. **93**(2): p. 467-470.
21. Bruckman, K., et al., *The Role of Different  $MoO_3$  Crystal Faces in Elementary Steps of Propene Oxidation*. Journal of Catalysis, 1987. **104**(1): p. 71-79.
22. Guerrero-Ruiz, A., et al., *Influence of Surface Structure on the Interaction of Allyl Iodide with  $MoO_3$  Catalysts*. Journal of the Chemical Society. Chemical Communications, 1987(13): p. 1031-1033.
23. Smith, M.R. and U.S. Ozkan, *The Partial Oxidation of Methane to Formaldehyde: Role of Different Crystal Planes of  $MoO_3$* . Journal of Catalysis, 1993. **141**(1): p. 124-139.
24. Greenblatt, M., *Molybdenum Oxide Bronzes with Quasi-Dimensional Properties*. Chem. Rev., 1988(88): p. 31-53.
25. Birtill, J.J. and P.G. Dickens, *Phase Relationship in the System  $H_X MoO_3$  ( $0 \leq X \leq 2$ )*. Materials Research Bulletin, 1978. **13**(4): p. 311-316.
26. Adams, S., K.-H. Ehses, and J. Spilker, *Proton Ordering in the Oerls-Distorted Hydrogen Molybdenum Bronze  $H_{0.33}MoO_3$ : Structure and Physical Properties*. Acta Crystallographica Section B, 1993. **B49**: p. 958-967.
27. Ohno, T., et al., *Heptane Isomerization Over Molybdenum Oxides Obtained by  $H_2$  Reduction of  $H_X MoO_3$  with Different Hydrogen Contents*. Applied Catalysis A: General, 2010. **389**: p. 52-59.
28. Mperberg, D.R., et al., *Mechanism of Hydrodeoxygenation of Acrolein on a Cluster Model of  $MoO_3$* . Journal of Physical Chemistry C, 2010. **114**: p. 13782-13795.
29. Xiang, X., et al., *Dispersed Platinum Supported by Hydrogen Molybdenum Bronze-Modified Carbon as Electrocatalyst for Methanol Oxidation*. Journal of Solid State Electrochemistry, 2010. **14**: p. 903-908.
30. Lesnyak, V.V., et al., *The Influence of Hydrogen-Containing Molybdenum and Tungsten Bronzes on the Catalytic Activity of Palladium Composite Catalysts for the Oxidation of  $H_2$ ,  $CO$ , and  $CH_4$* . Russian Journal of Physical Chemistry A, 2008. **82**(9): p. 1456-1459.
31. Sakagami, H., et al.,  *$H_2$  Reduction of Hydrogen Molybdenum Bronze to Porous Molybdenum Oxide and its Catalytic Properties for the Conversions of Pentane and Propan-2-ol*. Advances in Catalysis A: General, 2005. **284**: p. 123-130.
32. Apblett, A.W., et al., *Nanotechnology for Neutralization of Terrorist Explosives*. Ceramic Transactions, 2006. **172**: p. 29-35.
33. Gyuresik, B. and L. Nagy, *Carbohydrates as Ligands: coordination equilibria and structure of the metal complexes*. Coord. Chem. Rev., 2000. **203**: p. 81-149.

34. Carper, W.R. and D.B. Coffin, *NMR Studies of Paramagnetic Metal Ion Interactions with Gluconate and 1,5-Gluconolactone*. Inorg. Chim. Acta, 1990. **167**: p. 261-264.
35. Carper, W.R., D.B. Coffin, and J.R. Addis, *Studies of Magnesium and Manganese Interactions with Gluconate and 1,5-Gluconate*. Spectrochim. Acta, 1989. **45A**(3): p. 391-392.
36. Sawyer, D.T., *Metal-Gluconate Complexes*. Chem. Rev., 1964. **64**: p. 633-643.
37. Tsubomura, T., S. Yano, and S. Yoshikawa, *Cobalt(III) Complexes Containing an Aldonic Acid*. Bull. Chem. Soc. Jpn., 1988. **61**(10): p. 3497-3501.
38. Escandar, G.M., et al., *Interaction of Zinc(II) Ion with D-Aldonic Acids in the Crystalline Solid and Aqueous Solution*. Polyhedron, 1994. **13**(6/7): p. 909-914.
39. Escandar, G.M. and F. Salsa Luis, *Complexes of Cu(II) with D-Aldonic and D-Aldronic Acids in Aqueous Solution*. Can. J. Chem., 1992. **70**: p. 2053-2057.
40. Escandar, G.M., et al., *Complexation of Aluminium(III), Gallium(III) and Indium(III) Ions with D-Gluconic and Lactobionic Acids. A Potentiometric and Nuclear Magnetic Resonance Spectroscopic Study*. J. Chem. Soc. Dalton Trans., 1995: p. 799-804.
41. Brown, D.H. and D. Neumann, *Tungsten(VI) and (V) Complexes with Some Naturally Occuring Ligands*. J. Inorg. Nucl. Chem., 1975. **37**: p. 330-332.
42. Spence, J.T. and G. Kallos, *Molybdenum(V) and Molybdenum(VI) Complexes with Gluconic Acid*. Inorg. Chem., 1963. **2**(4): p. 710-713.
43. Antonio, C.A., L. Jover Elisa, and A. Ramirez Jose, *Tungsten(VI) Complexes Formed in an Excess of Gluconic Acid: A Polarimetric and Spectrophotometric Study*. Transition Met. Chem., 1985. **10**(11): p. 405-409.
44. Llopis, E., A. Ramirez Jose, and A. Cervilla, *Tungsten(VI)-Gluconic Acid Complexes: Polarimetric and <sup>13</sup>C NMR Studies in an Excess of Tungsten(VI)*. Transition Met. Chem., 1986. **11**(12): p. 489-494.
45. Ramos, M.L., M.M. Calderia, and V.M.S. Gil, *NMR Spectroscopy Study of the Complexation of D-Gluconic Acid with Tungsten(VI) and Molybdenum(VI)*. Carbohydrate Research, 1997. **304**: p. 97-109.
46. Szabo, A. and N.S. Ostlund, *Modern Quantum Chemistry: Introduction to Advanced Electronic Structure Theory* 1989, Mineola, New York: Dover Publications, INC.
47. Hohenberg, P. and W. Kohn, *Inhomogeneous Electron Gas*. Physical Review, 1964. **136**(3B): p. B864-B871.
48. Kohn, W. and L.J. Sham, *Self-Consistent Equations Including Exchange and Correlation Effects*. Physical Review, 1965. **140**(4A): p. A1133-A1138.
49. Koch, W. and M.C. Holthausen, *A Chemist's Guide to Density Functional Theory*. Second ed 2001, Germany: John Wiley & Sons.
50. Pople, J.A., P.M.W. Gill, and B.G. Johnson, *Kohn-Sham Density Functional Theory within a Finite Basis Set*. Chemical Physics Letters, 1992. **199**: p. 557-560.
51. Lieb, E.H. and S. Oxford, *Improved Lower Bound on the Indirect Coulomb Energy*. International Journal of Quantum Chemistry, 1981. **19**(3): p. 427-439.
52. Becke, A.D., *Density-Functional Exchange-Energy Approximation with Correct Asymptotic Behavior*. Physical Review A, 1988. **38**(6): p. 3098-3100.
53. Perdew, J.P. and W. Yue, *Accurate and Simple Density Functional for the Electronic Exchange Energy: Generalized Gradient Approximation*. Physical Review B, 1986. **33**(12): p. 8800-8802.
54. Perdew, J.P., et al., *Atoms, Molecules, Solids, and Surfaces: Applications of the Generalized Gradient Approximation for Exchange and Correlation*. Physical Review B, 1992. **46**(11): p. 6671-6687.
55. Perdew, J.P., K. Burke, and M. Ernzerhof, *Generalized Gradient Approximation Made Simple*. Physical Review Letters, 1996. **77**(18): p. 3865-3868.

56. Becke, A.D. and M.R. Roushel, *Exchange Holes in Inhomogeneous Systems: A Coordinate-Space Model*. Physical Review A, 1989. **39**(8): p. 3761-3767.
57. Becke, A.D., *Density-Functional Thermochemistry. IV. A New Dynamical Correlation Functional and Implications for Exact-Exchange Mixing*. Journal of Chemical Physics, 1996. **104**(3): p. 1040-1046.
58. Boese, A.D. and N.C. Handy, *New Exchange-Correlation Density Functionals: The Role of the Kinetic-energy Density*. Journal of Chemical Physics, 2002. **116**(22): p. 9559-9569.
59. Lee, C., W. Yang, and R.G. Parr, *Development of the Colle-Salvetti Correlation-Energy Formula into a Functional of the Electron Density*. Physical Review B, 1988. **37**(2): p. 785-789.
60. Furche, F. and K. Burke, *Time-Dependent Density Functional Theory in Quantum Chemistry*. Annual Reports in Computational Chemistry, 2005. **1**: p. 19-30.
61. Ullrich, C.A., *Time-Dependent Density-Functional Theory* 2012, New York: Oxford University Press Inc.
62. Roux, B. and T. Simonson, *Implicit Solvent Models*. Biophysical Chemistry, 1999. **78**(1-2): p. 1-20.
63. Tomasi, J. and M. Persico, *Molecular Interactions in Solution: An Overview of Models Based on Continuous Distributions of the Solvent*. Chemical Reviews, 1994. **94**(7): p. 2027-2094.
64. Onsager, L., *Electric Moments of Molecules in Liquids*. Journal of American Chemical Society, 1936. **58**(8): p. 1486-1493.
65. Cossi, M., et al., *Ab Initio Study of Solvated Molecules: A New Implementation of the Polarizable Continuum Model*. Chemical Physics Letters, 1996. **255**(4-6): p. 327-335.
66. Truong, T.N. and E.V. Stefanovich, *A New Method for Incorporating Solvent Effect Into the Classical, ab initio Molecular Orbital and Density Functional Theory*. Chemical Physics Letters, 1995. **240**(4): p. 253-260.
67. Klamt, A., *Cr-Like Screening Model for Real Solvents: A New Approach to the Quantitative Calculation of Solvation Phenomena*. Journal of Physical Chemistry, 1995. **99**(7): p. 2224-2235.
68. Barone, V. and M. Cossi, *Quantum Calculation of Molecular Energies and Energy Gradients in Solution by a Conductor Solvent Model*. J. Phys. Chem. A, 1998. **102**: p. 1995-2001.
69. Marenich, A., C. Cramer, and D. Truhlar, *Universal Solvation Model Based on Solute Electron Density and on a Continuum Model of the Solvent Defined by the Bulk Dielectric Constant and Atomic Surface Tensions*. J. Phys. Chem. B, 2009. **113**: p. 6378-6396.
70. ASTM-G193, *Standard Terminology and Acronyms Relating to Corrosion*, 2012, American Society for Testing and Materials.
71. Kruger, J., *Cost of Metallic Corrosion*, in *Uhlig's Corrosion Handbook*, R.W. Revie, Editor 2000, John Wiley & Sons, Inc.: New York. p. 3-10.
72. Baboian, R., *Corrosion Tests and Standards: Application and Interpretation* 1995.
73. Kopeliovich, D. *Corrosion and Oxidation*. 2012; Available from: <http://www.substech.com/>.
74. Fontana, M.G. and N.D. Greene, *Corrosion Engineering* 1978, New York: McGraw-Hill.
75. Smialowska, Z.S., *Pitting Corrosion of Metals* 1986, USA: NACE.
76. Schmutz, P. *Surfaces, Interfaces, and their Applications II*. 2013; Available from: [http://www.surface.mat.ethz.ch/education/courses/surfaces\\_interfaces\\_and\\_their\\_applications\\_II](http://www.surface.mat.ethz.ch/education/courses/surfaces_interfaces_and_their_applications_II).
77. Agarwala, V.S., P.L. Reed, and S. Ahmad, *Corrosion Detection and Monitoring - A Review*, in *Corrosion 2000* 2000, NACE International: Orlando, FL.

78. ASTM-STP866, *Laboratory Corrosion Tests and Standards*, 1983, American Society for Testing and Materials.
79. Schafer, G.J., J.R. Gabriel, and P.K. Foster, *On the Role of the Oxygen Concentration Cell in Crevice Corrosion and Pitting*. Journal of the Electrochemical Society, 1960. **107**(12): p. 1002-1004.
80. Natishan, P., *Introduction to Methods of Corrosion Protection*, in *Corrosion: Fundamentals, Testing, and Protection* 2003, ASM International: USA.
81. Khaladkar, P., *Fight Corrosion with Plastic*, in *Chemical Engineering Magazine* 1995.
82. *Corrosion Detection Technologies - A Sector Study*, 1998, North American Technology Industrial Base Organization (NATIBO), Prepared by BDM Federal Inc: McLean, VA.
83. Chawla, S.L. and R.K. Gupta, *Materials Selection for Corrosion Control*, in *Corrosion: Fundamentals, Testing, and Protection* 2003, ASM International: USA. p. 909-928.
84. Aiello, L., M. Colavita, and V. Agarwala, *Galvanic Sensor for Monitoring Structural Damage*. Corrosion Reviews, 2011. **25**(1-2): p. 39-50.
85. Song, H.-W. and V. Saraswathy, *Corrosion Monitoring of Reinforced Concrete Structures - A Review*. International Journal of Electrochemical Science, 2007. **2**(1): p. 1-28.
86. Martinez, I. and C. Andrade, *Examples of Reinforcement Corrosion Monitoring by Embedded Sensors in Concrete Structures*. Cement and Concrete Composites, 2009. **31**(8): p. 545-554.
87. Ardringa, M.M., et al. *Low-Cost Wireless Corrosion and Conductivity Sensors*. in *Proc. SPIE 6174, Smart Structures and Materials: Sensors and Smart Structures Technologies for Civil, Mechanical, and Aerospace Systems*. 2006. SPIE - The International Society for Optical Engineering.
88. Dickerson, N.P., et al. *Wireless Low-Cost Corrosion Sensors for Reinforced Concrete Structures*. in *Proc. SPIE 5765, Smart Structures and Materials: Sensors and Smart Structures Technologies for Civil, Mechanical, and Aerospace Systems*. 2005. SPIE - The International Society for Optical Engineering.
89. Frisch, M.J. and et al, *Gaussian 09*, 2010, Gaussian Inc.: Wallingford CT.
90. Dennington, R., T. Keith, and J. Millam, *GaussView 5*, 2009.
91. O'Boyle, N.M., A.L. Tenderholt, and K.M. Langer, *cclib: A Library for Package-Independent Computational Chemistry Algorithms*. Journal of Computational Chemistry, 2008. **29**(5): p. 839-845.
92. Becke, A.D., *Density-Functional Thermochemistry. III. The Role of Exact Exchange*. J. Chem. Phys., 1993. **98**: p. 5648-5652.
93. Lee, C., W. Yang, and R.G. Parr, *Development of the Colle-Salvetti Correlation-Energy Formula Into a Functional of the Electron Density*. Phys. Rev. B, 1988. **37**: p. 785-789.
94. Kendall, R.A., T.H.D. Jr., and R.J. Harrison, *Electron Affinities of the First-Row Atoms Revisited. Systematic Basis Sets and Wave Functions*. Journal of Chemical Physics, 1992. **96**: p. 6796-6806.
95. Andrae, D., et al., *Energy-Adjusted ab Initio Pseudopotentials for the Second and Third Row Transition Elements*. Theoretica Chimica Acta, 1990. **77**(2): p. 123-141.
96. Dieterle, M., G. Weinberg, and G. Mestl, *Raman Spectroscopy of Molybdenum Oxides. Part I. Structural Characterization of Oxygen Defects in MoO<sub>3-x</sub> by DR UV/VIS, Raman Spectroscopy and X-ray Diffraction*. Physical Chemistry Chemical Physics, 2002. **4**: p. 812-821.
97. Kihlberg, L., *Least Squares Refinement of the Crystal Structure of Molybdenum Trioxide*. Arkiv for Kemi, 1963. **21**(34): p. 357-364.
98. Clark, T., et al., *Efficient Diffuse Function-Augmented Basis-Sets for Anion Calculations. 3. The 3-21+G Basis Set for 1st-Row Elements, Li-F*. J. Comp. Chem., 1983. **4**: p. 294-301.

99. Mclean, A.D. and G.S. Chandler, *Contracted Gaussian-Basis Sets for Molecular Calculations. I. 2nd Row Atoms, Z=11-18*. J. Chem. Phys., 1980. **72**: p. 5639-5678.
100. Hay, P.J. and W.R. Wadt, *Ab initio Effective Core Potentials for MOlecular Calculations: Potentials for K to Au Including the Outermost Core Orbitals*. J. Chem. Phys., 1985. **82**: p. 299-310.
101. T.H. Dunning, J. and P.J. Hay, *Modern Theoretical Chemistry*, ed. F.S.I. H. Vol. 3. 1976, New York: Plenum.
102. Boys, S.F. and F. Bernardi, *Calculation of Small Molecular Interactions by Differences of Separate Total Energies - Some Procedures with Reduced Errors*. Molecular Physics, 1970. **19**: p. 533-556.
103. Haas, B. and H. Oberhammer, *Gas-Phase Structure of Dimethyl Peroxide*. Journal of American Chemical Society, 1984. **106**(21): p. 6146-6149.
104. Gase, W. and J.E. Boggs, *The Structures of Dimethyl Peroxide, CH<sub>3</sub>OOCH<sub>3</sub>, and Bis-(Trifluoromethyl) Peroxide (CF<sub>3</sub>OOCF<sub>3</sub>)*. Journal of Molecular Structure, 1984. **116**: p. 207-210.
105. Onsager, L., *Electric Moments of Molecules in Liquids*. J. Am. Chem. Soc., 1936. **58**: p. 1486-1493.
106. Tomasi, J., B. Mennucci, and R. Cammi, *Quantum Mechanical Continuum Solvation Models*. Chem. Rev., 2005. **105**: p. 2999-3093.
107. Bussan, D., *Applications of Molybdenum Utilized in Sensing Devices*, 2011, Oklahoma State University.
108. Lehtonen, A. and R. Sillanpaa, *Dioxomolybdenum(VI) Complexes of Chelating Alkoxides*. Acta Chemica Scandinavica, 1999. **53**: p. 1078-1082.
109. Liu, S. and J. Zubieta, *Polyoxymolybdate-Alkoxide Interactions. The Crystal and Molecular Structures of the Erythritolate Complexes [(n-C<sub>4</sub>H<sub>9</sub>)<sub>4</sub>N]<sub>2</sub>[Mo<sub>2</sub>O<sub>5</sub>(eryth)] and [(n-C<sub>4</sub>H<sub>9</sub>)<sub>4</sub>N][Mo<sub>2</sub>O<sub>5</sub>(Heryth)]* Polyhedron, 1989. **8**(12): p. 1571-1573.
110. ASTM-G193, *Standard Terminology and Acronyms Relating to Corrosion*, 2012, American Society for Testing and Materials.
111. ASTM-G1, *Standard Practice for Preparing, Cleaning, and Evaluating Corrosion Test Specimens*, 2011, American Society for Testing and Materials.
112. ASTM-G31, *Standards Guide for Laboratory Immersion Corrosion Testing of Metals*, 2012, American Society for Testing and Materials.
113. Strehblow, H.-H., *Nucleation and Repassivation of Corrosion Pits for Pitting on Iron and Nickel*. Materials and Corrosion, 1976. **27**(11): p. 769-840.
114. Gunasekaran, G., et al., *Enhanced Synergistic Inhibition by Gluconate in Low Chloride Media. Part I. Kinetics of Corrosion*. Proc. Indian Acad. Sci. (Chem. Sci.), 1996. **108**(4): p. 399-405.
115. Abd-El-Naby, B.A., et al., *Effect of Some Natural Extracts on the Corrosion of Zinc in 0.5 M NaCl*. International Journal of Electrochemical Science, 2012. **7**: p. 5864-5879.
116. Peulon, S. and D. Lincot, *Mechanistic Study of Cathodic Electrodeposition of Zinc Oxide and Zinc Hydroxychloride Films from Oxygenated Aqueous Zinc Chloride Solutions*. Journal of Electrochemical Society, 1998. **145**(3): p. 864-874.
117. M.Rostom, A., C. Mustafa, and M. Habib, *Effect of Molybdate, Nitrite and Zinc Ions on the Corrosion Inhibition of Mild Steel in Aqueous Chloride Media Containing Cupric Ions*. Journal of Scientific Research, 2009. **1**(1): p. 82-91.
118. Siragul, K., et al., *Corrosion Inhibition of Mild Steel by Calcium Gluconate in Simulated Cooling Water*. Leonardo Electronic Journal of Practices and Technology, 2010(16): p. 167-176.
119. Shibli, S.M.A. and V.A. Kumary, *Inhibitive Effect of Calcium Gluconate and Sodium Molybdate on Carbon Steel*. Anti-Corrosion Methods and Materials, 2004. **51**(4): p. 277-281.

120. Rajendran, S., B.V. Apparao, and N. Palaniswamy, *Calcium Gluconate as Corrosion Inhibitor for Mild Steel in Low Chloride Media*. British Corrosion Journal, 1998. **33**(4): p. 315-317.
121. O.Lahondny-Sarc, F. Kapor, and R. Halle, *Corrosion Inhibition of Carbon Steel in Chloride Solutions by Blends of Calcium Gluconate and Sodium Benzoate*. Materials and Corrosion, 2000. **51**: p. 147-151.
122. L.Leroy, R., *Chelate Inhibitors for Zinc and Galvanized Products*. Corrosion-NACE, 1978. **34**(3): p. 98-109.
123. Chang, H.-C. and E. Matijevic, *Interactions of Metal Hydrous Oxides with Chelating Agents: IV. Disolution of Hematite*. Journal of Colloid and Interface Science, 1983. **92**(2): p. 479-488.
124. Wilmott, M.J. and T.R. Jack, *Corrosion by Soils*, in *Uhlig's Corrosion Handbook*, R.W. Revie, Editor 2000, John Wiley & Sons, INC: New York. p. 329-348.
125. Uhlig, H.H. and R.W. Revie, *Corrosion and Corrosion Control: An Introduction to Corrosion Science and Engineering* 1985, New York: John Wiley & Sons INC.
126. ASTM-G162, *Standard Practice for Conducting and Evaluating Laboratory Corrosion Tests in Soils*, 2010, American Society for Testing and Materials.

## VITA

Ahmad Razzaghi Soufiani

Candidate for the Degree of

Doctor of Philosophy

Thesis: COMPUTATIONAL STUDIES OF MOLYBDENUM OXIDE CLUSTERS  
AND ENVIRONMENTAL CORROSION OF IRON AND ZINC

Major Field: Chemistry

Biographical:

### **Education:**

Completed the requirements for the Doctor of Philosophy in Physical Chemistry at Oklahoma State University, Stillwater, Oklahoma in July, 2014.

Completed the requirements for the Master of Science in Physical chemistry at Isfahan University of technology, Isfahan, Iran in 1999.

Completed the requirements for the Bachelor of Science in Chemistry at Birjand University, Birjand, Iran in 1996.

### **Experience:**

Graduate Research and Teaching Assistant, Oklahoma State University,  
Jan 2009 - July 2014

GC & Service Laboratories Manager, Borzouyeh Petrochemical Company  
(BPC), Iran, Aug 2004 - Oct 2008

Senior Laboratory Chemist, Borzouyeh Petrochemical Company (BPC), Iran,  
Dec 2002 - Jul 2004

Research Chemist, Kimya Maadan Co., Iran, Jan 2002 - Nov 2002

Graduate Research and Teaching Assistant, Isfahan University of Technology,  
Aug 1996 - Feb 1999

### **Professional Memberships:**

American Chemical Society